DTU Physics
Department of Physics

Bachelor Thesis

Theory of microscale acoustofluidics in inhomogeneous suspensions

Jakob Milo Hauge
s134239

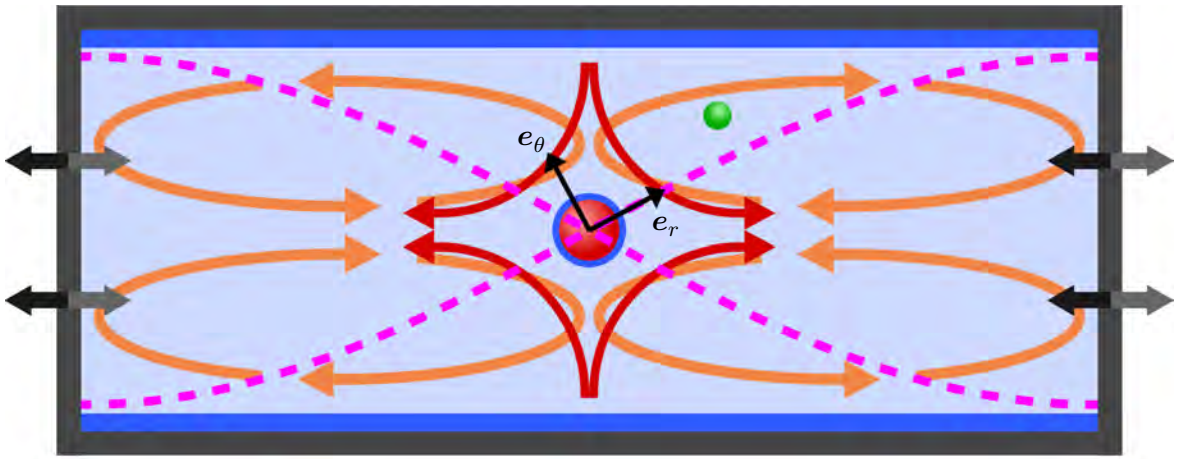

Supervisor: Henrik Bruus

DTU Physics - Department of Physics
Technical University of Denmark

25 July 2016

Abstract

Acoustofluidics is a topic that has received increased interest in last few decades due to its potential biomedical applications such as particle detection, separation and focusing.

In this thesis we study how an inhomogeneity in the form of a 12-µm-radius so-called seed particle affects the movement of sub-micron particles, such as sub-cellular organelles and viruses, suspended in a fluid supporting a standing pressure wave. The work is motivated by experimental findings that the presence of one ore more 12-µm-radius seed particles in the microfluidic channels enables an otherwise difficult focusing of sub-micron particles.

First- and second-order perturbation theory is employed to present the governing equations for small acoustic amplitudes, and to introduce the acoustic radiation force and acoustic streaming.

We derive an analytical expression for the contribution to the radiation force from the acoustic fields scattered on the seed particle. Comparing this expression to both the standard expression for standing wave fields and the drag force that dominates the motion of sub-micron particles, we conclude the contribution is negligible for particles of density and compressibility similar to those of biological particles.

We use the method of matched asymptotic expansions to derive an analytical expression for the streaming generated by a rigid, spherical particle in the node of a standing pressure wave. The expression is used to estimate the total streaming pattern due to the seed particle and the channel boundaries in a microfluidic channel of rectangular cross section. Numerical calculations of the total streaming pattern in a cylinder are compared to the analytical estimation for a rectangular channel. Despite the consideration of different geometries, we find in both the analytical and numerical studies that the main effect of the seed particle on the streaming pattern is the generation of small circulating flows close to its surface.

Simulations of the trajectories of sub-micron particles suspended in the cylindrical geometry indicate that trapping of these might be enabled by the presence of a seed particle inhomogeneity.

The findings are a step towards a more thorough understanding of the effects of large seed particles in microfluidic systems.

Preface

This bachelor thesis, corresponding to a workload of 15 ECTS points, is submitted in partial fulfilment of the requirements for obtaining the degree in Bachelor of Science in Physics and Nanotechnology at the Technical University of Denmark (DTU). It has been prepared in the Theoretical Microfluidics Group headed by Professor Henrik Bruus at DTU Physics, and treats microscale acoustofluidics.

First and foremost, I would like to thank my supervisor Henrik Bruus for his exceptional dedication to, and genuine interest in, his students. His enthusiasm, cheerfulness and guidance has made the work with this thesis a great pleasure.

Secondly, I would like to thank PhD students Mikkel Ley and Jonas Karlsen for helping me understand various phenomena within the field of acoustofluidics. I would also like to thank my fellow BSc student Andreas Munk, with whom I have had many fruitful discussions.

Lastly, I wish to thank my family for their support during the hard times of both this project and my bachelor programme in general.

Jakob Milo Hauge
DTU Physics - Department of Physics
Technical University of Denmark
25 July 2016

Contents

List of figures **ix**

List of tables **xi**

List of symbols **xiii**

1 Introduction **1**
1.1 Lab-on-a-chip systems 1
1.2 Thesis outline 3

2 Governing equations **5**
2.1 Definition of the continuum fields 5
2.2 Conservation of mass and momentum 6
2.3 Perturbation theory 7
2.3.1 First-order perturbation theory 7
2.3.2 Second-order perturbation theory 9

3 Weak form modelling in COMSOL **11**
3.1 The finite element method and boundary conditions 11

4 Acoustofluidic theory **13**
4.1 The acoustic wave equation 13
4.2 Acoustic radiation force 14
4.3 Acoustic streaming 18

5 Influence of a seed particle on the radiation force **21**
5.1 Calculation of the force contribution 22
5.2 Discussion of the results 26

6 Acoustic streaming generated by a rigid sphere **31**
6.1 Characteristic numbers 32
6.2 Reformulation of the Navier-Stokes equation 34
6.3 The scalar equation of motion 35
6.4 Boundary conditions 35

6.5 Singular perturbation theory and the method of matched asymptotic expansions . . . 37
6.6 Problem summary . . . 39
6.7 Outer first-order solution . . . 40
6.8 Inner first-order solution . . . 41
6.9 First-order asymptotic matching . . . 41
6.10 Inner second-order solution . . . 42
6.11 Outer second-order solution . . . 43
6.12 Second-order asymptotic matching . . . 43
6.13 Streaming outside the boundary layer . . . 44

7 Influence of a seed particle on the streaming pattern 47
7.1 Simulations of acoustic streaming . . . 51
7.1.1 Setting up COMSOL . . . 51
7.1.2 The simulated acoustic fields . . . 52
7.1.3 Particle tracing . . . 53

8 Conclusion and outlook 57
8.1 Conclusion . . . 57
8.2 Outlook . . . 58
8.2.1 Analytical treatment of the radiation force . . . 58
8.2.2 Analytical treatment of the streaming . . . 58
8.2.3 Numerical simulations of the seed particle streaming . . . 58

A Physical constants 59

B Appendix to Chapter 2 61
B.1 Fluid description . . . 61
B.2 Mathematial notation . . . 62

C Appendix to Chapter 4 65
C.1 Detailed calculation of the scattered velocity potential . . . 65

D Appendix to Chapter 5 67
D.1 Derivation of the scalar equation of motion . . . 67
D.2 Exact first-order solution of streaming equation . . . 71
D.3 Transformation of the streaming equation to inner co-ordinates . . . 74
D.4 Details in the first-order asymptotic matching . . . 76
D.5 Calculation of the product terms in the inner second-order streaming equation 77
D.6 Outer second-order solution . . . 80

E Appendix to Chapter 7 83

Bibliography 85

List of Figures

1.1 Three different ways to manipulate particles by acoustophoresis 2
1.2 Typical acoustophoretic system setup 3

3.1 Sketch of discretised computation domain in COMSOL. 11

4.1 Standing wave acoustic fields in a channel of rectangular cross section . . . 16
4.2 Acoustic radiation force for standing wave fields 17
4.3 Acoustic streaming in channels of rectangular cross section 19

5.1 Acoustic fields scattered from a seed particle 22
5.2 Radiation force contribution from seed particle 26
5.3 Radiation force contribution from seed particle relative to the original force 27
5.4 Total radiation force relative to streaming-induced drag force 29

6.1 Sphere in unbounded fluid supporting a standing pressure wave 32
6.2 Streaming due to a sphere in an oscillating fluid 45

7.1 System for comparison of sphere and channel streaming in an oscillating fluid 48
7.2 Drag force due to sum of sphere and channel streaming 49
7.3 Axially symmetric geometry used in COMSOL simulations 51
7.4 Second-order velocity fields simulated in COMSOL 53
7.5 Particle trajectories simulated in COMSOL 54

E.1 Simulated first-order and time-averaged second-order acoustic fields 83

List of Tables

A.1 Typical material parameter values 59

List of symbols

Symbol	Description	Unit
$\equiv$	Equal to by definition	
$\approx$	Approximately equal to	
$\sim$	Same order of magnitude as	
$\leq$	Less than or equal to	
$\geq$	Greater than or equal to	
$\lesssim$	Order of magnitude less than or equal to	
$\gtrsim$	Order of magnitude greater than or equal to	
$\lessapprox$	Less than approximately	
$\gtrapprox$	Greater than approximately	
$\ll$	Much smaller than	
$\gg$	Much bigger than	
$\cdot$	Scalar product	
$\times$	Cross product or multiplication sign	
$\partial_i = \frac{\partial}{\partial i}$	Partial derivative with respect to $i = x, y, z$	m^{-1}
$\boldsymbol{\nabla}$	Nabla or gradient vector operator	m^{-1}
$\boldsymbol{\nabla}\cdot$	Divergence operator	m^{-1}
$\boldsymbol{\nabla}\times$	Rotation operator	m^{-1}
∇^2	Laplacian operator	m^{-2}
$\Box^2 = \nabla^2 - \frac{1}{c_0^2}\partial_t^2$	d'Alembertian operator	m^{-2}
$\bullet_i$	ith component of $\bullet$ where $i = x, y, z$ unless otherwise stated	
$\bullet_0, \bullet_2, \bullet_3$	0th-, 1st, and 2nd-order perturbations of $\bullet$	
$\bullet_{\mathrm{I}}, \bullet_{\mathrm{II}}, \bullet_{\mathrm{III}}, \bullet_{\mathrm{IV}}$	Constant coefficients to be determined by boundary conditions	
$\bullet_{\mathrm{a}}$	Bulk amplitude of first-order field $\bullet$	
$\bullet^*$	Complex conjugate of $\bullet$	
$\bullet_{\mathrm{in}}$	Incident acoustic field $\bullet$	
$\bullet_{\mathrm{sc}}$	Scattered acoustic field $\bullet$	
$\bullet_{\mathrm{ext}}$	Acoustic field $\bullet$ created by external influence	

Symbol	Description	Unit
$\bullet'$	Non-dimensionalised physical quantity $\bullet$	
$\tilde{\bullet}$	Parameter value $\bullet$ of particle relative to that of the suspending medium	
$\lvert \bullet \rvert$	Numerical value of $\bullet$	
$\langle \bullet \rangle$	Time average of $\bullet$	
$\langle \bullet, \circ \rangle$	Projection of $\circ$ on $\bullet$. Also known as the inner product.	
$\mathrm{Re}(\bullet)$	Real part of $\bullet$	
$\mathrm{Im}(\bullet)$	Imaginary part of $\bullet$	
1D, 2D, 3D	One-, two- and three-dimensional	
a	Microparticle radius	m
a_c	Critical particle radius	m
a_p	Probe particle radius	m
a_s	Seed particle radius	m
c_0	Isentropic speed of sound	$\mathrm{m\ s^{-1}}$
$\mathrm{d}a$	Two-dimensional integral measure	m^2
$\mathrm{d}\boldsymbol{r}$	Three-dimensional integral measure	m^3
e	Euler's number	
$\boldsymbol{e}_x$, $\boldsymbol{e}_y$, $\boldsymbol{e}_z$	Cartesian unit vectors	
$\boldsymbol{e}_r$	Radial unit vector	
$\boldsymbol{e}_\theta$	Polar unit vector	
$\boldsymbol{e}_\phi$	Azimuthal unit vector	
E_ac	Acoustic energy density	$\mathrm{J/m^{-3}}$
f	Frequency	$\mathrm{s^{-1}}$
f_0, f_1	Monopole and dipole scattering coefficients	
$f_{0,\mathrm{p}}$, $f_{1,\mathrm{p}}$	Monopole and dipole scattering coefficients of probe particle	
$f_{0,\mathrm{s}}$, $f_{1,\mathrm{s}}$	Monopole and dipole scattering coefficients of seed particle	
$\boldsymbol{f}^\mathrm{body}$	Body force density	$\mathrm{N\ m^{-3}}$
F	Source term or arbitrary field	
$\boldsymbol{F}^\mathrm{drag}$	Viscous Stokes drag force	N
$\boldsymbol{F}^\mathrm{rad}$	Acoustic radiation force	N
$\boldsymbol{F}^\mathrm{rad}_\mathrm{rf}$	Acoustic radiation force for real incident fields	N
$\boldsymbol{F}^\mathrm{rad}_\mathrm{s}$	Contribution to the acoustic radiation force from the fields scattered by a seed particle	N
$\boldsymbol{F}^\mathrm{rad}_\mathrm{sw}$	Acoustic radiation force for standing wave fields	N
h	Microchannel height	m

Symbol	Description	Unit
i	Unit imaginary number	
$\mathbf{I}$	Identity matrix	
$\boldsymbol{J}$	Flux term	
$k_0 = \frac{2\pi}{\lambda} = \frac{\omega}{c}$	Undamped acoustic wavenumber	m^{-1}
k	Damped acoustic wavenumber	m^{-1}
$\lvert M\rvert^2 = \frac{\mathrm{i}\omega a^2}{\nu} = 2\,\frac{a^2}{\delta^2}$	Squared absolute value of boundary number	
$\boldsymbol{n}$	Surface outward normal vector	
p	Pressure	$\mathrm{N\ m}^{-2}$
$\boldsymbol{r}$	Position vector	m
Re	Reynolds number	
s	Entropy	$\mathrm{J\ K}^{-1}$
t	Time	s
T	Temperature	K
U	Acoustic potential	m^{-4}
$\boldsymbol{v}$	Eulerian velocity field vector	$\mathrm{m\ s}^{-1}$
v	Eulerian velocity field magnitude	$\mathrm{m\ s}^{-1}$
ΔV	Fluid particle volume	m^{-3}
w	Microchannel width	m
(x, y, z)	Cartesian co-ordinates	m
α	Microchannel aspect ratio	
β	Viscosity ratio	
Γ	Viscous damping factor	
δ	Acoustic boundary layer thickness	m
δ_{ij}	Kronecker delta	
$\varepsilon = \frac{v_\mathrm{a}}{\omega a}$	Amplitude number	
η	Dynamic shear viscosity	$\mathrm{kg\ m}^{-1}\ \mathrm{s}^{-1}$
η_B	Bulk viscosity	Pa s
θ	Polar angle	
κ	Compressibility	Pa^{-1}
λ	Acoustic wavelength	m
$\mu = \cos\theta$	Transformed polar co-ordinate	
ν	Kinematic viscosity	$\mathrm{m}^2\ \mathrm{s}^{-1}$
ρ	Eulerian mass density field	$\mathrm{kg\ m}^{-3}$
$\boldsymbol{\sigma}$	Total stress tensor	$\mathrm{N\ m}^{-2}$
τ	Oscillation period	s

Symbol	Description	Unit
ϕ	Velocity potential	$\mathrm{m}^2\ \mathrm{s}^{-1}$
Φ	Acoustic contrast factor	
$\omega = 2\pi f$	Angular frequency	s^{-1}
Ω	2D or 3D domatin	
$\partial\Omega$	Boundary of the domain Ω	
ψ	Streaming function	$\mathrm{m}^3\ \mathrm{s}^{-1}$

Chapter 1

Introduction

Acoustofluidics is the study of acoustics in fluids but often, as in this thesis, the term refers to microscale acoustofluidics, which is the combined field of acoustics and microfluidics. The interest in the field has increased as the ability to fabricate lab-on-a-chip systems has gained ground due to the potential biomedical applications involving particle handling. This could be detection or analysis of cells, bacteria, sub-cellular organelles and viral particles for diagnostic, forensic or food control purposes [1]. Among numerous examples are detection of tumour cells [2], automated enrichment of sperm cells [3] and quality control of raw milk [4].

1.1 Lab-on-a-chip systems

A lab-on-a-chip system integrates various laboratory functions on a single sub-millimetre-sized chip. Such chips can often be mass-produced for fast single-use analysis in the field far from laboratories and, due to the sub-millimetre scale of the chips, the required sample size can be reduced considerably. However, in order to manipulate particles in suspensions at this scale, a thorough understanding of microfluidics is necessary.

There are many different ways to handle particle suspensions. For example, magnetophoresis [5] and dielectrophoresis [6] are particle manipulation techniques where the particles move under the influence of a magnetic and an electric field, respectively. Such techniques can be used only on particles with specific magnetic or electric properties and flow rates of the order 0.01 L/h and 0.001 L/h, respectively [7]. It is therefore desirable to have techniques for particle manipulation that work when these requirements are not met. Acoustophoresis, where the particles move under the influence of a standing acoustic wave, is one such technique. The basis for manipulation is differences in size, density and compressibility between the medium and the particles, and between the different particles. Moreover, it has potential flow rates of the order 1 L/h [7].

Figure 1.1 shows a top view of three cases of acoustophoresis in a microchannel. The particles enter the channel through the inlets, flow through an acoustophoretic zone where the manipulation takes place, and exit through outlets. The three cases illustrate three different ways of manipulating particles by exploiting the acoustic radiation force which

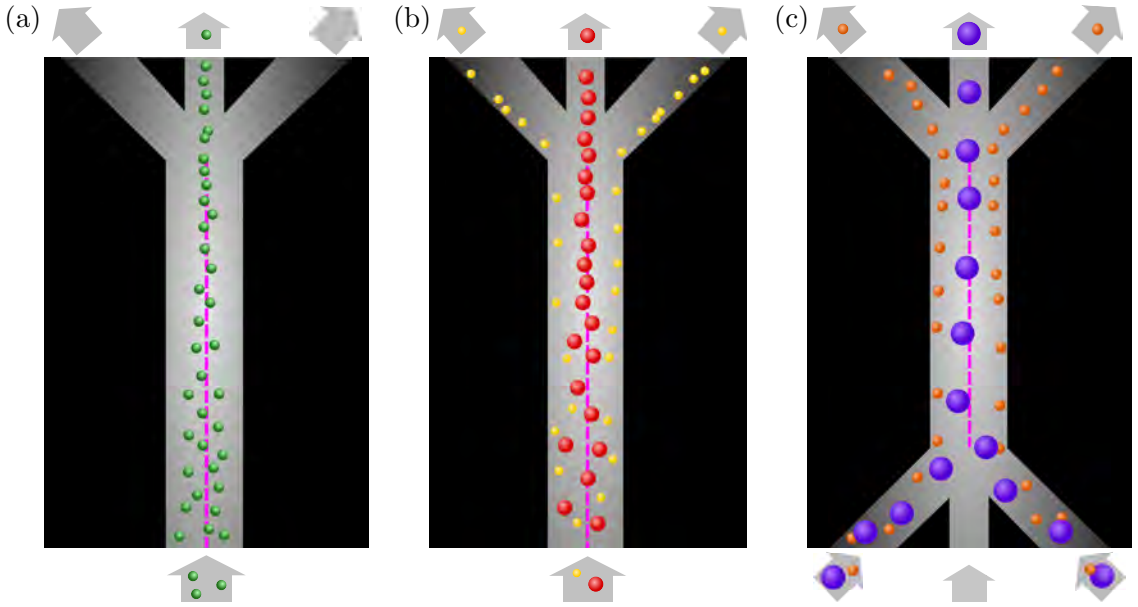

Figure 1.1 Top view of three different ways to manipulate particles by acoustophoresis, adapted from Ref. [8]. The acoustophoretic zone is the area where the fluid supports a standing pressure wave perpendicular to the particle flow. The wave is marked by its node in the central channel plane (magenta) and has antinodes at the channel walls. (a) Enrichment of the green particles as they are focused at the pressure node while some of the particle-free medium exits through side outlets. (b) The acoustic contrast factor is a material property that depends on the density and the compressibility. Here, the red particles have a positive acoustic contrast factor and are therefore focused at the pressure node, whereas the yellow particles, which have a negative contrast factor, are focused at the pressure antinodes. (c) Both the orange and the purple particles move towards the pressure node but because of the difference in particle size, the purple particles focus much faster.

depends on the particle size, density and compressibility (the force will be introduced in Section 4.2).

Figure 1.2 is a cross-sectional sketch the system in Figure 1.1 and show a typical system setup for acoustophoresis. It consists of a silicon chip with an etched microchannel of rectangular cross section and a glass lid on top, mounted on a piezoelectric actuator. Water is used as the suspending medium. A horizontal, half-wavelength, 1D standing pressure wave is induced perpendicular to the laminar water flow by vibrations of the actuator. We shall consider this setup throughout most of this thesis.

The separation sketched in Figure 1.1(b) has been demonstrated for particles with radii of several micrometres and a half-wavelength standing pressure wave at 2 Mhz in a channel of width $w = 350\,\mu\text{m}$ and height $h = 125\,\mu\text{m}$ [10]. However, for sufficiently small particle sizes another effect dominates their behaviour. This effect, called acoustic streaming, arises from large velocity gradients near the channel boundaries that generates

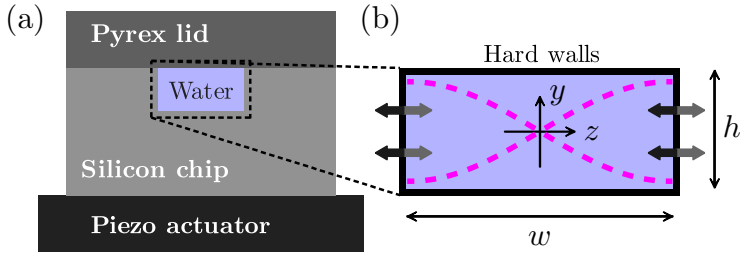

Figure 1.2 (a) Cross section of a typical system setup for acoustophoresis adapted from Ref.[9]. A silicon chip with an etched channel is mounted on a piezoelectric actuator that vibrates at MHz frequencies. (b) Sketch of the model system for an acoustophoretic zone in the channel. Due to the piezoelectric vibrations, the side walls oscillate in phase as indicated by the thick, grey arrows, and thereby create a horizontal standing pressure wave (magenta). The top and bottom walls are assumed to be infinitely hard and the width w and height h of the channel are of the order 100 µm.

rotational flow. For systems like the typical one sketched in Figure 1.2 operated at 2 MHz, the acoustic streaming dominates the behaviour of particles smaller than aprroximately 1 µm [11], thus complicating the manipulations sketched in Figure 1.1. It has, however, been demonstrated [1] that if 10-12 µm-sized seed particles are injected to the pressure node, focusing can be accomplished even for particles smaller than the approximate transition size of 1 µm.

In this thesis we investigate some of the effects of placing a single such seed particle at the pressure node. We estimate how the presence of the seed particle affects the radiation force acting on sub-micron particles. Furthermore, we derive an analytical expression for the acoustic streaming that arises from the seed particle, to examine how this affects the overall streaming pattern that influences sub-micron particles. To ease the analytical treatment this derivation is for an unbounded fluid, as opposed to the more realistic bounded geometry in Figure 1.2. Finally, we carry out numerical calculations of the streaming in a bounded geometry like the one in Figure 1.2, and compare it to the analytical result for an unbounded fluid.

1.2 Thesis outline

Chapter 2: Governing equations
We briefly go through the description of fluids and then present the relevant governing equations. We employ perturbation theory to derive first- and second-order expressions for these.

Chapter 3: Weak form modelling in COMSOL
This chapter is a brief introduction to the simulation software COMSOL, the finite element method and the weak formulation of a boundary value problem.

Chapter 4: Acoustofluidic theory
We derive the damped Helmholtz equation for the first-order fields and discuss viscosity in the bulk fluid. The second-order effects known as the acoustic radiation force and acoustic streaming are then introduced through well-known examples in rectangular channels. We use this introduction to motivate the investigation of the influence of a seed particle on these effects.

Chapter 5: Influence of a seed particle on the radiation force
We begin the investigation of a system containing a seed particle by examining how the acoustic fields scattered on it affect the radiation force on a small probe particle.

Chapter 6: Acoustic streaming generated by a rigid sphere
In this chapter we derive an expression for the acoustic streaming generated by a rigid spherical particle at the node of a standing pressure wave in an unbounded fluid.

Chapter 7: Influence of a seed particle on the streaming pattern
The analytical result from the previous chapter is used to estimate how the total streaming pattern in a channel changes due to the presence of a seed particle. Moreover, numerical calculations of the total streaming in both the absence and presence of the seed particle is performed, and the results are compared to the analytical predictions. Simulations of the trajectories of micron-sized and sub-micron-sized particles in the total streaming pattern are examined to see whether the seed particle has a significant effect on the particle motion.

Chapter 8: Conclusion and outlook
This chapter provides a summary of our findings and suggestions for future theoretical and numerical work.

Chapter 2

Governing equations

In this chapter we first define the basic continuum fields. The basic fluid mechanic theory is then presented and perturbation methods is used to derive the zeroth-, first- and second-order expressions for the governing equations. We shall use Einstein index notation unless otherwise stated, and standard vector calculus. Further details about the mathematical notation are provided in Section B.2 in Appendix B.

2.1 Definition of the continuum fields

In this thesis we shall use the Eulerian description of fluids, in which the spatial point $\boldsymbol{r}$ and the time t are independent variables. Furthermore, as the smallest length scale that we consider is of the order 100 nm, we shall assume the validity of the continuum hypothesis. The reader unfamiliar with these concepts are referred to Section B.1 in Appendix B.

We define the value of any field $F(\boldsymbol{r}, t)$ at the spatial point $\boldsymbol{r}$ at time t as an average value in some fluid particle of volume $\Delta V(\boldsymbol{r})$ around $\boldsymbol{r}$,

$$F(\boldsymbol{r}, t) = \left\langle F_{\text{mol}}(\boldsymbol{r'}, t) \right\rangle_{\boldsymbol{r'} \in \Delta V(\boldsymbol{r})} . \tag{2.1}$$

Let m_i and $\boldsymbol{v}_i$ denote the mass and velocity of the i'th molecule and let $i \in \Delta V$ denote all molecules contained in the volume $\Delta V(\boldsymbol{r})$ at time t. Then, we define the mass density $\rho(\boldsymbol{r}, t)$ and the velocity field $\boldsymbol{v}(\boldsymbol{r}, t)$ as

$$\rho(\boldsymbol{r}, t) \equiv \frac{1}{\Delta V} \sum_{i \in \Delta V} m_i, \tag{2.2a}$$

$$\boldsymbol{v}(\boldsymbol{r}, t) \equiv \frac{1}{\rho(\boldsymbol{r}, t) \Delta V} \sum_{i \in \Delta V} m_i \boldsymbol{v}_i. \tag{2.2b}$$

Notice how the velocity field is defined by the momentum density and not simply as the sum of the molecular velocities in the fluid particle.

2.2 Conservation of mass and momentum

We shall use two governing equations for non-relativistic fluid mechanics in this thesis and, for brevity, we omit explicitly writing the time and space dependencies of the fields. The first one, called the continuity equation, expresses that mass is conserved,

$$\partial_t \rho = -\boldsymbol{\nabla}\cdot(\rho \boldsymbol{v}). \tag{2.3}$$

The second is the equation of motion, which states that momentum density of fluid inside any region can change by advection, action of surface forces and action of body forces,

$$\partial_t(\rho \boldsymbol{v}) = -\boldsymbol{\nabla}\cdot(\rho \boldsymbol{v}\boldsymbol{v}) + \boldsymbol{\nabla}\cdot \boldsymbol{\sigma} + \boldsymbol{f}^{\text{body}}. \tag{2.4}$$

Here, $\boldsymbol{f}^{\text{body}}$ is the sum of all body forces and $\boldsymbol{\sigma}$ is the total stress tensor of rank two,

$$\boldsymbol{\sigma} = \eta\left[(\boldsymbol{\nabla}\boldsymbol{v}) + (\boldsymbol{\nabla}\boldsymbol{v})^T\right] + \left[\left(\eta_B - \frac{2}{3}\eta\right)(\boldsymbol{\nabla}\cdot\boldsymbol{v}) - p\right]\mathbf{I}, \tag{2.5}$$

where η is the dynamic shear viscosity, η_{B} the bulk viscosity, p the pressure and $\mathrm{I}_{ij} = \delta_{ij}$. In index notation σ_{ij} expresses the ith component of the friction force per area acting on a surface element oriented with its surface normal parallel to the jth unit vector $\boldsymbol{e}_j$. We shall ignore the body forces gravity and buoyancy. Furthermore, we shall assume that the coefficients η and η_B are constant in space and time at a given temperature. Then, the dynamic equation reduces to the well-known Navier-Stokes equation for compressible fluids,

$$\rho\left[\partial_t \boldsymbol{v} + (\boldsymbol{v}\cdot\boldsymbol{\nabla})\boldsymbol{v}\right] = -\boldsymbol{\nabla}p + \eta\nabla^2\boldsymbol{v} + \beta\eta\boldsymbol{\nabla}(\boldsymbol{\nabla}\cdot\boldsymbol{v}). \tag{2.6}$$

Here, we have introduced the viscosity ratio $\beta = \eta_B/\eta + 1/3$ for brevity. We shall work with the equation of motion both on the form of Eq. (2.4) and on form of the Navier-Stokes equation.

In addition to the two governing equations presented above, we shall also use the thermodynamic equation of state which relates the pressure to the density and entropy s,

$$p = p(\rho, s), \tag{2.7}$$

An isentropic (s constant) expansion to second order of the equation of state around some constant value p_0 yields

$$p(\rho) = p_0 + \left(\partial_\rho p\right)_{\rho_0}(\rho - \rho_0) + \frac{1}{2}\left(\partial_\rho^2 p\right)_{\rho_0}(\rho - \rho_0)^2 \tag{2.8a}$$

$$= p_0 + c_0^2(\rho - \rho_0) + \frac{1}{2}\left(\partial_\rho\, c_0^2\right)_{\rho_0}(\rho - \rho_0)^2. \tag{2.8b}$$

In the last expression we have introduced the speed of sound, c_0, which from thermodynamics is known to be defined as

$$c_0^2 \equiv \left(\frac{\partial p}{\partial \rho}\right)_s. \tag{2.9}$$

We shall not prove this directly but when we derive the acoustic wave equation we can identify it as the speed of sound. Apart from the relations described above we shall not consider thermal effects. Thus we have three equations to solve,

$$p = p(\rho), \tag{2.10a}$$
$$\partial_t \rho = -\boldsymbol{\nabla}\cdot(\rho \boldsymbol{v}), \tag{2.10b}$$
$$\partial_t(\rho \boldsymbol{v}) = -\boldsymbol{\nabla}\cdot(\rho \boldsymbol{v}\boldsymbol{v}) + \boldsymbol{\nabla}\cdot\boldsymbol{\sigma}. \tag{2.10c}$$

2.3 Perturbation theory

Eqs. (2.10a)-(2.10c) form a set of three coupled, partial differential equations with three unknown quantities and should thus be solvable. However, the non-linearities in Eq. (2.10c) make the equations analytically insolvable in any but a few special cases. We therefore have to settle for analytical approximations to treat other cases. These can be obtained with perturbation theory which deals with small corrections, called perturbations, to exact solutions.

We shall consider the exact solution to Eq. (2.10) for water where the three dependent variables are all constants,

$$p = p_0, \qquad \rho = \rho_0, \qquad \boldsymbol{v} = \boldsymbol{v}_0. \tag{2.11}$$

Let $\boldsymbol{v}_0 = \boldsymbol{0}$ such that the fluid is quiescent. Furthermore, ρ_0 is the density of water.

2.3.1 First-order perturbation theory

If the quiescent fluid is slightly perturbed by an acoustic wave we can write

$$p = p_0 + p_1, \qquad \rho = \rho_0 + \rho_1, \qquad \boldsymbol{v} = \boldsymbol{v}_1, \tag{2.12}$$

where

$$p_0 \gg |p_1|, \qquad \rho_0 \gg |\rho_1|, \qquad c_0 \gg |v_1|. \tag{2.13}$$

The maximum pressure perturbation that we will consider is $p_1 = 1$ MHz corresponding to a maximum density of $\rho_1 \sim 10^{-4}\rho_0$ for water. The maximum velocity perturbation that we will consider is $v_1 = 1$ m/s, which is much less than the isentropic speed of sound in water, $c_0 \approx 1500$ m/s. The pressure p_0 that p_1 should be compared to is related to the cohesive energy of water and is of the order $\rho_0 c_0^2 \approx 1$ GPa [12], which is much larger than 1 MHz. The perturbations that we consider are thus in the valid limits. Moreover, the hydrostatic pressure in microfluidic channels of height $h \sim 1$ mm is $\rho_0 g h \sim 10$ Pa which is negligible compared to the pressure perturbations.

If we insert Eq. (2.12) into Eqs. (2.10a)-(2.10c), the zeroth-order terms from the exact solution cancel out. If we assume that products of first-order terms, i.e. terms with subscript 1, are negligible compared to the first-order terms themselves, we are left with

the first-order governing equations

$$p_1 = c_0^2 \rho_1, \tag{2.14a}$$
$$\partial_t \rho_1 = -\rho_0 \boldsymbol{\nabla} \cdot \boldsymbol{v}_1, \tag{2.14b}$$
$$\rho_0 \partial_t \boldsymbol{v}_1 = \boldsymbol{\nabla} \cdot \boldsymbol{\sigma}_1. \tag{2.14c}$$

We note that ρ_0 is a constant that can be moved outside derivatives. Contrary to the original equations, these are linear. We can thus assume harmonic time dependence of all fields corresponding to a harmonic driving force without loss of generality,

$$\rho_1(\boldsymbol{r}, t) = \rho_1(\boldsymbol{r})\, \mathrm{e}^{-\mathrm{i}\omega t}, \tag{2.15a}$$
$$p_1(\boldsymbol{r}, t) = c_0^2\, \rho_1(\boldsymbol{r})\, \mathrm{e}^{-\mathrm{i}\omega t}, \tag{2.15b}$$
$$\boldsymbol{v}_1(\boldsymbol{r}, t) = \boldsymbol{v}_1(\boldsymbol{r})\, \mathrm{e}^{-\mathrm{i}\omega t}. \tag{2.15c}$$

Here, we introduce a complex phase but the physical fields are the real part of the expressions. It follows from the harmonic time dependence that a time derivative gives a factor $(-\mathrm{i}\omega)$ and Eq. (2.14) can therefore be rewritten as

$$p_1 = c_0^2 \rho_1, \tag{2.16a}$$
$$-\mathrm{i}\omega \rho_1 = -\rho_0 \boldsymbol{\nabla} \cdot \boldsymbol{v}_1, \tag{2.16b}$$
$$-\mathrm{i}\omega \rho_0 \boldsymbol{v}_1 = \boldsymbol{\nabla} \cdot \boldsymbol{\sigma}_1. \tag{2.16c}$$

In later chapters we shall use Eq. (2.16) both in the case of a viscid and an inviscid fluid. In the latter we can see in Eq. (2.5) that the divergence of the first-order stress tensor reduces to $\boldsymbol{\nabla} \cdot \boldsymbol{\sigma}_1 = -\boldsymbol{\nabla} p_1$ when the viscosity is set to zero, $\eta = \eta_\mathrm{B} = 0$. Furthermore, in the inviscid case the first-order velocity field has no vorticity, i.e. $\boldsymbol{\nabla} \times \boldsymbol{v}_1 = \boldsymbol{0}$. We can therefore perform a Helmholtz decomposition to define a velocity potential,

$$\boldsymbol{v}_1 = \boldsymbol{\nabla} \phi_1. \tag{2.17}$$

With the expression $\boldsymbol{\nabla} \cdot \boldsymbol{\sigma}_1 = -\boldsymbol{\nabla} p_1$ inserted in Eq. (2.16c), the first-order pressure and density can be expressed in terms of ϕ_1,

$$p_1 = \mathrm{i}\omega \rho_0\, \phi_1, \tag{2.18a}$$
$$\rho_1 = \mathrm{i} \frac{\rho_0 \omega}{c_0^2}\, \phi_1, \tag{2.18b}$$

It also follows from the harmonic time dependence that to first order, there are no time-averaged effects. By a time-average $\langle X \rangle$ of a quantity $X(t)$ with period τ we understand

$$\langle X \rangle \equiv \frac{1}{\tau} \int_0^\tau \mathrm{d}t\, X(t), \tag{2.19}$$

and it is clear that $\langle \mathrm{Re}[\exp(-\mathrm{i}\omega t)] \rangle = \langle \cos(\omega t) \rangle = 0$.

2.3.2 Second-order perturbation theory

To investigate time-averaged effects it is necessary to proceed to second order,

$$p = p_0 + p_1 + p_2, \tag{2.20a}$$
$$\rho = \rho_0 + \rho_1 + \rho_2, \tag{2.20b}$$
$$\boldsymbol{v} = \boldsymbol{0} \ + \boldsymbol{v}_1 + \boldsymbol{v}_2. \tag{2.20c}$$

When Eqs. (2.20a)-(2.20c) are inserted into Eqs. (2.10a)-(2.10c) the zeroth-order terms cancel out again but so do the first-order terms. Neglecting terms of higher order than two yields

$$p_2 = c_0^2 \rho_2 + \frac{1}{2} \left(\partial_\rho c_0^2 \right)_{\rho_0} \rho_1^2, \tag{2.21a}$$
$$\partial_t \rho_2 = -\rho_0 \boldsymbol{\nabla} \cdot \boldsymbol{v}_2 - \boldsymbol{\nabla} \cdot (\rho_1 \boldsymbol{v}_1), \tag{2.21b}$$
$$\partial_t (\rho_0 \boldsymbol{v}_2 + \rho_1 \boldsymbol{v}_1) = -\rho_0 \boldsymbol{\nabla} \cdot (\boldsymbol{v}_1 \boldsymbol{v}_1) + \boldsymbol{\nabla} \cdot \boldsymbol{\sigma}_2. \tag{2.21c}$$

When the driving force is harmonic in time it follows that in steady state the second order fields must be harmonic with the same period. Hence, according to Fourier analysis they can be decomposed into a sum of different frequencies and a constant term. Since the time-average of a non-zero constant term is also non-zero, we can not in general assume that $\langle p_2 \rangle = \langle \rho_2 \rangle = \langle \boldsymbol{v}_2 \rangle = 0$. However, a time derivative eliminates the constant terms so $\langle \partial_t p_2 \rangle = \langle \partial_t \rho_2 \rangle = \langle \partial_t \boldsymbol{v}_2 \rangle = 0$. After we have taken the time average of Eqs. (2.21b) and (2.21c), we obtain

$$0 = \rho_0 \boldsymbol{\nabla} \cdot \langle \boldsymbol{v}_2 \rangle + \boldsymbol{\nabla} \cdot \langle \rho_1 \boldsymbol{v}_1 \rangle \,, \tag{2.22a}$$
$$0 = \boldsymbol{\nabla} \cdot (\langle \boldsymbol{\sigma}_2 \rangle - \rho_0 \langle \boldsymbol{v}_1 \boldsymbol{v}_1 \rangle) \,, \tag{2.22b}$$

We do not need Eq. (2.21a) nor its time average as we can solve Eq. (2.22) for $\boldsymbol{v}_2$ and p_2 without the relation between p_2 and ρ_2.

Chapter 3

Weak form modelling in COMSOL

In Chapter 7 we present simulation results obtained in the commercially available software COMSOL Multiphysics. We shall use COMSOL as tool rather than as a subject in itself. Therefore, the introduction to COMSOL given in this chapter is brief. It is based on the notes of Nielsen [13] and Bruus [14].

3.1 The finite element method and boundary conditions

COMSOL is a simulation software in which the finite element method is applied. The core of this method is to discretise the physical fields by approximating them with a superposition of basis functions or test functions, as they are called in COMSOL. The discretisation is shown in Figure 3.1. It is established by placing a grid on the computational domain. Each grid point is connected to other grid points to form triangular mesh elements. Mesh elements that share a grid node make a mesh cell. For every physical field $g(\boldsymbol{r})$, a test function $\hat{g}_n(\boldsymbol{r})$ is defined on the n'th mesh cell. Each test function is unity at the central grid node in its associated mesh cell, and decreases continuously to zero at the mesh cell boundary. The physical field $g(\boldsymbol{r})$ is then approximated by

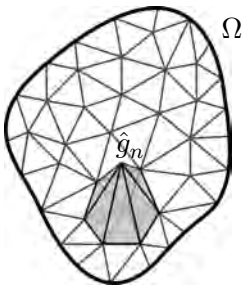

Figure 3.1 Sketch of the discretisation of the computation domain Ω into grid points that are connected to form triangular mesh elements, adapted from [13]. Th nth COMSOL test function $\hat{g}_n(\boldsymbol{r})$ is sketched as a linear function (out of the plane of the sketch) defined on a the gray mesh cell. It attains the value 1 at the nth grid node and 0 on the boundary of the cell.

$$g(\boldsymbol{r}) = \sum_n C_n^g \, \hat{g}_n(\boldsymbol{r}), \tag{3.1}$$

where the C_n^g is the coefficient to the n'th test function associated with the physical field g.

COMSOL is set up to handle problems formulated as continuity equations

$$\boldsymbol{\nabla}\cdot\boldsymbol{J}[g(\boldsymbol{r})] - \boldsymbol{F}(\boldsymbol{r}) = \boldsymbol{0}, \tag{3.2}$$

where g is the physical field described by the equation, $\boldsymbol{F}$ a generalised driving force and $\boldsymbol{\nabla}\cdot\boldsymbol{J}$ a Cartesian divergence of a generalised flux $\boldsymbol{J}$ that depends linearly on g. Both $\boldsymbol{J}$ and $\boldsymbol{F}$ are tensors, but the the rank of $\boldsymbol{J}$ is one higher than that of $\boldsymbol{F}$, which can be zero (corresponding to a scalar) or higher. For simplicity, we consider a scalar F.

Insertion of the approximation in Eq. (3.1) into Eq. (3.2) yields a defect $d(\boldsymbol{r})$,

$$\boldsymbol{\nabla}\cdot\boldsymbol{J}\left[\sum_n C_n^g \, \hat{g}_n(\boldsymbol{r})\right] - F(\boldsymbol{r}) = d(\boldsymbol{r}). \tag{3.3}$$

COMSOL seeks to make the projection of the defect $d(\boldsymbol{r})$ on every test function vanish, i.e. it tries to fulfil the equation

$$\langle \hat{g}_m, d\rangle \equiv \int_\Omega \hat{g}_m(\boldsymbol{r}) d(\boldsymbol{r}) \mathrm{d}\boldsymbol{r} \, = \int_\Omega \hat{g}_m(\boldsymbol{r}) \Big[\boldsymbol{\nabla}\cdot\boldsymbol{J}[g(\boldsymbol{r})] - F(\boldsymbol{r})\Big] \mathrm{d}\boldsymbol{r} \, = 0, \quad \text{for all } m. \tag{3.4}$$

Eq. (3.4) is known as the weak form of the problem. The strong form in Eq. (3.2) is approximately satisfied when the weak form is.

The problem is linear and can thus be written on matrix form or, equivalently, with index notation. We suppress the spatial dependence and define $f_m = \langle \hat{g}_m, F\rangle$ and $K_{mn} = \langle \hat{g}_m, \boldsymbol{\nabla}\cdot\boldsymbol{J}[\hat{g}_n]\rangle$, such that Eq. (3.4) can be written as

$$K_{mn} \, C_n^g = F_m. \tag{3.5}$$

COMSOL determines the coefficients C_n^g by matrix inversion.

To see how boundary conditions are implemented we apply the divergence theorem on Eq. (3.4) to obtain

$$\int_{\partial\Omega} \hat{g}_m \boldsymbol{n}\cdot\boldsymbol{J} \, \mathrm{d}a \, + \int_\Omega \big[(-\boldsymbol{\nabla}\hat{g}_m)\cdot\boldsymbol{J} - \hat{g}_m F\big] \mathrm{d}\boldsymbol{r} \, = 0. \quad \text{for all } m. \tag{3.6}$$

A Neumann boundary condition $\boldsymbol{n}\cdot\boldsymbol{J} = N(\boldsymbol{r})$ for $\boldsymbol{r} \in \partial\Omega$ is now straightforward to impose. Any other boundary condition can be written as $R(\boldsymbol{r}) = 0$ for $\boldsymbol{r} \in \partial\Omega$. It can be imposed by introducing an extra degree of freedom, a so-called Lagrange multiplier field $\lambda(\boldsymbol{r}) = \boldsymbol{n}\cdot\boldsymbol{J}$, which is defined only on the boundary. Associated with it is a set of test functions $\hat{\lambda}_m(\boldsymbol{r})$, such that the weak form of the general boundary condition becomes $\langle \hat{\lambda}_m, R\rangle = 0$ for all m. This is added to Eq. (3.6), which becomes

$$\int_{\partial\Omega} \Big[\hat{g}_m \lambda + \hat{\lambda}_m R\Big] \, \mathrm{d}a \, + \int_\Omega \big[(-\boldsymbol{\nabla}\hat{g}_m)\cdot\boldsymbol{J} - \hat{g}_m F\big] \mathrm{d}\boldsymbol{r} \, = 0. \quad \text{for all } m. \tag{3.7}$$

As $\hat{\lambda}_m$ is independent of $\hat{g}_m$ this form still enforces $\langle \hat{\lambda}_m, R\rangle = 0$ and at the same time determines $\lambda(\boldsymbol{r})$. A common boundary condition is the Dirichlet condition $g(\boldsymbol{r}) = D(\boldsymbol{r})$ or $R(\boldsymbol{r}) = g(\boldsymbol{r}) - D(\boldsymbol{r})$ on the general form.

Chapter 4

Acoustofluidic theory

In this chapter we use the perturbation theory developed in the previous chapter to derive the linear wave equation for the first-order pressure. We also begin the investigation of the two time-averaged second-order effects, the acoustic radiation force and the acoustic streaming, by reviewing both in the typical setup in Figure 1.2.

4.1 The acoustic wave equation

The first-order governing equations derived in the previous chapter are

$$p_1 = c_0^2 \rho_1, \tag{4.1a}$$

$$\partial_t \rho_1 = -\rho_0 \boldsymbol{\nabla} \cdot \boldsymbol{v}_1, \tag{4.1b}$$

$$\rho_0 \partial_t \boldsymbol{v}_1 = -\boldsymbol{\nabla} p_1 + \eta \nabla^2 \boldsymbol{v}_1 + \beta \eta \boldsymbol{\nabla}(\boldsymbol{\nabla} \cdot \boldsymbol{v}_1). \tag{4.1c}$$

We note that ρ_0 is a constant that commutes with derivatives, so when taking the time derivative of Eq. (2.16b) we may write

$$\partial_t^2 \rho_1 = -\boldsymbol{\nabla} \cdot (\rho_0 \partial_t \boldsymbol{v}_1). \tag{4.2}$$

An equation for ρ_1 is obtained by insertion of Eq. (4.1c) into Eq. (4.2) followed by elimination of p_1 and $\boldsymbol{\nabla} \cdot \boldsymbol{v}_1$ by use of Eq. (4.1a) and Eq. (4.1b), respectively,

$$\partial_t^2 \rho_1 = \nabla^2 p_1 - (1+\beta)\eta \nabla^2 (\boldsymbol{\nabla} \cdot \boldsymbol{v}_1) = c_0^2 \left[1 + \frac{(1+\beta)\eta}{\rho_0 c_0^2} \partial_t \right] \nabla^2 \rho_1. \tag{4.3}$$

As argued previously, we can assume harmonic time dependence expressed in Eq. (2.15) without loss of generality. Therefore, a time derivative corresponds to a factor $(-\mathrm{i}\omega)$. Moreover, it is evident from Eq. (4.1a) that we can substitute p_1/c_0 for ρ_1, and if we also define a wavenumber $k_0 = \omega/c_0$ we arrive at

$$\nabla^2 p_1 = -\frac{1}{1 - \mathrm{i}2\Gamma} k^2 p_1, \qquad \Gamma = \frac{(1+\beta)\eta\omega}{2\rho_0 c_0^2}. \tag{4.4}$$

If the frequency of the acoustic fields are in the Mhz range, which is the range relevant for lab-on-a-chip systems, one finds $\Gamma \approx 10^{-5} \ll 1$ using parameter values for water at 300 K (see Table A.1 in Appendix A), and $\omega = 2\pi f$ where $f = 2$ MHz. Thus, we can to a good approximation write Eq. (4.4) in the form of a Helmholtz equation for a damped wave,

$$\nabla^2 p_1 = -k^2 p_1, \qquad k = (1 + \mathrm{i}\Gamma)k_0 = (1 + \mathrm{i}\Gamma)\frac{\omega}{c_0}. \tag{4.5}$$

We are now able to identify Γ as a viscous damping factor and recognise c_0 as the speed of sound. Furthermore, since $\Gamma \ll 1$, we see that viscosity is negligible in the bulk part of the acoustic wave which is a result we use in the discussion of the acoustic radiation force.

4.2 Acoustic radiation force

The acoustic radiation force is a second-order, time-averaged effect. It arises from the scattering of acoustic waves on particles suspended in a fluid subjected to an acoustic field. The acoustic radiation force on compressible and incompressible particles was first analysed in 1934 by King [15] and in 1955 by Yosioka and Kawasima [16]. In both cases the results were restricted to particles suspended in an incompressible, inviscid fluid, and they were valid only in the limit where the particle radius a is much smaller than the acoustic wavelength λ. In 1962 Gorkov [17] summarised and generalised their work. An extension of his classic theory was provided in 2012 by Settnes and Bruus [18] who included viscosity effects, and in 2015 by Karlsen and Bruus [19] who included both the effect of viscosity and heat conduction.

In this section we shall not provide a thorough derivation of an analytical expression for the acoustic radiation force. Instead, we shall merely outline the derivation by explaining the main arguments and stating a few intermediate results.

As shown in the discussion of the acoustic wave equation, it is a good approximation to neglect viscosity effects in the bulk of the fluid. Moreover, we shall ignore heat conduction, since thermal effects are negligible far from thermal boundary layers [19]. The ideal theory of Gorkov is thus sufficient in this thesis. We shall follow the derivation of Bruus [20] who presents Gorkov's theory, while filling in some details originally left out.

The starting point is first-order and time-averaged second-order perturbations on a quiescent fluid as described in Section 2.3 by Eqs. (2.11)-(2.22). The acoustic radiation force on a spherical particle suspended in the fluid is calculated as the surface integral of the time-averaged second-order pressure $\langle p_2 \rangle$ and momentum flux tensor $\rho_0 \langle \boldsymbol{v}_1 \boldsymbol{v}_1 \rangle$ over a fixed surface outside the sphere,

$$\boldsymbol{F}^{\mathrm{rad}} = -\int_{\partial\Omega} \mathrm{d}a \, \left[\langle p_2 \rangle \, \boldsymbol{n} + \rho_0 \, \langle (\boldsymbol{n} \cdot \boldsymbol{v}_1)\boldsymbol{v}_1 \rangle \right], \tag{4.6a}$$

$$= -\int_{\partial\Omega} \mathrm{d}a \, \left\{ \left[\frac{1}{2}\kappa_0 \left\langle p_1^2 \right\rangle - \frac{1}{2}\rho_0 \left\langle \boldsymbol{v}_1^2 \right\rangle \right] + \rho_0 \, \langle (\boldsymbol{n} \cdot \boldsymbol{v}_1)\boldsymbol{v}_1 \rangle \right\}, \tag{4.6b}$$

where the last expression can be obtained by use of first- and second-order perturbed governing equations. If no body forces influence the particle, the integral can be calculated

using any fixed surface $\partial\Omega$ encompassing the particle [19]. Introducing a velocity potential ϕ_1 given by $\boldsymbol{v}_1 = \boldsymbol{\nabla}\phi_1$, we can for sufficiently weak incoming acoustic fields write the first-order fields as a sum of the incoming and scattered fields,

$$\phi_1 = \phi_{\text{in}} + \phi_{\text{sc}}, \qquad \boldsymbol{v}_1 = \boldsymbol{v}_{\text{in}} + \boldsymbol{v}_{\text{sc}}, \qquad p_1 = p_{\text{in}} + p_{\text{sc}}, \qquad \rho_1 = \rho_{\text{in}} + \rho_{\text{sc}}. \tag{4.7}$$

As we assume that the particle radius is much smaller than the acoustic wavelength, $a \ll \lambda$, the particle behaves as a point scatterer. This means that the scattered field can be expressed as a time-retarded multipole expansion if the co-ordinate system is centred at the scatterer. In the limit $a \ll \lambda$ the monopole and dipole terms dominate, simplifying the calculations. Through physical considerations one can arrive at the far-field expression

$$\phi_{\text{sc}}(r,t) = -f_0 \frac{a^3}{3\rho_0} \frac{\partial_t \rho_{\text{in}}(t - r/c_0)}{r} - f_1 \frac{a^3}{2} \boldsymbol{\nabla} \cdot \left(\frac{\boldsymbol{v}_{\text{in}}(t - r/c_0)}{r} \right), \tag{4.8}$$

where ρ_{in} and $\boldsymbol{v}_{\text{in}}$ are the incoming fields and $\boldsymbol{r}$ is the position vector. For convenience, the unknown factors are chosen as $\frac{1}{3}f_0$ and $\frac{1}{2}f_1$, where f_0 and f_1 are known as the monopole and dipole coefficients. If we evaluate the integral over a surface outside the acoustic boundary layer but close to the particle surface, e.g. $r \approx a + 5\delta$ where $\delta \ll a$, the retardation time is negligible in comparison to the oscillation period of the field, $r/c_0 \approx a/c_0 \ll \lambda/c_0$. Therefore, we can replace the time-retarded argument $t - r/c_0$ of the fields with the instantaneous argument t.

Next, it is evident from Eq. (4.7) that the terms $\langle p_1^2 \rangle$ and $\langle v_1^2 \rangle$ in Eq. (4.6b) contain squares of the incoming fields, squares of the scattered fields and mixed terms, e.g. ϕ_{in}^2, ϕ_{sc}^2 and $\phi_{\text{in}}\phi_{\text{sc}}$. If the particle is acoustically indistinguishable from the surrounding fluid there would be no scattering and hence no radiation force. Thus, the terms corresponding to ϕ_{in}^2 do not contribute to the radiation force. Moreover, the terms corresponding to ϕ_{sc}^2 are negligible compared to the mixed terms since the former are proportional to the particle small volume a^3 and the latter to its even smaller square a^6. Thus, it suffices to keep only the mixed terms in the calculations. After several mathematical manipulations of Eq. (4.6b), the following expression is obtained in index notation,

$$F_i^{\text{rad}} = -\int_{\partial\Omega} \mathrm{d}\boldsymbol{r}\, \rho_0 \left\langle v_i^{\text{in}} \left(\partial_j \partial_j \phi_{\text{sc}} - \frac{1}{c_0^2} \partial_t^2 \phi_{\text{sc}} \right) \right\rangle = -\int_{\partial\Omega} \mathrm{d}\boldsymbol{r}\, \rho_0 \left\langle v_i^{\text{in}}\, \Box^2 \phi_{\text{sc}} \right\rangle \tag{4.9}$$

The last expression in Eq. (4.9) is written because the final non-zero result for the radiation force comes from the singularity in ϕ_{sc} that the d'Alembert operator $\Box^2$ picks up at $\boldsymbol{r} = \boldsymbol{0}$. Then, insertion of Eq. (4.8) and several rewritings yield

$$\boldsymbol{F}^{\text{rad}} = -\pi a^3 \left[\frac{2\kappa_0}{3} \operatorname{Re}[f_1^* p_{\text{in}}^* \boldsymbol{\nabla} p_{\text{in}}] - \rho_0 \operatorname{Re}[f_2^* \boldsymbol{v}_{\text{in}}^* \cdot \boldsymbol{\nabla} \boldsymbol{v}_{\text{in}}] \right], \tag{4.10}$$

where p_{in} and $\boldsymbol{v}_{\text{in}}$ are evaluated at $\boldsymbol{r} = \boldsymbol{0}$, and an asterisk denotes complex conjugation. If the spatial parts of the fields are real, this expression reduces to

$$\boldsymbol{F}_{\text{rf}}^{\text{rad}} = -\frac{4\pi}{3} a^3 \boldsymbol{\nabla} \left[\frac{1}{2} \operatorname{Re}[f_0]\, \kappa_0 \left\langle p_{\text{in}}^2 \right\rangle - \frac{3}{4} \operatorname{Re}[f_1]\, \rho_0 \left\langle v_{\text{in}}^2 \right\rangle \right]. \tag{4.11}$$

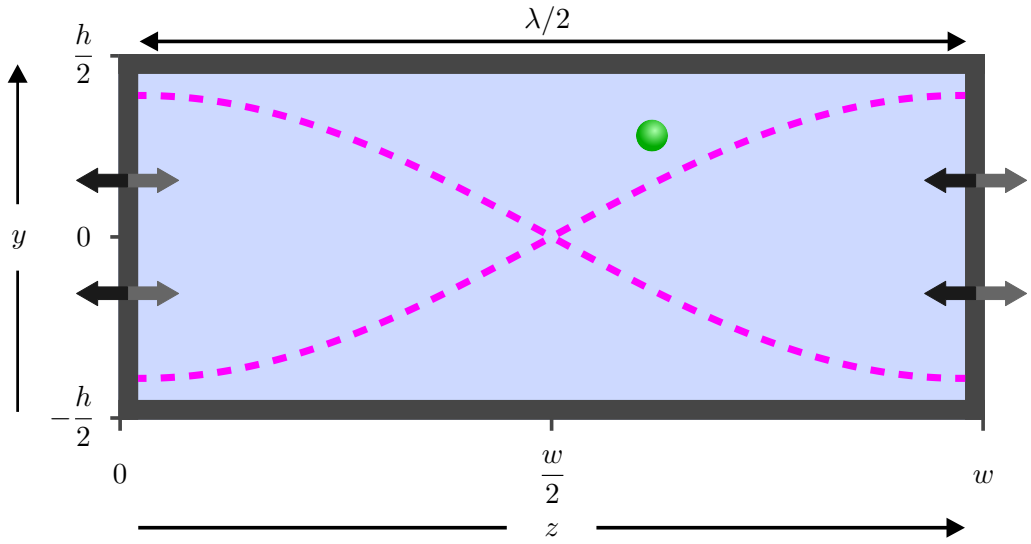

Figure 4.1 Cross section of a channel with oscillating side walls indicated by the grey arrows. The fluid (light blue) supports a horizontal standing pressure wave (magenta) with an node at the central plane and antinodes at the side walls. The pressure field and the other acoustic fields are scattered by the green particle which thus experience a radiation force.

Considerations about the scattered fluid mass and particle velocity lead to the expressions for the monopole coefficient f_0 and dipole coefficient f_1, respectively,

$$f_0 = 1 - \tilde{\kappa}, \quad \tilde{\kappa} = \frac{\kappa'}{\kappa_0}, \qquad f_1 = \frac{2(\tilde{\rho} - 1)}{2\tilde{\rho} + 1}, \quad \tilde{\rho} = \frac{\rho'}{\rho_0}. \tag{4.12}$$

Here, the particle and medium parameters are denoted by a prime and a subscript 0. The expression in Eq. (4.11) reduces further when the incident fields are standing waves. We consider a 1D half-wavelength standing pressure wave, given by $p_1(z) = p_a \cos(kz)\cos(\omega t)$, in the channel of rectangular cross section sketched in Figure 4.1. If $k_0 = 2\pi/\lambda = \omega/c_0$ is the wavenumber where $\lambda = 2w$, Eq. (4.11) reduces further to

$$\boldsymbol{F}_{\mathrm{sw}}^{\mathrm{rad}} = 4\pi\, \Phi(\tilde{\kappa}, \tilde{\rho})\, ka^3 E_{ac} \sin(2kz)\, \boldsymbol{e}_z \approx 2\,\mathrm{fN}, \tag{4.13}$$

where

$$\Phi(\tilde{\kappa}, \tilde{\rho}) = \frac{1}{3} f_0(\tilde{\kappa}) + \frac{1}{2} f_1(\tilde{\rho}), \qquad E_{\mathrm{ac}} = \frac{p_{\mathrm{a}}^2}{4\rho_0 c_0^2}. \tag{4.14}$$

Here, Φ is the acoustic contrast factor mentioned in Chapter 1 and E_{ac} is the acoustic energy density. The value in Eq. (4.13) is evaluated at $z = \frac{w}{4}$ where the sine is unity, making it a maximum. Moreover, it is evaluated for a polystyrene particle of radius $a = 100$ nm in water and a pressure amplitude of $p_{\mathrm{a}} = 1$ MPa. The density and compressibility of polystyrene contained in the contrast factor Φ are listed in Table A.1. The reason for using polystyrene is that the material's density and compressibility are similar to those of water

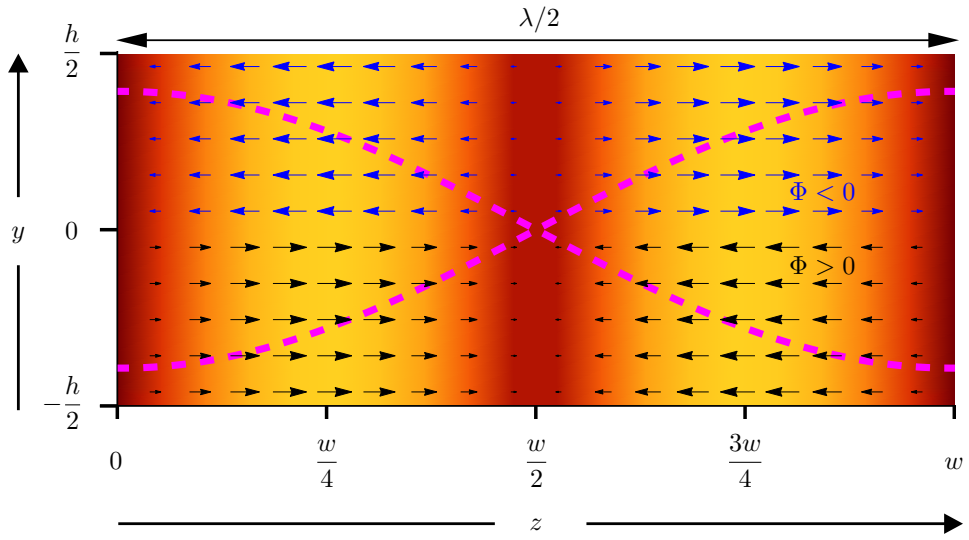

Figure 4.2 Colour and vector plots of the radiation force $\boldsymbol{F}_{\mathrm{sw}}^{\mathrm{rad}}$ for a half-wavelength ($\lambda/2$) standing pressure wave (magenta) with a central node in a channel of height h and width w. The colour and arrow size vary from dark red and no arrow (zero force magnitude) to bright yellow and largest arrow (maximum force magnitude). The arrows point in the direction of the force which is plotted for a negative acoustic contrast factor in the upper half-plane (blue) and a positive in the lower half-plane (black). The force attains its maximum at $z = \frac{w}{4}$ and $z = \frac{3w}{4}$. The minimum is attained at $z = 0$, $z = \frac{w}{2}$ and $z = w$.

(see the table), as is the case for many biological particles. As the force is proportional to the particle radius cubed, it is approximately 2 pN for a particle of radius $a = 1$ µm.

As evident from Eqs. (4.12) and (4.14), the sign of the acoustic contrast factor depends on the density and compressibility of the particle relative to the suspending medium. Particles with a positive acoustic contrast factor will experience a force towards the pressure node, whereas particles with a negative contrast factor will experience a force towards the nearest antinode at the walls.

We notice that the monopole coefficient tends towards 1 as the compressibility goes to zero corresponding to an infinitely hard material. Moreover, the dipole coefficient f_1 tends towards the values -2 and 1 for particles much lighter and denser than the suspending medium, respectively. We also notice that the force is zero at the pressure node ($z = \frac{w}{2}$), which, as we will see in the next section, is the reason that the acoustic streaming complicates the focusing and separation of particles.

The radiation force for a standing wave given in Eq. (4.13) is plotted in Figure 4.2 for a half-wavelength standing pressure wave with a node in the channel centre. The plot includes both the case of a positive and negative acoustic contrast factor. As seen in the argument of the sine in Eq. (4.13), the force has twice the wavelength of the fields that induce it. We see this in the figure, where both the pressure wave and the force have nodes in the channel centre, but the force has antinodes half-way between the centre and the walls, whereas the pressure has antinodes at the walls.

4.3 Acoustic streaming

Acoustic streaming is, like the radiation force, a second-order time-averaged effect generated by an oscillating acoustic field. It originates either from bulk attenuation of acoustic momentum or from boundary interaction [21]. In this thesis, only the latter is studied.

The presence of a solid, hard wall boundary, that does not yield to the velocity of the liquid, forces the amplitude of the acoustic velocity field to decay from its bulk value to zero at the boundary. This transition takes place within a thin region, the so-called acoustic boundary layer, thus generating large velocity gradients and, with that, large viscous stresses. As a consequence of this and the non-linearity of the governing equations, a steady (time-averaged) flow field parallel to the boundary is generated. This flow within the boundary layer is known as inner boundary layer streaming or Schlichting streaming, and it drives a steady flow in the entire fluid, referred to as outer boundary layer streaming or Rayleigh streaming [22].

The amplitude of the streaming is usually much lower than the amplitude v_a of the oscillating velocity field [23], which itself is much lower than the speed of sound c_0 in order for the perturbation theory to be valid. We stress these relations because fluid flows at velocities much lower than the speed of light can be approximated as incompressible, and because we shall use this approximation later in this section.

The boundary layer thickness δ depends on the angular frequency ω of the oscillating field and on the kinematic viscosity $\nu = \frac{\rho}{\eta}$ of the fluid, where ρ is its density and η its dynamic viscosity,

$$\delta = \sqrt{\frac{2\nu}{\omega}} \approx 0.5\ \mu\mathrm{m}. \tag{4.15}$$

The value is calculated for water, for which parameter values are listed in Table A.1, and the frequency $f = 2$ Mhz, which is typical for microparticle acoustophoresis. The expression in Eq. (4.15) is justified in Chapter 6.

Figure 4.3 shows both the inner and the outer streaming generated by a half-wavelength standing pressure wave. Figure 4.3(a) shows a sketch of the streaming in a shallow, infinite, parallel-plate channels, whereas Figure 4.3(b) shows the numerically calculated streaming in a water-channel of rectangular cross section. We shall not go into details about the numerical calculation here as the result merely serves to show the effect of the side walls on the streaming pattern.

A particle present in such steady streaming patterns will experience a force that drags it with the flow. The drag force on a rigid spherical particle of radius a moving with the velocity $\boldsymbol{v}^\mathrm{p}$ in the bulk of an incompressible fluid is [25, chap. 3]

$$\boldsymbol{F}^\mathrm{drag} = 6\pi\eta a(\boldsymbol{v} - \boldsymbol{v}^\mathrm{p}), \tag{4.16}$$

where $\boldsymbol{v}$ is the velocity of the fluid at the given position in the absence of the particle. As argued earlier, the fluid is indeed incompressible on the streaming time scale. The linear dependency on the fluid velocity relative to the particle velocity is only valid for low Reynolds numbers, i.e. for

$$Re = \frac{v^\mathrm{p} a}{\nu} \ll 1, \tag{4.17}$$

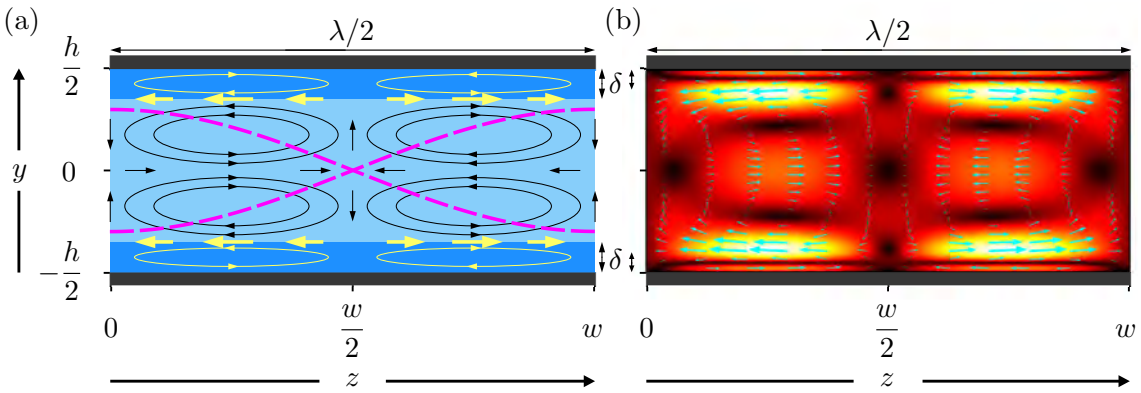

Figure 4.3 (a) Sketch of the acoustic streaming in shallow, infinite, parallel-plate channels generated by a standing pressure wave (dashed, magenta lines) of wavelength λ parallel to the plates, adapted from [24]. The inner streaming (yellow arrows) is confined to the boundary layer (dark shade blue) of approximate thickness δ, but it drives the outer streaming (black arrows) in the bulk liquid (light shade blue). (b) Numerically determined streaming in a water-channel of rectangular cross section of width $w = 380$ µm and height $h = 160$ µm supporting a half-wavelength, horizontal, standing pressure wave with a node in the $y = 0$ plane. The dimensions correspond to a resonance frequency of 1.96 Mhz and the viscosity was increased by a factor 300 in order to make the boundary layers visible. The cyan arrows show the direction of the streaming while the normalised magnitude is given by both the length of the arrows and the colour, ranging from the maximum (largest arrows and white colour) to 0 (no arrow and black colour).

where ν is the kinematic viscosity of the fluid. As typical parameter values for the rectangular system with water as the medium, we use the experimental results reported in Ref. [24]. The authors report maximum steady particle velocities of $v^{\mathrm{p}} = 63$ µm/s for spherical polystyrene particles of radius 269 nm at the acoustic energy density $E_{\mathrm{ac}} = 65$ J/m^3 corresponding to an amplitude of $v_{\mathrm{a}} = 0.51$ m/s for the oscillating velocity field. Using the value $\nu = 8.567 \times 10^{-7}$ m^2 s^{-1} from Table A.1 we arrive at $Re \approx 10^{-4} \ll 1$. Thus, Eq. (4.17) is valid for sub-micron particles under typical acoustophoretic conditions. Setting $\boldsymbol{v}^{\mathrm{p}} = \mathbf{0}$ and equating Eqs. (4.13) and (4.16) with the sine set to 1 leads to the critical particle size

$$a_{\mathrm{c}} = \sqrt{\frac{3\eta v}{2k\Phi E_{\mathrm{ac}}}} \approx 0.5 \text{ µm}. \tag{4.18}$$

The value is calculated for polystyrene in water, $v = 50$ µm/s, $E_{\mathrm{ac}} = 50$ J/m^3, and a wavelength $\lambda = 190$ µm corresponding to a channel width $w = 380$ µm. The values for η and the relevant parameters in Φ are given in Table A.1 and Φ is given by Eqs. (4.12) and (4.14). We use these values because they are typical for experiments [24] and therefore yield a good estimate of the critical radius. We have set the sine to unity, which means that we have used the maximum radiation force in the calculation. However, $v = 50$ µm/s is a typical maximum streaming velocity, so we have also used the maximum drag force.

The value $a_c = 0.5$ µm expresses that the motion of particles with a radius larger than 0.5 µm is dominated by the radiation force, whereas the motion of particles a smaller radius is dominated by the drag force. The motion of particles with a radius close to 0.5 µm will be influenced by both forces.

Sub-micron particles, for which the drag force dominates, will thus follow the streaming sketched in Figure 4.3. At the pressure node, where the radiation force vanishes, they will move towards either the top or bottom boundary layer, whichever is nearest. Then, they will follow one of four the circulating flows. At $z = \frac{w}{4}$ and $z = \frac{3w}{4}$ they are half-way between the pressure node and the side walls. Here, the radiation force attains its maximum (see Figure 4.2), which has direction inwards for particles with a positive contrast factor Φ. Particles with $\Phi > 0$ will thus slow down a little when they are half-way, but they will continue following the streaming pattern, since the drag force magnitude is larger than the radiation force magnitude. Particle focusing and separation thus becomes impossible. In the next chapters we investigate whether some of the effects of a seed particle at the channel centre make it possible to focus sub-micron particles even in the presence of these circulating flows.

Chapter 5

Influence of a seed particle on the radiation force

As mentioned in Chapter 1 it has been demonstrated that the presence of seed particles with radii of $a_s = 10 - 12$ µm in the centre of a rectangular channel makes it possible to focus sub-micron particles [1] despite the circulating flow. Our goal in this chapter is to examine how the fields scattered by a seed particle in the centre change the acoustic radiation force exerted on a sub-micron probe particle.

The system is sketched schematically in Figure 5.1, where we have moved the origin to the seed particle centre. Except for the seed particle it is the same system as those sketched in Figures 4.2 and 4.3. The side walls oscillate to sustain a half-wavelength standing pressure wave and thereby generates a circulating streaming flow. The flow drags a sub-micron probe particle towards the channel centre if it is close to $z = 0$, and towards the channel top or bottom if it is near $y = 0$. The acoustic fields are scattered by the seed particle and the scattered fields affect the radiation force on the probe particle. As mentioned above, this influence is the subject of this chapter. A rigid seed particle will, however, also generate a boundary layer around its surface which can create another streaming pattern, thereby changing the overall streaming pattern. This effect is the subject of Chapters 6 and 7.

One of two main results of this chapter is that the effect from the seed particle on the radiation force exerted on particles with water-like acoustic properties is a contribution that is at the maximum one order of magnitude lower than the original force (the force in the absence of the seed particle).

The other main result is that the introduction of a seed particle brings a new length scale into the problem: the seed particle radius a_s. As we consider an acoustic wavelength λ that is almost of the order 1 mm, and a seed particle radius of the order 10 µm , the latter will affect the spatial derivatives of the acoustic fields. In the absence of the seed particle these would correspond to factors of the order λ^{-1}, but in its presence some of them will correspond to factors of the order a_s^{-1}. For probe and seed particles with ideal properties, this will cause the force contribution to be up to one order of magnitude higher than the original force. However, as we will see, ideal properties are very different from water-like properties relevant for biomedical applications of acoustophoresis.

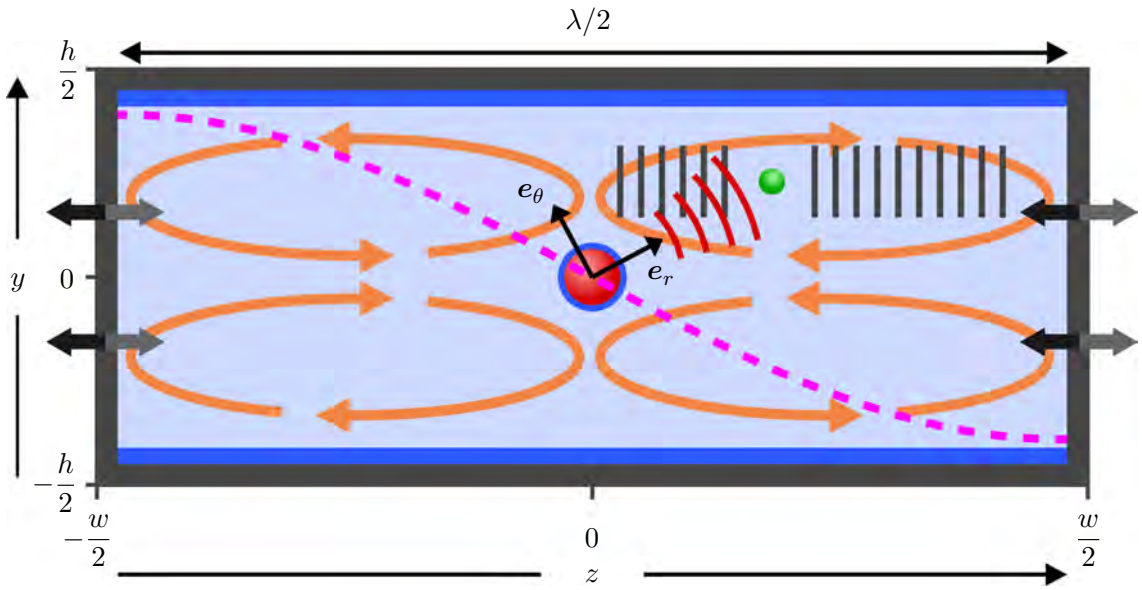

Figure 5.1 Seed particle system. The side walls (dark gray) oscillate in a channel of rectangular cross section filled with water (light blue) to sustain a half-wavelength ($\lambda/2$) standing pressure wave (magenta) with a node in the central channel plane $z = 0$. The velocity field decays to zero within a thin boundary layer (blue) at the channel top and bottom, thus giving rise to circulating flows (orange). A seed particle (red) of radius $a_\mathrm{s} \ll \lambda$ is placed in the channel centre. It generates a boundary layer (blue) of thickness $\delta \ll a_\mathrm{s}$ around its surface and scatters the acoustic fields incident on it. The scattered fields (red) will, like the fields generated externally (dark gray) by the oscillating walls, affect a sub-micron probe particle (green) through the acoustic radiation force. A spherical co-ordinate system is introduced, where the polar angle θ is measured relative to the z axis. The unit vectors $\boldsymbol{e}_r$ and $\boldsymbol{e}_\theta$ indicate that the origin ($r = 0$) is defined as the seed particle centre.

5.1 Calculation of the force contribution

We begin the investigation by going back to Eq. (4.11), which is the expression for the acoustic radiation force. It is valid far from boundary layers for a spherical particle much smaller than the acoustic wavelength and for real incident fields and multipole coefficients,

$$\boldsymbol{F}_\mathrm{rf}^\mathrm{rad} = -\frac{4\pi}{3}\, a^3\, \boldsymbol{\nabla} \left[\frac{1}{2} f_0\, \kappa_0 \left\langle p_\mathrm{in}^2 \right\rangle - \frac{3}{4} f_1\, \rho_0 \left\langle v_\mathrm{in}^2 \right\rangle \right]. \tag{5.1}$$

There are no further restrictions on Eq. (5.1). It is thus valid for any real incident fields but we will, however, still consider externally generated plane wave fields. Without the seed particle, the incident fields are simply the plane wave fields from the standing wave. We shall refer to the force that the probe particle would have experienced if the seed particle had not been there as the standing wave force.

In the presence of a seed particle, however, the probe particle will also be affected by the fields scattered from the seed particle. Thus, the field incident on the probe particle is the sum of the fields from the standing wave, which are induced externally and denoted by a subscript "ext", and the fields scattered from the seed particle, which are denoted by a subscript "sc",

$$\phi_{\mathrm{in}} = \phi_{\mathrm{ext}} + \phi_{\mathrm{sc}}, \qquad p_{\mathrm{in}} = p_{\mathrm{ext}} + p_{\mathrm{sc}}, \qquad \rho_{\mathrm{in}} = \rho_{\mathrm{ext}} + \rho_{\mathrm{sc}}, \qquad \boldsymbol{v}_{\mathrm{in}} = \boldsymbol{v}_{\mathrm{ext}} + \boldsymbol{v}_{\mathrm{sc}}. \tag{5.2}$$

Inserting this into Eq. (5.1) yields terms containing squares of the incident plane wave fields, squares of the fields scattered on the seed particle, and the corresponding mixed terms, e.g. v_{ext}^2, v_{sc}^2 and $2\boldsymbol{v}_{\mathrm{ext}} \cdot \boldsymbol{v}_{\mathrm{sc}}$. The plane wave terms give rise to the standing wave force that we discussed in Section 4.2. Since the mixed terms are proportional to a_{s}^3 and the terms containing squares of the scattered fields are proportional to a_{s}^6, we can neglect the latter terms for a 10-micron seed particle. Thus, we include only the mixed terms and the squares of the plane wave terms in the force expression. We split it into the two terms

$$\boldsymbol{F}^{\mathrm{rad}} = \boldsymbol{F}_{\mathrm{sw}}^{\mathrm{rad}} + \boldsymbol{F}_{\mathrm{s}}^{\mathrm{rad}}, \tag{5.3}$$

where the former is what we call the standing wave force and the latter is the radiation force contribution that originates from the seed particle. We then have

$$\boldsymbol{F}_{\mathrm{sw}}^{\mathrm{rad}} = -\frac{4\pi}{3}\, a_{\mathrm{p}}^3\, \boldsymbol{\nabla} \left[\frac{1}{2} f_{0,\mathrm{p}}\, \kappa_0 \left\langle p_{\mathrm{ext}}^2 \right\rangle - \frac{3}{4} f_{1,\mathrm{p}}\, \rho_0 \left\langle v_{\mathrm{ext}}^2 \right\rangle \right], \tag{5.4a}$$

$$\boldsymbol{F}_{\mathrm{s}}^{\mathrm{rad}} = -\frac{4\pi}{3}\, a_{\mathrm{p}}^3\, \boldsymbol{\nabla} \left[\frac{1}{2} f_{0,\mathrm{p}}\, \kappa_0 \left\langle 2 p_{\mathrm{ext}}\, p_{\mathrm{sc}} \right\rangle - \frac{3}{4} f_{1,\mathrm{p}}\, \rho_0 \left\langle 2 \boldsymbol{v}_{\mathrm{ext}} \cdot \boldsymbol{v}_{\mathrm{sc}} \right\rangle \right], \tag{5.4b}$$

where we also in Eq. (5.4b) use the expression valid for real incident fields. The extra subscripts "p" and "s" on the multipole coefficients f_0 and f_1 denote that it is a probe and seed particle parameter, respectively. The term $\boldsymbol{F}_{\mathrm{s}}^{\mathrm{rad}}$ is not a force exerted directly by the seed particle on the probe particle, but for brevity we shall refer to it as the seed particle force.

Consider a transverse standing pressure wave given by

$$p_{\mathrm{ext}}(z,t) = p_{\mathrm{a}} \sin(kz)\, \sin(\omega t) = p_{\mathrm{a}} \sin[kr\cos\theta] \sin(\omega t). \tag{5.5}$$

As in the first discussion of the radiation force in Section 4.2, the bulk fluid can be considered inviscid, allowing us to introduce a velocity potential given by $\boldsymbol{v} = \boldsymbol{\nabla}\phi$. This field and the other acoustic fields can be determined by use of the first-order relations in Eqs. (2.17) and (2.18),

$$\phi_{\mathrm{ext}}(z,t) = \frac{p_{\mathrm{a}}}{\rho_0 \omega}\, \sin(kz)\, \cos(\omega t) \quad = \frac{p_{\mathrm{a}}}{\rho_0 \omega}\, \sin[kr\cos\theta] \cos(\omega t) \tag{5.6a}$$

$$\rho_{\mathrm{ext}}(z,t) = \frac{\frac{p_{\mathrm{a}}}{c_0^2}}{}\, \sin(kz)\, \sin(\omega t) \quad = \frac{\frac{p_{\mathrm{a}}}{c_0^2}}{}\, \sin[kr\cos\theta] \sin(\omega t) \tag{5.6b}$$

$$v_{\mathrm{ext}}(z,t) = \frac{p_{\mathrm{a}}}{\rho_0 c_0} \cos(kz)\, \cos(\omega t) \boldsymbol{e}_z = \frac{p_{\mathrm{a}}}{\rho_0 c_0} \cos[kr\cos\theta][\cos\theta \boldsymbol{e}_r - \sin\theta \boldsymbol{e}_\theta] \cos(\omega t) \tag{5.6c}$$

The expression for $\boldsymbol{F}_{\mathrm{sw}}^{\mathrm{rad}}$ is given in Eq. (4.13) with the appropriate radius and multipole coefficients,

$$\boldsymbol{F}_{\mathrm{sw}}^{\mathrm{rad}} = 4\pi\,\Phi(\tilde{\kappa},\tilde{\rho})\,k a_{\mathrm{p}}^3 E_{ac}\,\sin(2kz-\pi)\,\boldsymbol{e}_y, \tag{5.7a}$$

$$\Phi(\tilde{\kappa},\tilde{\rho}) = \frac{1}{3}f_{0,\mathrm{p}}(\tilde{\kappa}) + \frac{1}{2}f_{1,\mathrm{p}}(\tilde{\rho}), \qquad E_{\mathrm{ac}} = \frac{p_{\mathrm{a}}^2}{4\rho_0 c_0^2} \tag{5.7b}$$

$$f_0 = 1-\tilde{\kappa}, \quad \tilde{\kappa} = \frac{\kappa'}{\kappa_0}, \qquad f_1 = \frac{2(\tilde{\rho}-1)}{2\tilde{\rho}+1}, \quad \tilde{\rho} = \frac{\rho'}{\rho_0}, \tag{5.7c}$$

Here, we have introduced a phase shift π in the sine because we changed the zero of the z axis in Figure 5.1 compared to previous figures. In order to calculate $\boldsymbol{F}^{\mathrm{rad}}$ we have to determine the fields p_{sc} and v_{sc} scattered on the seed particle. As mentioned in the beginning of this chapter, we consider seed particles with radii of the order 10 µm, like those used in the experiments described in Ref. [1], and typical wavelengths of the order 1 mm $\gg$ 10 µm. The seed particle will thus act as a point scatterer and so we can use Eq. (4.8) for the scattered potential. If the distance to the seed particle is small compared to the acoustic wavelength, we can neglect the time retardation,

$$\phi_{\mathrm{sc}}(r,t) = -f_{0,\mathrm{s}}\frac{a^3}{3\rho_0}\frac{\partial_t\rho_{\mathrm{ext}}}{r} - f_{1,\mathrm{s}}\frac{a^3}{2}\boldsymbol{\nabla}\cdot\left(\frac{\boldsymbol{v}_{\mathrm{ext}}}{r}\right), \tag{5.8}$$

where ρ_{ext} and $\boldsymbol{v}_{\mathrm{ext}}$ are evaluated at the centre of the seed particle ($r=0$) at time t. The seed particle is in the channel centre where the pressure and density waves have a node, whereas the velocity have an antinode, so

$$\partial_t\rho_{\mathrm{ext}} = 0, \qquad \boldsymbol{v}_{\mathrm{ext}} = \frac{p_{\mathrm{a}}}{\rho_0 c_0}\left[\cos\theta\boldsymbol{e}_r - \sin\theta\boldsymbol{e}_\theta\right]\cos(\omega t). \tag{5.9}$$

Thus, from the definition of the velocity potential we have

$$\phi_{\mathrm{sc}}(r,t) = -f_{1,\mathrm{s}}\frac{a_{\mathrm{s}}^3}{2}\frac{p_{\mathrm{a}}}{\rho_0 c_0}\boldsymbol{\nabla}\cdot\left(\frac{\cos\theta\boldsymbol{e}_r - \sin\theta\boldsymbol{e}_\theta}{r}\right)\cos(\omega t) = f_{1,\mathrm{s}}\frac{a_{\mathrm{s}}^3}{2}\frac{p_{\mathrm{a}}}{\rho_0 c_0}\frac{\cos\theta}{r^2}\cos(\omega t). \tag{5.10}$$

A more detailed calculation of the last expression above can be found in Appendix C, Section C.1. Notice that as the seed particle is situated at the pressure node, the monopole term vanishes so that the scattered potential, and thus the seed particle force, do not depend on the seed particle monopole coefficient $f_{0,\mathrm{s}}$. Again, the first-order relations in Eqs. (2.17) and (2.18) allow us to calculate the relevant scattered fields,

$$p_{\mathrm{sc}} = \mathrm{i}\omega\rho_0\,\phi_{\mathrm{sc}} \quad = f_{1,\mathrm{s}}\frac{a_{\mathrm{s}}^3}{2}\frac{p_{\mathrm{a}}\omega}{c_0}\frac{\cos\theta}{r^2}\sin(\omega t), \tag{5.11a}$$

$$\boldsymbol{v}_{\mathrm{sc}} = \boldsymbol{\nabla}\phi_{\mathrm{sc}} \quad = -\frac{p_{\mathrm{a}}}{\rho_0 c_0}f_{1,\mathrm{s}}\frac{a_{\mathrm{s}}^3}{r^3}\left(\cos\theta\,\boldsymbol{e}_r + \frac{1}{2}\sin\theta\,\boldsymbol{e}_\theta\right)\cos(\omega t) \tag{5.11b}$$

Since both the external pressure and velocity fields in Eqs. (5.5) and (5.6c) and the scattered fields in Eqs. (5.11a) and (5.11b) are real, we were in Eq. (5.4b) allowed to use the radiation force expression that is valid for real incident fields.

When Eqs. (5.11a) and (5.11b) are inserted into Eq. (5.4b), the time averages $\left\langle \sin^2(\omega t)\right\rangle$ and $\left\langle \cos(\omega t)^2\right\rangle$ both give a factor $\frac{1}{2}$, and we end up with

$$\boldsymbol{F}_{\mathrm{s}}^{\mathrm{rad}} = -\frac{4\pi}{3}\, a_{\mathrm{p}}^3\, \boldsymbol{\nabla}\Bigg\{ \frac{1}{2} f_{0,\mathrm{p}}\, \kappa_0 \left[p_{\mathrm{a}} \sin[kr\cos\theta]\right] \left[f_{1,\mathrm{s}} \frac{a_{\mathrm{s}}^3}{2} \frac{p_{\mathrm{a}}\omega}{c_0} \frac{\cos\theta}{r^2}\right] \tag{5.12a}$$

$$- \frac{3}{4} f_{1,\mathrm{p}}\, \rho_0 \left[\frac{p_{\mathrm{a}}}{\rho_0 c_0} \cos[kr\cos\theta]\right] \left[-\frac{p_{\mathrm{a}}}{\rho_0 c_0} f_{1,\mathrm{s}} \frac{a_{\mathrm{s}}^3}{r^3} \left(\cos^2\theta - \frac{1}{2}\sin^2\theta\right)\right]\Bigg\} \tag{5.12b}$$

$$= -\frac{4\pi}{3}\, a_{\mathrm{p}}^3 a_{\mathrm{s}}^3 f_{1,\mathrm{s}} E_{\mathrm{ac}}\, \boldsymbol{\nabla} U(r,\theta), \tag{5.12c}$$

where the force is expressed as a gradient of the acoustic potential

$$U(r,\theta) = k f_{0,\mathrm{p}} \frac{\sin[kr\cos\theta]\cos\theta}{r^2} + 3 f_{1,\mathrm{p}} \frac{\cos[kr\cos\theta]\left[\cos^2\theta - \frac{1}{2}\sin^2\theta\right]}{r^3}. \tag{5.13}$$

In spherical co-ordinates we write the gradient as

$$\boldsymbol{\nabla} U(r,\theta) = \boldsymbol{e}_r \partial_r U + \boldsymbol{e}_\theta \frac{1}{r} \partial_\theta U = \boldsymbol{e}_r R(r,\theta) + \boldsymbol{e}_\theta \Theta(r,\theta), \tag{5.14}$$

such that the force is

$$\boldsymbol{F}_{\mathrm{s}}^{\mathrm{rad}}(r,\theta) = -\frac{4\pi}{3}\, a_{\mathrm{p}}^3 a_{\mathrm{s}}^3 f_{1,\mathrm{s}} E_{\mathrm{ac}} \left[\boldsymbol{e}_r R(r,\theta) + \boldsymbol{e}_\theta \Theta(r,\theta)\right]. \tag{5.15}$$

The component functions $R(r,\theta)$ and $\Theta(r,\theta)$ are

$$R(r,\theta) = +k f_{0,\mathrm{p}} \cos\theta \left[\frac{k\cos(kr\cos\theta)\cos\theta}{r^2} - \frac{2\sin(kr\cos\theta)}{r^3}\right] \tag{5.16a}$$

$$- 3 f_{1,\mathrm{p}} (\cos^2\theta - \tfrac{1}{2}\sin^2\theta) \left[\frac{k\sin(kr\cos\theta)\cos\theta}{r^3} + \frac{3\cos(kr\cos\theta)}{r^4}\right] \tag{5.16b}$$

$$\Theta(r,\theta) = -k f_{0,\mathrm{p}} \frac{\sin\theta}{r^3} \left[kr\cos(kr\cos\theta)\cos\theta + \sin(kr\cos\theta)\right] \tag{5.16c}$$

$$+ 3 f_{1,\mathrm{p}} \frac{\sin\theta}{r^4} \left[kr\sin(kr\cos\theta)\left(\cos^2\theta - \tfrac{1}{2}\sin^2\theta\right) - 3\cos(kr\cos\theta)\cos\theta\right]. \tag{5.16d}$$

It is of particular interest to evaluate the contribution $\boldsymbol{F}_{\mathrm{s}}^{\mathrm{rad}}$ for $\theta = \frac{\pi}{2}$, which is at the pressure node where $\boldsymbol{F}_{\mathrm{sw}}^{\mathrm{rad}} = 0$. We see in Eq. (5.16) that at the pressure node $\Theta = 0$, and in R only the last term in the second bracket is non-zero. Hence, the total radiation force experienced by a probe particle at the pressure node is given by a one-term expression,

$$\boldsymbol{F}^{\mathrm{rad}}\left(r, \frac{\pi}{2}\right) = \boldsymbol{F}_{\mathrm{s}}^{\mathrm{rad}}\left(r, \frac{\pi}{2}\right) = -6\pi\, a_{\mathrm{p}}^3 a_{\mathrm{s}}^3 f_{1,\mathrm{p}} f_{1,\mathrm{s}} E_{\mathrm{ac}} \frac{1}{r^4}\, \boldsymbol{e}_r. \tag{5.17}$$

We see from the sign that for positive dipole coefficients $f_{1,\mathrm{p}}$ and $f_{1,\mathrm{s}}$, the direction of the radiation force is inwards. Along the z axis, corresponding to $\theta = 0$, we see in Eqs. (5.15) and (5.16) that the seed particle force is

$$\boldsymbol{F}_{\mathrm{s}}^{\mathrm{rad}}(r,0) = k f_{0,\mathrm{p}} \left[\frac{k\cos(kr)}{r^2} - \frac{2\sin(kr)}{r^3}\right] - 3 f_{1,\mathrm{p}} \left[\frac{k\sin(kr)}{r^3} + \frac{3\cos(kr)}{r^4}\right]. \tag{5.18}$$

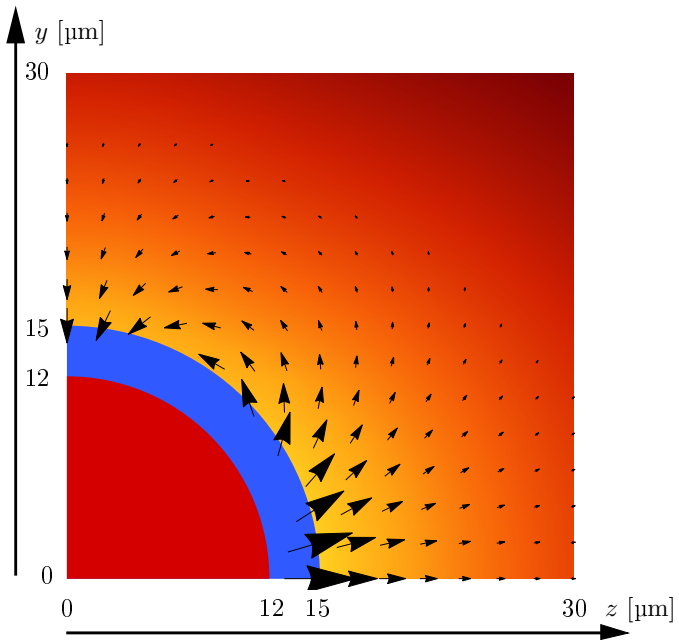

Figure 5.2 Vector density plot of the seed particle force $\boldsymbol{F}_{\mathrm{s}}^{\mathrm{rad}}$ experienced by a probe particle. The arrow size and the colour express the force magnitude on a linear and logarithmic scale, respectively. The scales go from the lowest magnitude of $\simeq 2$ aN (dark red and no arrow) to the largest of $\simeq 17$ fN (yellow and largest arrow) where both particles are of polystyrene and have the radii $a_{\mathrm{s}} = 12$ µm and $a_{\mathrm{p}} = 100$ nm. The red quadrant is the seed particle and the blue area is the boundary layer region where the expression for $\boldsymbol{F}_{\mathrm{s}}^{\mathrm{rad}}$ is invalid.

5.2 Discussion of the results

The general result for the seed particle force $\boldsymbol{F}_{\mathrm{s}}^{\mathrm{rad}}$ on a probe particle is plotted in Figure 5.2 outside the blue boundary layer region for the case where both particles are of polystyrene. We stress that the chosen extent of the boundary layer region is arbitrary. In Eq. (4.15), the boundary layer thickness was determined to be $\delta \approx 0.5$ µm for ultrasound frequencies in water and we have therefore chosen $6\delta \approx 3$ µm as the extent in order to be sure that we plot the force in a valid domain.

As the incident fields oscillate symmetrically around $z = 0$, a plot that includes the negative z-axis is superfluous and, due to the symmetry around the same axis, so too is a plot that includes the negative y-axis. The colour plot and arrow size indicate the force magnitude and the arrows point in the direction of the force. It is evident that the force is largest at the angle $\theta = 0$ (relative to the z axis). Moreover, its direction close to $y = 0$ is opposite to its direction close to $z = 0$. In this case, its direction is outwards at $y = 0$ and inwards at $z = 0$, but which direction is outwards and inwards depends on the sign of the seed particle dipole coefficient $f_{1,\mathrm{s}}$, as evident from Eq. (5.15). As given in Eq. (4.12),

the general expressions for the monopole and dipole coefficients are

$$f_0 = 1 - \tilde{\kappa}, \quad \tilde{\kappa} = \frac{\kappa'}{\kappa_0}, \qquad f_1 = \frac{2(\tilde{\rho}-1)}{2\tilde{\rho}+1}, \quad \tilde{\rho} = \frac{\rho'}{\rho_0}, \tag{5.19}$$

where a prime is used for the particle parameters and a subscript 0 for the parameters of the medium. Polystyrene is denser than water and therefore its dipole coefficient $f_{1,\mathrm{p}}$ in water is positive. A probe particle that is less dense than water would have a negative dipole coefficient and experience an outwards seed particle contribution force along the y axis and inwards along the z axis, contrary to a polystyrene particle.

We recall that the reason for investigating the seed particle force is to see if it adds one or more orders of magnitude to the force experienced by the probe particle, whereby the latter gets larger than the drag force for sub-micron particles.

However, before we turn to that, we compare the seed particle force with the standing wave force. As seen in Eqs. (5.7) and (5.15), both are proportional to the probe particle volume a_{p}^3, which means that the ratio of their magnitude is independent of this quantity. In Figure 5.3 we plot the magnitude of the seed particle force relative to the magnitude of the standing wave force. It is plotted as a function of the radial distance to the seed particle centre at three different angles: $\theta = 0$ (along the z axis), $\theta = \frac{\pi}{5}$, and $\theta = \frac{\pi}{2}$ (along the y axis). We have included the boundary layer region as the dashed parts of the plots but we do not know if they are a good approximation. Figure 5.3(a) is the most relevant plot since it is for polystyrene particles, which, as mentioned earlier, have acoustic

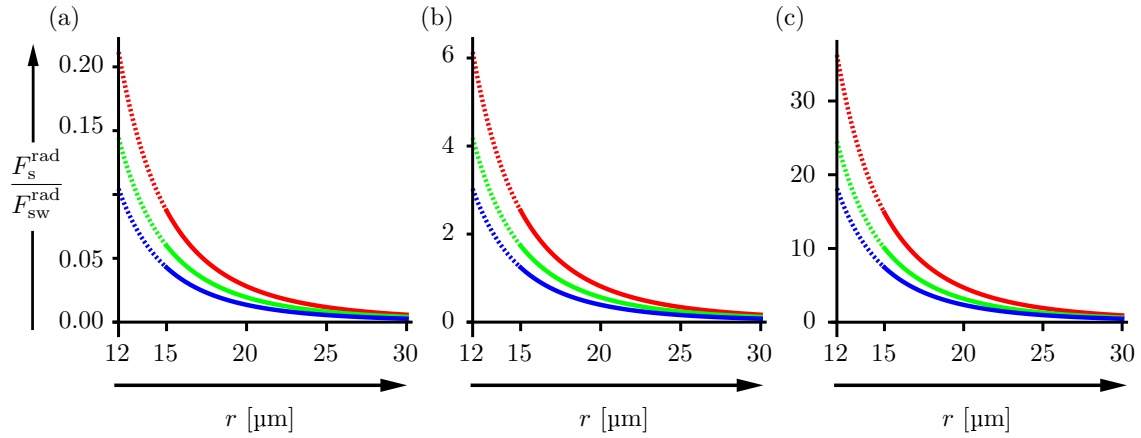

Figure 5.3 The seed particle contribution relative to the standing wave radiation force plotted for $a_{\mathrm{s}} = 12$ µm and $a_{\mathrm{p}} = 100$ nm versus the radial distance to the seed particle centre at the angles $\theta = 0$ (red) corresponding to the z axis, $\theta = \frac{\pi}{5}$ (green) and $\theta = \frac{\pi}{2}$ (blue) corresponding to the y axis. The plots are for water and a wavelength of $\lambda = 2w = 780$ nm. They are dashed in the boundary layer region as the expressions for $F_{\mathrm{s}}^{\mathrm{rad}}$ and $F_{\mathrm{sw}}^{\mathrm{rad}}$ are invalid there. (a) Both the seed particle and the probe particle are of polystyrene. (b) The probe particle is of polystyrene and the seed particle is infinitely dense and hard. (c) Both the seed particle and the probe particle are infinitely dense and hard.

properties similar to those of water and thereby also many organic particles relevant for potential biomedical applications of acoustophoresis. The figure shows that such particles will experience a seed particle force that at its maximum is one order of magnitude lower than the standing wave force. The maximum is just outside the boundary layer region, here 3 µm from the seed particle, corresponding to 15 µm from the channel centre. We see that at approximately 25 µm, the seed particle force has dropped another order of magnitude.

Figure 5.3(b) illustrates the same but for a an infinitely dense seed particle. It shows the increase in orders of magnitude that is achieved if the seed particle is much denser that the suspending medium. For seed particles that are a factor $\frac{3}{2}$ and $\frac{5}{2}$ denser than the suspending medium, use of Eq. (5.19) gives the dipole coefficient $f_{1,\mathrm{s}} = \frac{1}{4}$ and $f_{1,\mathrm{s}} = \frac{1}{2}$, respectively, compared with approximately 0.03 for polystyrene. For an infinitely dense particle, the dipole coefficient is unity so these examples would, as evident from the figure, yield a seed particle force of the same order of magnitude as the standing wave force.

Finally, Figure 5.3(c) shows the case in which both the seed and probe particle are infinitely dense, and the latter also infinitely hard. The fact that the probe particle is infinitely hard corresponding to a vanishing compressibility, $\kappa_{\mathrm{p}} = 0$, results in a probe particle monopole coefficient $f_{0,\mathrm{p}}$ of unity compared with 0.47 for polystyrene. It is thus the high density that increases the seed particle force another order of magnitude from Figure 5.3(b) to Figure 5.3(c). The latter figure indicates that, in principle, one can achieve a seed particle contribution to the radiation force that is an order of magnitude larger than the force would have been, had the seed particle not been present. It is possible because the seed particle introduces a new length scale that enters the problem through the gradient $\boldsymbol{\nabla} U$. For each of the seed particle force component functions R and Θ in Eq. (5.16), we see that the last term is proportional to r^{-4} and that the other terms are proportional to $k^2 r^{-2} \sim \lambda^{-2} r^{-2}$ or $kr^{-3} \sim \lambda^{-1} r^{-3}$. Close to the seed particle $r \approx a_{\mathrm{s}}$. Since we consider $a_{\mathrm{s}} \sim 10$ µm and $\lambda \sim 1$ mm, the r^{-4} term will thus dominate near the seed particle. As it does not include any factor of k or λ it must be a consequence of the introduction of the seed particle length scale.

The above discussion of the seed particle force relative to the standing wave force gives an indication of the ratio of their sum to the drag force since, for particles of the critical radius a_{c} defined in Eq. (4.18), the standing wave force is of the same order of magnitude as the drag force. Nevertheless, we will make the direct comparison in the following, as we our focus is not particles of radius a_{c}. We wish to compare the total radiation force with the drag force for particles smaller than the critical radius, determined to be $a_{\mathrm{c}} \approx 0.5$ µm in Eq. (4.18) under typical experimental conditions. In Figure 5.4, the total radiation force magnitude $F^{\mathrm{rad}} = |\boldsymbol{F}_{\mathrm{sw}}^{\mathrm{rad}} + \boldsymbol{F}_{\mathrm{s}}^{\mathrm{rad}}|$, given by Eqs. (5.7), (5.15) and (5.16), is plotted relative to the magnitude of the drag force given by Eq. (4.16). As in previous examples, we use the streaming velocity $v = 50$ µm/s and the values given in Table A.1.

As the drag force is constant for a given streaming velocity and a given probe particle radius, the radial variations in Figure 5.4 are due to the radiation force. Figure 5.3(a) showed that the radiation force is dominated by the standing wave force for polystyrene particles and this is in agreement with what we see in Figure 5.4(a), which is also for polystyrene. In this figure we see the sinusoidal radial dependence of the standing wave

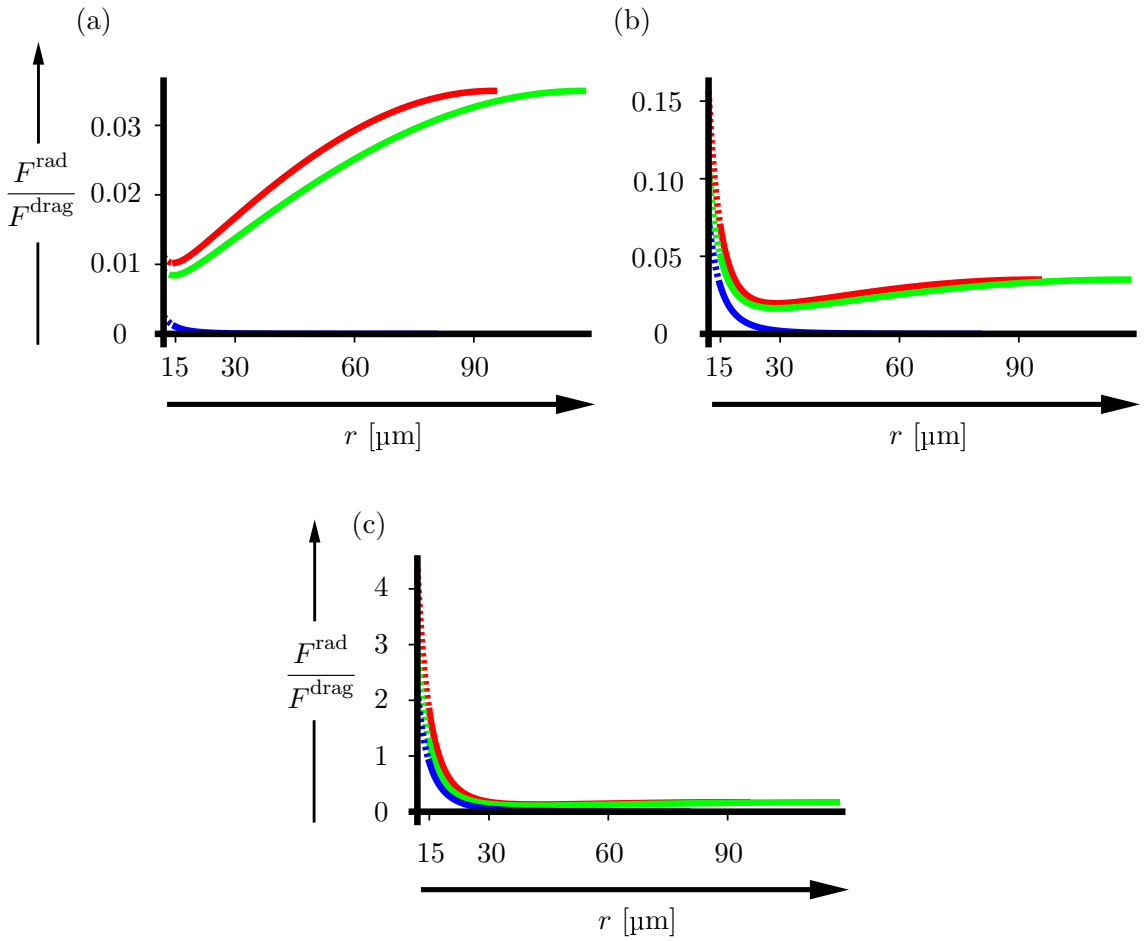

Figure 5.4 Plot of the total radiation force magnitude $F^{\text{rad}} = |\boldsymbol{F}^{\text{rad}}_{\text{sw}} + \boldsymbol{F}^{\text{rad}}_{\text{s}}|$ relative to the drag force magnitude F^{drag} for polystyrene particles of radii $a_{\text{s}} = 12$ µm and $a_{\text{p}} = 100$ nm, the channel width $w = 380$ µm, the channel height $h = 160$ µm, and a streaming velocity $v = 50$ µm/s in water, as a function of the distance r to the seed particle centre at the angles $\theta = 0$ (red), $\theta = \frac{\pi}{5}$ (green) and $\theta = \frac{\pi}{2}$ (blue). The plots are dashed in the boundary layer region 12 µm $\leq r \lessapprox 15$ µm, since we do not know if the plotted expression is valid there. As evident from Figure 5.1, going in the radial direction at angle $\theta = 0$ corresponds to going horizontally along the z axis. In this direction the channel wall is reached at $r = \frac{w}{2}$ and the maximum radiation force at $r = \frac{w}{4}$ (see Figure 4.2). We therefore stop the red plots at $r = \frac{w}{4}$ as the radiation force decreases afterwards. The angle $\theta = \frac{\pi}{2}$ corresponds to the y axis and the blue plots therefore stop when they reach the channel wall at $r = \frac{h}{2}$. For the green plots at $\theta = \frac{\pi}{5}$, the maximum radiation force is reached at $r \approx 117$ µm. (a) Both the seed particle and the probe particle are of polystyrene. (b) The probe particle is of polystyrene and the seed particle is infinitely dense and hard. (c) Both the seed particle and the probe particle are infinitely dense and hard.

force in most of the plot, whereas the inverse proportionality on r^2, r^3 and r^4 from the seed particle force is visually confined to a few micrometres just outside the boundary layer. Most importantly, we see that for particles with water-like properties and radius $a_\mathrm{p} = 100$ nm, the drag force is at least one order of magnitude higher than the total radiation force.

The plots in Figure 5.4(b) are for an infinitely dense and hard seed particle that, as we saw in Figure 5.3(b), has the best properties if we want a high radiation force on the probe particle. In agreement with Figure 5.3(b) we see that the seed particle force (inverse r tendency) is of the same order of magnitude as the standing wave force (sinusoidal dependence). Furthermore, we see that even if a very dense seed particle could be implemented in an acoustophoretic setup, the total radiation force would still be one order of magnitude lower than the drag force.

Finally, in Figure 5.4(c) we see the force ratio for particles with ideal properties: an infinitely dense and hard seed particle and an infinitely dense probe particle. For these imaginary particles, we saw in Figure 5.3 that the introduction of the seed particle length scale increases the radiation force by an order of magnitude. In Figure 5.4(c), we see that this makes it of the same order of magnitude as the drag force for 100 nm particles. It should be stressed that we have used a typical maximum (50 µm /s) for the drag force which means that we underestimate the ratio in some parts of the rectangular channel where the streaming is not at its maximum (see Figure 4.3).

Summing up the effect on the radiation force of placing a seed particle in the channel centre, we can say that under circumstances realistic for biomedical applications (particles with water-like acoustic properties), the seed particle force is at least an order of magnitude less than the standing wave force for 100 nm probe particles. Moreover, the total radiation force is at least one order of magnitude lower than the drag force, which means that the latter will still dominate the particle trajectories.

If a seed particle material could be found, that is inert with respect to the probe particles and much denser than water, it could yield a seed particle force that, within 10 µm of the seed particle surface, is almost of the same order of magnitude as the standing wave force. For 100 nm particles, that is not enough to make the total radiation force as big as the drag force. Even if one could find an application for the case of very dense seed and probe particles, which would yield a total radiation force of the same order of magnitude as the drag force for 100 nm particles, Figure 5.2 shows that this contribution would only counteract the streaming close to the y axis. Close to the z axis, the contribution would be outwards, thus making it impossible to focus particles in the channel centre.

Due to the negligible contribution to the acoustic radiation force under circumstances realistic for biomedical applications, we shall not treat the seed particle force further in this thesis. One could increase the seed particle radius a_s and see how this affects the results but, for the systems considered here, there is a risk that it occupies most of the channel centre, thus making it impossible for the probe particles to move there. We shall not continue further with those considerations but instead turn our attention to the streaming that the seed particle generates.

Chapter 6

Acoustic streaming generated by a rigid sphere

The conclusion from the previous chapter is that for sub-micrometre-sized organic (water-like) particles in milimetre-sized channels with transverse standing acoustic waves, the channel streaming dominates the acoustic radiation force. It could be, however, that the streaming generated by the velocity gradients at the seed particle surface is stronger than the channel streaming. In this and the next chapter we therefore investigate the streaming due to the seed particle.

The acoustic streaming from a sphere located in the pressure node of a standing acoustic wave has been calculated by Riley [26] in the incompressible flow approximation for an unbounded fluid. In Ref. [27] Sadhal goes through Riley's work in what is supposed to be a tutorial article on the streaming from a sphere. However, Sadhal does not present any calculations or derivations but only the employed method and the results. The problem is non-trivial but, nevertheless, detailed calculations and derivations have not been found in the literature. In this thesis we therefore include all the detailed calculations originally left out by both Riley and Sadhal, as a considerable amount of time in the work done preparing the thesis has been devoted to derive Riley's result. All the calculations are available but some are included only in appendices.

The system is sketched in Figure 6.1. It is different from the system sketched in Figure 5.1 as we now consider an unbounded fluid. Furthermore, we emphasise the seed particle streaming (red) and not the scattered fields as previously. At this point, we do not know what the streaming pattern is, hence the question marks. The fluid is still supporting a standing pressure wave of wavelength λ along the z axis and the seed particle is located at a pressure node. We think of the pressure wave as a field applied by an external influence so far away that we can still consider the fluid unbounded. We shall drop the term seed particle for now and refer to it as a sphere, due to the general character of the problem. When we have solved the general problem, we resume the discussion of the effects of the seed particle, applying the results.

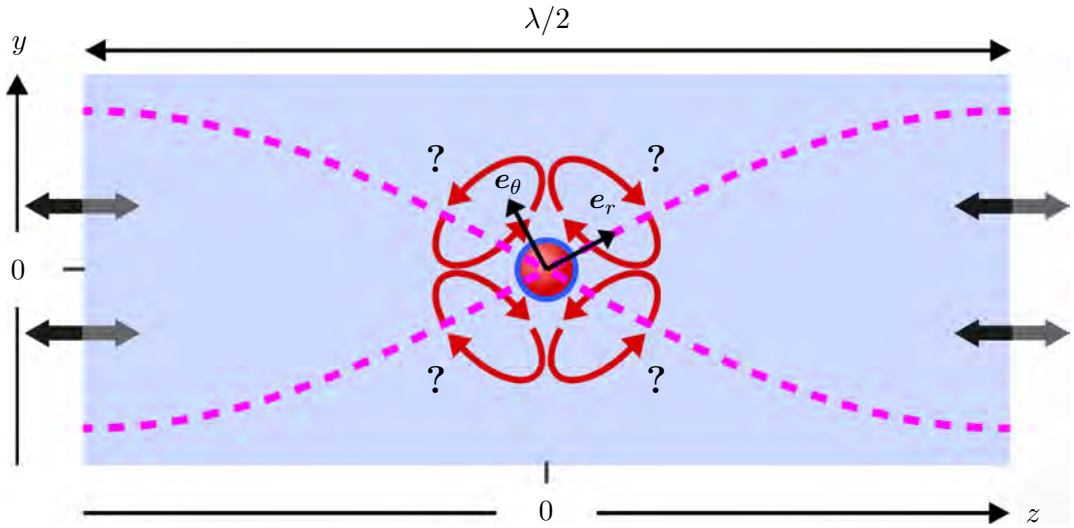

Figure 6.1 Unbounded fluid (light blue) supporting a standing pressure wave (magenta) of wavelength λ. The fluid contains a rigid, spherical particle (red), on the surface of which the velocity field has to decay to zero. The resulting velocity gradients create a boundary layer (blue) and drive a streaming pattern (red arrows) to be determined. The unit vectors $\boldsymbol{e}_r$ and $\boldsymbol{e}_\theta$ indicate that the origin ($r = 0$) of the spherical co-ordinate system is the centre of the seed particle.

6.1 Characteristic numbers

Before we begin the mathematical treatment, it is instructive to discuss the characteristic scales of the problem and relevant dimensionless numbers that we shall encounter. As discussed in Section 4.3 the velocity field amplitude decays to zero at the sphere surface within a boundary layer of thickness

$$\delta = \sqrt{\frac{2\nu}{\omega}} \approx 0.5\ \mu\text{m}. \tag{6.1}$$

This is the shortest length scale of the problem which has two more: the sphere radius a and the acoustic wavelength λ. Moreover, the problem also involves three velocity scales: the steady streaming velocity $\langle v_2 \rangle$ due to the sphere, the amplitude of the oscillating velocity field v_a, and the isentropic speed of sound c_0. Finally, the problem has only one time scale given by the angular frequency ω of the oscillating fields.

It turns out that the qualitative structure of the sphere streaming depends on the ratio of its radius a to the boundary layer thickness δ, inviting a definition of a dimensionless number. We define

$$M^2 \equiv \frac{\mathrm{i}\omega a^2}{\nu}, \tag{6.2a}$$

$$|M^2| = \frac{\omega a^2}{\nu} = \frac{2\omega a^2}{2\nu} = 2\frac{a^2}{\delta^2}, \tag{6.2b}$$

and refer to M as the boundary number. As evident from Eq. (6.2b), the square of its magnitude is two times the ratio of the sphere's radius to the boundary layer thickness. We shall assume that it is much larger than unity, $|M| \gg 1$, which is the limit where the boundary layer is thin compared to the size of the sphere.

Another dimensionless number that we will encounter is

$$\varepsilon = \frac{v_\mathrm{a}}{\omega a} \approx \frac{\Delta a}{a}. \tag{6.3}$$

We shall refer to ε as the amplitude number since it depends on the velocity amplitude v_a of the oscillating velocity field, which is the quantity that can be increased or decreased experimentally. If we divide the velocity amplitude v_a by the angular frequency ω, we get the spatial oscillation amplitude of the velocity field, i.e. the displacement of the fluid far from the sphere. This is a good estimate of the displacement Δa of the sphere when it moves back and forth during the oscillations. In Eq. (6.3) we use this estimate to interpret the amplitude number as the ratio of the sphere displacement relative to its size. We shall assume that $\varepsilon \ll 1$ such that the sphere displacement is small compared to its size, as we intent to use the amplitude number as a small perturbation parameter.

As $r \to \infty$, the first-order velocity field must approach the velocity field that is applied far from the sphere by the external influence. This leads to a boundary condition that is simplified if we assume that the sphere is much smaller than the acoustic wavelength, i.e. that $a \ll \lambda$. In this limit, the velocity field far from the sphere (far in this case being several radii) is a constant since the sphere is sufficiently small that the variation is negligible. Summing up the length scales, we work in the limit

$$\delta \ll a \ll \lambda. \tag{6.4}$$

The externally applied oscillating velocity field is regarded as a first-order perturbation of an otherwise quiescent fluid. Thus, its amplitude must be much lower than the speed of sound in the fluid, i.e. $v_\mathrm{a} \ll c_0$. The streaming is the steady part of the second-order velocity field and should therefore be smaller than the first-order velocity amplitude, i.e. $\langle v_2 \rangle \ll v_\mathrm{a}$. This and the limit $v_\mathrm{a} \ll c_0$ ensure that both the streaming flow and the first-order flow are incompressible, since density fluctuations travel at the much higher speed of sound, c_0. This allows us to use the incompressible flow approximation of the governing equation. Summing up the velocity relations, we work in the limit

$$\langle v_2 \rangle \ll v_\mathrm{a} \ll c_0. \tag{6.5}$$

Finally, we have also introduced the two dimensionless numbers

$$|M| = \sqrt{2}\,\frac{a}{\delta} \gg 1, \tag{6.6a}$$

$$\varepsilon \approx \frac{\Delta a}{a} \ll 1, \tag{6.6b}$$

where the boundary number limit follows from Eq. (6.4), and the amplitude number limit is an extra condition interpreted as a small displacement of the sphere relative to its size.

6.2 Reformulation of the Navier-Stokes equation

Having discussed the different scales of the problem, we are now ready to begin the mathematical treatment. We want to derive the streaming velocity for a rigid, spherical particle in an unbounded fluid supporting a standing acoustic wave in the incompressible flow approximation. As we saw in Eqs. (5.5) and (5.6) for the external standing wave fields, the velocity field has an antinode where the pressure field has a node. Thus, if we let the polar axis coincide with the axis of oscillation, as in Figure 6.1, we can express the first-order velocity field far from the particle as

$$\boldsymbol{v}_1 = \boldsymbol{v}(z,t) = v_\mathrm{a}\cos(kz)\mathrm{e}^{\mathrm{i}\omega t}\boldsymbol{e}_z, \qquad r \gg a, \tag{6.7}$$

where v_a is the amplitude, and the physical fields are obtained by taking the real part. As all the fields involved have a time dependence that can be written on the complex form $\mathrm{e}^{\mathrm{i}\omega t}$, we shall henceforth omit writing it explicitly. We do, however, remember that we assume harmonic time dependence of the externally applied fields, which means that a time derivative gives a factor $\mathrm{i}\omega$. In the incompressible flow approximation the velocity field is divergenceless, $\boldsymbol{\nabla}\cdot v = 0$, and the Navier-Stokes equation, Eq. (2.6), reduces to

$$\rho\left[\partial_t\boldsymbol{v} + (\boldsymbol{v}\cdot\boldsymbol{\nabla})\boldsymbol{v}\right] = -\boldsymbol{\nabla}p + \eta\nabla^2\boldsymbol{v}. \tag{6.8}$$

Using the identity $(\boldsymbol{v}\cdot\boldsymbol{\nabla})\boldsymbol{v} = \frac{1}{2}\boldsymbol{\nabla}(\boldsymbol{v}\cdot\boldsymbol{v}) - \boldsymbol{v}\times(\boldsymbol{\nabla}\times\boldsymbol{v})$ this can be rewritten as

$$\rho\left[\partial_t\boldsymbol{v} - \boldsymbol{v}\times(\boldsymbol{\nabla}\times\boldsymbol{v})\right] = -\boldsymbol{\nabla}\left(p + \tfrac{1}{2}\boldsymbol{v}\cdot\boldsymbol{v}\right) + \eta\nabla^2\boldsymbol{v}. \tag{6.9}$$

Taking the curl eliminates the gradient terms and yields

$$\partial_t\boldsymbol{\zeta} - \boldsymbol{\nabla}\times(\boldsymbol{v}\times\boldsymbol{\zeta}) = \nu\nabla^2\boldsymbol{\zeta}, \tag{6.10}$$

where we have introduced the so-called vorticity $\boldsymbol{\zeta} = \boldsymbol{\nabla}\times\boldsymbol{v}$, and where $\nu = \eta/\rho$ is the kinematic viscosity. To ease the treatment, we non-dimensionalise the problem using the sphere radius a as a length scale, the angular frequency ω as a time scale, and the amplitude of the oscillating field as a velocity scale. Denoting the non-dimensionalised quantities by a prime, we have

$$r' = \frac{r}{a}, \qquad t' = \omega t, \qquad \boldsymbol{v}' = \frac{\boldsymbol{v}}{v_\mathrm{a}}, \qquad \boldsymbol{\nabla} = a\boldsymbol{\nabla}', \qquad \boldsymbol{\zeta}' = \frac{a}{v_\mathrm{a}}\boldsymbol{\zeta}. \tag{6.11}$$

Insertion of Eq. (6.11) into Eq. (6.10) and multiplication by $\frac{a}{\omega v_\mathrm{a}}$ yield

$$\partial_t\boldsymbol{\zeta}' - \boldsymbol{\nabla}\times(\boldsymbol{v}'\times\boldsymbol{\zeta}') = \frac{1}{|M|^2}\nabla'^2\boldsymbol{\zeta}', \qquad \varepsilon = \frac{v_\mathrm{a}}{\omega a}, \qquad |M| = \sqrt{2}\,\frac{a}{\delta}. \tag{6.12}$$

This is a rewritten, non-dimensionalised equation of motion for incompressible flows. We stress that in the non-dimensionalised co-ordinates, a time derivative corresponds to a factor of the imaginary unit i for fields with a harmonic time dependence, since $\exp(\mathrm{i}\omega t) = \exp(\mathrm{i}t')$. For convenience, we shall omit the primes in most of the following treatment, and only write them explicitly when we also discuss the dimensionalised fields.

In the following section we exploit the axisymmetry and incompressibility to reformulate Eq. (6.12) as a scalar equation. This requires many tedious calculations, which is why we describe the method and present only the result. The full calculation is included in Appendix D, Section D.1.

6.3 The scalar equation of motion

The symmetry around the z axis dictates that the physical fields can neither have an azimuthal dependence nor an azimuthal component, thus reducing the problem to a 2D problem. Since the velocity field is divergenceless, we can write the two components in terms of the curl of a scalar function $\psi(r,\theta)$, which we shall refer to as the streaming function,

$$\boldsymbol{v} = \boldsymbol{\nabla} \times \boldsymbol{\xi} = \boldsymbol{\nabla} \times \left[\frac{\psi(r,\theta)}{r\sin\theta}\, \boldsymbol{e}_\phi \right]. \tag{6.13}$$

Taking the curl of a vector that has only a azimuthal component ensures that the velocity field has only a radial and a polar component. The division by $r\sin\theta$ turns out to be convenient. We now wish to calculate the vorticity $\boldsymbol{\zeta}$, its Laplacian $\nabla^2\boldsymbol{\zeta}$ and the term $\boldsymbol{\nabla} \times (\boldsymbol{v} \times \boldsymbol{\zeta})$ contained in Eq. (6.12) in terms of the streaming function. This is a very tedious process that ends with a scalar equation, which we shall refer to as the streaming equation,

$$\partial_t(D^2\psi) + \varepsilon \left[\frac{1}{r^2} \frac{\partial(\psi, D^2\psi)}{\partial(r,\mu)} + \frac{2}{r^2}(D^2\psi)(L\psi) \right] = \frac{1}{|M|^2} D^4\psi. \tag{6.14}$$

The operators are

$$D^2 = \partial_r^2 + \frac{1-\mu^2}{r^2}\,\partial_\mu^2, \qquad D^4 = D^2D^2, \qquad L = \frac{\mu}{1-\mu^2}\,\partial_r + \frac{1}{r}\,\partial_\mu, \tag{6.15}$$

and

$$\frac{\partial(P,Q)}{\partial(x,y)} = (\partial_x P)(\partial_y Q) - (\partial_y P)(\partial_x Q). \tag{6.16}$$

When deriving this equation in Section D.1 in Appendix D, we also determine the relation between the streaming function and the velocity components. These are found in Eq. (D.10) by calculation of the cross product in Eq. (6.13) and the result is

$$\boldsymbol{v} = -\boldsymbol{e}_r \frac{1}{r^2}\,\partial_\mu\psi - \boldsymbol{e}_\theta \frac{(1-\mu^2)^{-\frac{1}{2}}}{r}\,\partial_r\psi. \tag{6.17}$$

These relations are necessary when we in the next section convert the boundary conditions given in terms of the velocity field to conditions in terms of the streaming function.

6.4 Boundary conditions

One boundary condition for Eq. (6.14) is given by the first-order velocity field far from the sphere, which must be equal to the applied oscillating field,

$$\boldsymbol{v}_1(z,t) = v_\mathrm{a}\cos(kz)\boldsymbol{e}_z = v_\mathrm{a}\left(1 - \frac{1}{2}(kz)^2 + \frac{1}{24}(kz)^4 - ...\right)\boldsymbol{e}_z, \qquad r \gg a. \tag{6.18}$$

In the last expression we have written the series expansion of the cosine function to illustrate that for $kz \ll 1$ or equivalently $z \ll \lambda$, the first term is a good approximation.

Physically, this means that the sphere is situated at the velocity antinode and is sufficiently small compared to the acoustic wavelength that the field does not vary considerably over the extent of the sphere and its immediate surroundings. The condition states that the first-order velocity field $\boldsymbol{v}_1$ must approach the external field far from the sphere. As there is no external second-order field, the second-order velocity fields must decay to zero far from the sphere. Finally, the velocity field has to decay from its bulk amplitude to zero at the surface of the sphere due to its rigidity. We shall refer to this requirement as a no-slip boundary condition. As it is a consequence of a particle property it applies to all orders. Hence, the boundary conditions are

$$v_{1r} = 0 \quad \text{and} \quad v_{1\theta} = 0 \qquad \text{at} \quad r = 1, \tag{6.19a}$$
$$v_{2r} = 0 \quad \text{and} \quad v_{2\theta} = 0 \qquad \text{at} \quad r = 1, \tag{6.19b}$$
$$\boldsymbol{v}_1 \to v_\mathrm{a} \left(\cos\theta\, \boldsymbol{e}_r - \sin\theta\, \boldsymbol{e}_\theta\right) \quad \text{as} \quad r \to \infty, \tag{6.19c}$$
$$\boldsymbol{v}_2 \to 0 \qquad \text{as} \quad r \to \infty, \tag{6.19d}$$

where the unit vector $\boldsymbol{e}_z$ is expressed in spherical co-ordinates and subscripts r and θ denote the vector components in spherical co-ordinates. Remember that these conditions are for the non-dimensionalised variables, so $r = 1$ corresponds to the surface of the sphere.

We work with the streaming function and consequently the boundary conditions have to be formulated in terms of that. The relations between $\boldsymbol{v}$ and ψ are given in Eq. (6.17) and lead to the conditions

$$v_{ir} = -\frac{1}{r^2}\partial_\mu \psi_i = 0 \qquad \text{at} \quad r = 1 \quad \text{for} \quad i = 1, 2 \tag{6.20a}$$
$$v_{i\theta} = -\frac{\left(1-\mu^2\right)^{-\frac{1}{2}}}{r}\,\partial_r \psi_i = 0 \quad \text{at} \quad r = 1 \quad \text{for} \quad i = 1, 2 \tag{6.20b}$$
$$\psi_1 \to \frac{1}{2} v_\mathrm{a} r^2 \left(1-\mu^2\right) \qquad \text{as} \quad r \to \infty, \tag{6.20c}$$
$$\psi_2 \lesssim r \qquad \text{as} \quad r \to \infty, \tag{6.20d}$$

where the symbol $\lesssim$ denotes that the order of magnitude is equal to or less than the subsequent expression. The equivalence of Eqs. (6.19c) and (6.20c) and of Eqs. (6.19c) and (6.20d) can be recognised by computation of the components in Eqs. (6.20a) and (6.20b). Inspection of Eqs. (6.20a) and (6.20b) reveals that the no-slip condition is fulfilled for $\psi_i = \partial_r \psi_i = 0$ on the surface of the sphere. This allows a simplification of the boundary conditions,

$$\psi_1 = \quad \psi_2 = 0 \qquad \text{at} \quad r = 1, \tag{6.21a}$$
$$\partial_r \psi_1 = \partial_r \psi_2 = 0 \qquad \text{at} \quad r = 1, \tag{6.21b}$$
$$\psi_1 \to \tfrac{1}{2} v_\mathrm{a} r^2 \left(1-\mu^2\right) \qquad \text{as} \quad r \to \infty, \tag{6.21c}$$
$$\psi_2 \lesssim r \qquad \text{as} \quad r \to \infty. \tag{6.21d}$$

We now return to a discussion of the equation itself.

6.5 Singular perturbation theory and the method of matched asymptotic expansions

Due to the nonlinear terms in the square bracket, it is difficult to solve the equation of motion, even after transforming it to the scalar equation

$$\partial_t(D^2\psi) + \varepsilon\left[\frac{1}{r^2}\frac{\partial(\psi, D^2\psi)}{\partial(r,\mu)} + \frac{2}{r^2}(D^2\psi)(L\psi)\right] = \frac{1}{|M|^2}D^4\psi. \tag{6.22}$$

The usual way to overcome this is to employ perturbation theory, but it turns out that a straightforward perturbation expansion,

$$\psi = \psi_1 + \varepsilon\psi_2 + \varepsilon^2\psi_3 + ..., \tag{6.23}$$

in the parameter ε, which contains the oscillation amplitude, works only to first order. The reason for this is the presence of three disparate length scales in the problem: the boundary layer thickness δ, the particle radius $a \gg \delta$ and the acoustic wavelength $\lambda \gg a$. Inside the boundary layer, the length scale is given by its thickness δ, whereas the acoustic wavelength λ is the appropriate length scale outside. Consequently, the acoustic fields vary over distances of the order δ and λ within and outside the boundary layer, respectively. This means that for an order of magnitude calculation inside the boundary layer, we can approximate the radial derivatives by a factor δ^{-1}. Likewise we can replace radial derivatives outside by the factor λ^{-1}. As we have non-dimensionalised the length scale by dividing by the sphere radius a, this parameter enters the non-dimensionalised derivatives in the numerator. Thus, we can make an order of magnitude comparison of the different terms by substituting either $a\delta^{-1}$ or $a\lambda^{-1}$ for each radial derivative, and remember that $|M|^2 \sim a^2\delta^{-2}$. The radial derivatives are of the order unity and can therefore be ignored. For the orders of magnitude inside ($r \sim \delta$) and outside ($r \gtrapprox 5\delta$), we obtain

$$\partial_t(D^2\psi) \;+\; \varepsilon\left[-\frac{1}{r^2}\frac{\partial(\psi, D^2\psi)}{\partial(r,\mu)} + \frac{2}{r^2}(D^2\psi)(L\psi)\right] \;=\; \frac{1}{|M|^2}D^4\psi, \tag{6.24a}$$

$$r \sim \delta: \quad \sim \frac{a^2}{\delta^2} \approx 10^3 \qquad \sim \varepsilon\frac{a^3}{\delta^3} \approx 10^2 \qquad \sim \frac{a^2}{\delta^2} \approx 10^3, \tag{6.24b}$$

$$r \gtrapprox 5\delta: \quad \sim \frac{a^2}{\lambda^2} \approx 10^{-4} \qquad \lesssim \varepsilon\frac{a^3}{\lambda^3} \approx 10^{-8} \qquad \sim \frac{a^2\delta^2}{\lambda^4} \approx 10^{-11}. \tag{6.24c}$$

The order of magnitude of each term within and outside the boundary layer is determined using the values $v_a \approx 0.5$ m/s and $\lambda = 760$ µm (reported in Ref. [24]) for experiments resembling the usual rectangular channel, and $a = 12$ µm, which was the seed particle radius used in the experiments reported in Ref. [1]. The angular frequency ω is calculated using the isentropic speed of sound in Table A.1. Notice that we do not include the time derivative in the order of magnitude calculation, since we consider only harmonic time dependence, and in the non-dimensionalised co-ordinates this would merely give a factor of the imaginary unit i. Furthermore, notice the use of $\lesssim$ in Eq. (6.24c). It means that

the order of magnitude is less than or equal to the subsequent expression, and we use it because the factors r^{-2} decrease as r increases.

We see clearly in Eq. (6.24c) that the term on the right hand side is negligible outside the boundary layer. Moreover, to first order (zeroth order in ε) we can also neglect the square bracket so Eq. (6.24a) reduces to $\partial_t(D^2\psi_1) = 0$. The solution to this equation will, however, fulfil only the boundary condition in Eq. (6.21c). It breaks down near the boundary layer, revealing that the problem is singular in the term on the right hand side. By singular, we mean that the problem and its solutions change qualitatively if the term is neglected even though it is negligible in most of the problem domain. The reason is that the very small factor $|M|^{-2}$ multiplies the highest derivative, which is huge within the boundary layer, where the velocity, the streaming function and its radial derivative transition from their bulk amplitude to zero over a very short distance. Thus, as evident from Eq. (6.24b), in this small part of the problem domain the right hand side term is of the same order of magnitude as $\partial_t(D^2\psi_1)$, and should therefore not be neglected.

We could be tempted to solve the first order problem without neglecting the singular term in any region. This is done in Section D.2 in Appendix D, but has the downside that the second-order solution can not be determined by going to second order with the found solution. As we are interested in acoustic streaming, a second-order effect, we have to solve the problem using the method of matched asymptotic expansions. It dates back to the seminal work of Prandtl [28] and is described thoroughly by Van Dyke in Ref. [29]. The idea is to separate the problem into an inner and an outer part that satisfy the boundary conditions inside and outside the boundary layer, respectively. The co-ordinates and dependent variables of the inner part are stretched in order be formulated using the length scale δ that is appropriate within the boundary layer. These two solutions are then matched asymptotically. By this we mean that as the relevant inner co-ordinates go to infinity, corresponding to just outside the boundary layer, it should match the outer solution for the outer co-ordinates approaching the boundary layer.

Since we want to introduce the boundary layer thickness in the non-dimensionalisation of the problem, we introduce the stretched radial co-ordinate η' and the inner streaming function Ψ',

$$\eta' = \frac{|M|}{\sqrt{2}}(r' - 1) = \frac{a}{\delta}(r' - 1) = \frac{a}{\delta}\left(\frac{r}{a} - 1\right) = \frac{(r - a)}{\delta}, \tag{6.25a}$$

$$\Psi' = \frac{|M|}{\sqrt{2}}\psi' \qquad = \frac{a}{\delta}\psi' \qquad = \frac{a}{\delta}\frac{\psi}{v_\mathrm{a}a^2} \qquad = \frac{\psi}{v_\mathrm{a}a\delta}. \tag{6.25b}$$

Here, we have briefly reintroduced the prime notation for the non-dimensionalised radial co-ordinate and the streaming function. This shows that the stretched radial non-dimensionalised co-ordinate η' is the radial distance to the surface of the sphere in units of the boundary layer thickness. It can be considered a normalisation such that, in the boundary layer region, the radial derivatives are of the order unity like the polar ones. For the streaming function, it shows that the appropriate scale is $v_\mathrm{a}a\delta$ and not $v_\mathrm{a}a^2$.

If we once again omit the prime notation, we can transform Eq. (6.24a) into the

appropriate inner equation of motion,

$$\partial_t\big(\partial_\eta^2\psi\big) + \varepsilon\left[\frac{\partial\big(\Psi,\partial_\eta^2\Psi\big)}{\partial(\eta,\mu)} + \frac{2\mu}{1-\mu^2}\big(\partial_\eta\Psi\big)\big(\partial_\eta^2\Psi\big)\right] = \frac{1}{2}\partial_\eta^4\Psi, \tag{6.26}$$

where the details are provided in Appendix D, Section D.3. Inspection of Eq. (6.25a) shows that the no-slip boundary conditions in the inner co-ordinates take the form

$$\Psi_1 = \quad \Psi_2 = 0 \quad \text{at} \quad \eta = 0, \tag{6.27a}$$
$$\partial_\eta\Psi_1 = \partial_\eta\Psi_2 = 0 \quad \text{at} \quad \eta = 0. \tag{6.27b}$$

We recall that the reason for going to second order is that we wish to investigate the steady streaming pattern, a time-averaged effect. Therefore, we take the time average of the second-order conditions in Eq. (6.27). As the time average of zero is zero, we obtain

$$\Psi_1 = \quad \big\langle\Psi_2\big\rangle = 0 \quad \text{at} \quad \eta = 0, \tag{6.28a}$$
$$\partial_\eta\Psi_1 = \partial_\eta\big\langle\Psi_2\big\rangle = 0 \quad \text{at} \quad \eta = 0. \tag{6.28b}$$

The conditions in Eqs. (6.21c) and (6.21d) remain unchanged as they apply outside the boundary layer.

6.6 Problem summary

Before we begin solving the problem, we provide a short summary of the preceding sections. The problem we seek to solve is a rigid sphere situated at a pressure node of an acoustic standing plane wave supported by an unbounded fluid. We want to solve it the incompressible flow approximation and in the limit $\varepsilon \ll 1$, where the amplitude of the acoustic wave is sufficiently small that the oscillation amplitude of the sphere is much smaller than its radius. Furthermore, we require that $|M| \gg 1$, such that the acoustic boundary layer is much thinner than the radius of the sphere, and finally, we require that $\lambda \gg a$ meaning that the acoustic wavelength is much larger than the extent of the sphere, so that its amplitude is approximately constant the sphere's vicinity.

We started out discussing the above-mentioned characteristic length scales and numbers in anticipation of the importance of those when the problem should be solved. We then rewrote the vector equation of motion in the form of the Navier-Stokes equation to a non-dimensionalised scalar equation in the streaming function, exploiting the axisymmetry and the incompressibility. Finally, we discussed the singular term in the scalar equation and separated the problem into an inner problem,

$$\partial_t(\partial_\eta^2\Psi) + \varepsilon\left[\frac{\partial\big(\Psi,\partial_\eta^2\Psi\big)}{\partial(\eta,\mu)} + \frac{2\mu}{1-\mu^2}\big(\partial_\eta^2\Psi\big)\big(\partial_\eta\Psi\big)\right] = \frac{1}{2}\partial_\eta^4\Psi, \tag{6.29a}$$
$$\Psi_1 = \quad \Psi_2 = 0 \quad \text{at} \quad \eta = 0, \tag{6.29b}$$
$$\partial_\eta\Psi_1 = \partial_\eta\Psi_2 = 0 \quad \text{at} \quad \eta = 0. \tag{6.29c}$$

and an outer problem

$$\partial_t(D^2\psi) + \varepsilon\left[-\frac{1}{r^2}\frac{\partial(\psi, D^2\psi)}{\partial(r,\mu)} + \frac{2}{r^2}(D^2\psi)(L\psi)\right] = \frac{1}{|M|^2}D^4\psi, \tag{6.30a}$$

$$\psi_1 \to \tfrac{1}{2}v_{\mathrm{a}}r^2\big(1-\mu^2\big) \qquad \text{as} \quad r\to\infty, \tag{6.30b}$$

$$\psi_2 \lesssim r \qquad\qquad\qquad\quad \text{as} \quad r\to\infty. \tag{6.30c}$$

6.7 Outer first-order solution

We shall now solve the problem and find an expression for the sphere streaming. We begin by solving the outer first-order equation where the first step is to make a perturbation expansion in the oscillation parameter,

$$\psi = \psi_1 + \varepsilon\psi_2 + \varepsilon^2\psi_3 + ... \tag{6.31}$$

Insertion of Eq. (6.31) into Eq. (6.14) yields to first order

$$\partial_t(D^2\psi_1) = \frac{1}{|M|^2}D^4\psi_1, \tag{6.32}$$

As discussed, it is possible to solve this equation and find the exact first-order solution for an arbitrary value of M. However, it is more instructive to find the inner and outer solutions directly, as they are needed to solve the second-order equation for $|M| \gg 1$. The exact solution to first order is derived in Section D.2 in Appendix D, where it is also shown that for $|M| \gg 1$, it tends towards the inner and outer solution close to and far from the boundary layer, respectively. Here, we derive the outer solution to first order, meaning that we neglect the right hand side term. As we consider acoustic fields that have a harmonic time dependence, the time derivative gives a factor i (in the non-dimensionalised co-ordinates), and the equation reduces to

$$D^2\psi_1 = \partial_r^2\psi_1 + \frac{1-\mu^2}{r^2}\partial_\mu^2\psi_1 = 0. \tag{6.33}$$

The asymptotic boundary condition in Eq. (6.30b) calls for a separation of variables,

$$\psi_1(r,\mu) = R_1(r)\big(1-\mu^2\big). \tag{6.34}$$

Insertion of Eq. (6.34) into Eq. (6.33) yields

$$R_1''(r) = \frac{2}{r^2}R_1(r), \tag{6.35}$$

which has the solution $R_1(r) = c_{\mathrm{I}}r^2 + c_{\mathrm{II}}r^{-1}$. The asymptotic condition in Eq. (6.30b) leads to $c_{\mathrm{I}} = \frac{1}{2}$, but as expected the solution can not fulfil both the inner conditions $\psi = \partial_r\psi = 0$ at $r = 1$, as they were expressed before we transformed them to the inner co-ordinates. Thus, one coefficient remains undetermined for now,

$$\psi_1(r,\mu) = \left(\frac{1}{2}r^2 + \frac{c_{\mathrm{II}}}{r}\right)\left(1-\mu^2\right). \tag{6.36}$$

6.8 Inner first-order solution

We proceed to make a perturbation expansion of the inner streaming function,

$$\Psi = \Psi_1 + \varepsilon\Psi_2 + \varepsilon^2\Psi_3 + ... \tag{6.37}$$

Substitution into Eq. (6.29a) yields the first-order equation

$$\mathrm{i}\partial_\eta^2\Psi_1 = \frac{1}{2}\partial_\eta^4\Psi_1, \tag{6.38}$$

where the factor i is from the time derivative. We know that the inner and outer solution should tend asymptotically towards each other for $\eta \to \infty$ and $r \to 1$. From this and Eq. (6.36) we infer that

$$\Psi_1(\eta,\mu) = \Phi_1(\eta)\big(1-\mu^2\big). \tag{6.39}$$

Eq. (6.38) can be solved in two steps if we set $\zeta(\eta) = \partial_\eta^2\Phi_1(\eta)$ and thereby $\partial_\eta^2\zeta = 2\,\mathrm{i}\zeta$. The latter equation has the solution $\zeta(\eta) = C_\mathrm{I}\,\mathrm{e}^{(1+\mathrm{i})\eta} + C_\mathrm{II}\,\mathrm{e}^{-(1+\mathrm{i})\eta}$, which we integrate twice to obtain

$$\Phi_1(\eta) = C_\mathrm{I}\,\mathrm{e}^{(1+\mathrm{i})\eta} + C_\mathrm{II}\,\mathrm{e}^{-(1+\mathrm{i})\eta} + C_\mathrm{III}\eta + C_\mathrm{IV}, \tag{6.40}$$

where the coefficients C_I and C_II have been redefined. The no-slip conditions $\Psi_1(0) = 0$ and $\partial_\eta\Psi_1(0) = 0$ leads to $C_\mathrm{IV} = -\big(C_\mathrm{I} + C_\mathrm{II}\big)$ and $C_\mathrm{III} = (1+\mathrm{i})\big(C_\mathrm{II} - C_\mathrm{I}\big)$, and so we end up with

$$\Psi_1(\eta,\mu) = \Big[C_\mathrm{I}\,\mathrm{e}^{(1+\mathrm{i})\eta} + C_\mathrm{II}\,\mathrm{e}^{-(1+\mathrm{i})\eta} + (1+\mathrm{i})\big(C_\mathrm{II} - C_\mathrm{I}\big)\eta - \big(C_\mathrm{I} + C_\mathrm{II}\big)\Big]\big(1-\mu^2\big). \tag{6.41}$$

We determine the remaining constants in the matching process in the next section.

6.9 First-order asymptotic matching

We have derived the inner and outer solutions to first order,

$$\Psi_1(\eta,\mu) = \Big[C_\mathrm{I}\,\mathrm{e}^{(1+\mathrm{i})\eta} + C_\mathrm{II}\,\mathrm{e}^{-(1+\mathrm{i})\eta} + (1+\mathrm{i})\big(C_\mathrm{II} - C_\mathrm{I}\big)\eta - \big(C_\mathrm{I} + C_\mathrm{II}\big)\Big]\big(1-\mu^2\big), \tag{6.42a}$$

$$\psi_1(r,\mu) = \left(\frac{1}{2}r^2 + \frac{c_\mathrm{II}}{r}\right)\left(1-\mu^2\right), \tag{6.42b}$$

and are ready to match them. Substitution of $r = 1 + \frac{\sqrt{2}\eta}{|M|}$ into the inner solution and a subsequent Taylor expansion to first order in $\frac{\sqrt{2}\eta}{|M|} \ll 1$ yields

$$\psi_1(\eta,\mu) = \left[\tfrac{1}{2}\left(1 + \tfrac{\sqrt{2}\eta}{|M|}\right)^2 + c_\mathrm{II}\left(1 + \tfrac{\sqrt{2}\eta}{|M|}\right)^{-1}\right]\left(1-\mu^2\right) \tag{6.43a}$$

$$\approx \left[\tfrac{1}{2}\left(1 + 2\tfrac{\sqrt{2}\eta}{|M|}\right) + c_\mathrm{II}\left(1 - \tfrac{\sqrt{2}\eta}{|M|}\right)\right]\left(1-\mu^2\right) \tag{6.43b}$$

$$= \left[\big(\tfrac{1}{2} + c_\mathrm{II}\big) + \tfrac{\sqrt{2}}{|M|}\big(1 - c_\mathrm{II}\big)\eta\right]\left(1-\mu^2\right) \tag{6.43c}$$

The Taylor expansion is justified since $\frac{\sqrt{2}\eta}{|M|} = r-1 \ll 1$ when r approaches 1 (corresponding to a in dimensionalised co-ordinates). As $\Psi = \frac{|M|}{\sqrt{2}}\psi$, the matching condition is

$$\lim_{\eta\to\infty} \Psi_1 = \lim_{r\to 1} \frac{|M|}{\sqrt{2}}\psi_1. \tag{6.44}$$

Comparing Eqs. (6.42a) and (6.43), we see that $\Psi(\eta,\mu)$ can not increase faster than proportionally to η as we let $\eta \to \infty$. Consequently, C_{I} must be zero. This leaves the conditions $(1+\mathrm{i})C_{\mathrm{II}} = 1-c_{\mathrm{II}}$ and $C_{\mathrm{II}} = -\frac{|M|}{\sqrt{2}}\left(c_{\mathrm{II}}+\frac{1}{2}\right)$, which in Section D.4 in Appendix D are shown to be fulfilled for

$$c_{\mathrm{II}} = -\frac{1}{2}\frac{|M|(1+\mathrm{i})+2\sqrt{2}}{|M|(1+\mathrm{i})-\sqrt{2}} \approx -\frac{1}{2}, \tag{6.45a}$$

$$C_{\mathrm{II}} = \frac{3}{2}\frac{|M|}{|M|(1+\mathrm{i})-\sqrt{2}} \approx \frac{3}{2}\frac{1}{1+\mathrm{i}} = \frac{3}{4}(1-\mathrm{i}), \tag{6.45b}$$

where we exploit that $|M| \gg 1$ to reduce the coefficients. Insertion of $C_{\mathrm{I}} = 0$ and Eq. (6.45) into Eq. (6.42) yields the first-order solutions

$$\Psi_1(\eta,\mu) = \frac{3}{2}\left[\eta - \frac{1}{2}(1-\mathrm{i})\left(1-\mathrm{e}^{-(1+\mathrm{i})\eta}\right)\right]\left(1-\mu^2\right), \tag{6.46a}$$

$$\psi_1(r,\mu) = \frac{1}{2}\left(r^2-\frac{1}{r}\right)\left(1-\mu^2\right). \tag{6.46b}$$

Having determined these, we can proceed to second order.

6.10 Inner second-order solution

To second order the inner streaming equation, Eq. (6.29a), reduces to

$$\partial_t(\partial_\eta^2\Psi_2) + \frac{\partial\left(\Psi_1,\partial_\eta^2\Psi_1\right)}{\partial(\eta,\mu)} + \frac{2\mu}{1-\mu^2}\left(\partial_\eta^2\Psi_1\right)\left(\partial_\eta\Psi_1\right) = \frac{1}{2}\partial_\eta^4\Psi_2. \tag{6.47}$$

We recall that the reason for going beyond first order is that the time averages of the first-order fields are zero. Thus, we have to go to second order to determine time-averaged effects. Taking the time average (denoted by $\langle\,\bullet\,\rangle$) eliminates the first term,

$$\left\langle\frac{\partial\left(\Psi_1,\partial_\eta^2\Psi_1\right)}{\partial(\eta,\mu)}\right\rangle + \frac{2\mu}{1-\mu^2}\left\langle\left(\partial_\eta^2\Psi_1\right)\left(\partial_\eta\Psi_1\right)\right\rangle = \frac{1}{2}\partial_\eta^4\left\langle\Psi_2\right\rangle. \tag{6.48}$$

The terms that are comprised of products of the first-order solution are calculated thoroughly in Section **??** in Appendix D, after which we end up with

$$\partial_\eta^4\langle\Psi_2\rangle = \frac{9}{2}\left[\mathrm{e}^{-2\eta} - \mathrm{e}^{-\eta}\cos\eta + \mathrm{e}^{-\eta}\sin\eta - 2\eta\,\mathrm{e}^{-\eta}\sin\eta\right]\mu\left(1-\mu^2\right). \tag{6.49}$$

After four consecutive integrations we obtain

$$\langle\Psi_2(\eta,\mu)\rangle = \frac{9}{2}\left[\frac{1}{16}\,\mathrm{e}^{-2\eta}+\frac{5}{4}\,\mathrm{e}^{-\eta}\cos\eta+\frac{3}{4}\,\mathrm{e}^{-\eta}\sin\eta+\frac{1}{2}\eta\,\mathrm{e}^{-\eta}\sin\eta+C_{\mathrm{I}}\eta^3+C_{\mathrm{II}}\eta^2+C_{\mathrm{III}}\eta+C_{\mathrm{IV}}\right]\mu(1-\mu^2). \tag{6.50}$$

Notice that the second-order dependence on the transformed polar co-ordinate μ differs from the first-order dependence. From the condition $\langle\Psi_2(0,\mu)\rangle = 0$ we determine $C_{\mathrm{IV}} = -\frac{21}{16}$, and then $C_{\mathrm{III}} = \frac{5}{8}$ follows from the condition $\langle\partial_\eta\Psi_2(0,\mu)\rangle$. We thus have two coefficients that have yet to be determined,

$$\langle\Psi_2(\eta,\mu)\rangle = \frac{9}{2}\left[\frac{1}{16}\,\mathrm{e}^{-2\eta}+\frac{5}{4}\,\mathrm{e}^{-\eta}\cos\eta+\frac{3}{4}\,\mathrm{e}^{-\eta}\sin\eta+\frac{1}{2}\eta\,\mathrm{e}^{-\eta}\sin\eta+C_{\mathrm{I}}\eta^3+C_{\mathrm{II}}\eta^2+\frac{5}{8}\eta-\frac{21}{16}\right]\mu(1-\mu^2). \tag{6.51}$$

6.11 Outer second-order solution

Finally, we are ready to calculate the streaming outside the boundary layer which was the reason for going through the previous inner and outer first-order and inner second-order calculations. As for the inner second-order equation, we take the time average to eliminate the time derivative term, after which the outer streaming equation, Eq. (6.30a), reduces to

$$\frac{1}{r^2}\left\langle\frac{\partial(\psi_1,D^2\psi_1)}{\partial(r,\mu)}\right\rangle + \frac{2}{r^2}\left\langle(D^2\psi_1)(L\psi_1)\right\rangle = \frac{1}{|M|^2}D^4\langle\psi_2\rangle. \tag{6.52}$$

From the first order equation $D^2\psi_1 = 0$, we see that the two first terms are zero so the equation reduces to

$$D^4\langle\psi_2\rangle = 0. \tag{6.53}$$

Eq. (6.53) is solved in Section D.6 in Appendix D where the angular dependence is inferred from the inner second-order solution. The result is

$$\langle\psi_2(r,\mu)\rangle = \left[c_{\mathrm{I}}r^5 + c_{\mathrm{II}}r^3 + c_{\mathrm{III}} + c_{\mathrm{IV}}r^{-2}\right]\mu\left(1-\mu^2\right). \tag{6.54}$$

The condition in Eq. (6.30c) that the second-order streaming function can not increase faster than proportionally to r (so that the second-order velocity field dies out far from the sphere) rules out the two first terms,

$$\langle\psi_2(r,\mu)\rangle = \left[c_{\mathrm{III}} + c_{\mathrm{IV}}r^{-2}\right]\mu\left(1-\mu^2\right). \tag{6.55}$$

The two other coefficients are determined by the asymptotic matching condition.

6.12 Second-order asymptotic matching

The inner and outer streaming functions to be matched are

$$\langle\psi_2\rangle = \left[c_{\mathrm{III}} + c_{\mathrm{IV}}r^{-2}\right]\mu\left(1-\mu^2\right), \tag{6.56a}$$

$$\langle\Psi_2\rangle = \frac{9}{2}\left[\frac{1}{16}\,\mathrm{e}^{-2\eta} + \frac{5}{4}\,\mathrm{e}^{-\eta}\cos\eta + \frac{3}{4}\,\mathrm{e}^{-\eta}\sin\eta + \frac{1}{2}\eta\,\mathrm{e}^{-\eta}\sin\eta + C_{\mathrm{I}}\eta^3 + C_{\mathrm{II}}\eta^2 + \frac{5}{8}\eta - \frac{21}{16}\right]\mu(1-\mu^2). \tag{6.56b}$$

As for the first-order case, we perform the matching by first rewriting the outer solution in terms of the inner variable η and then Taylor expanding the result for $r \ll 1$,

$$\begin{aligned}
\langle \psi_2(r,\mu) \rangle &= \left[c_{\mathrm{III}} + c_{\mathrm{IV}} r^{-2}\right] \mu\left(1-\mu^2\right) && \text{(6.57a)}\\
&= \left[c_{\mathrm{III}} + c_{\mathrm{IV}} \left(1 + \tfrac{\sqrt{2}\eta}{|M|}\right)^{-2}\right] \mu\left(1-\mu^2\right) && \text{(6.57b)}\\
&\approx \left[c_{\mathrm{III}} + c_{\mathrm{IV}} \left(1 - 2\tfrac{\sqrt{2}\eta}{|M|}\right)\right] \mu\left(1-\mu^2\right) && \text{(6.57c)}\\
&= \tfrac{\sqrt{2}}{|M|}\left[\tfrac{|M|}{\sqrt{2}}\left(c_{\mathrm{III}} + c_{\mathrm{IV}}\right) - 2\, c_{\mathrm{IV}}\eta\right] \mu\left(1-\mu^2\right). && \text{(6.57d)}
\end{aligned}$$

Finally we multiply by $\frac{|M|}{\sqrt{2}}$ to obtain the same scale as the inner solution, and match,

$$\lim_{\eta\to\infty} \Psi_2 = \lim_{r\to 1} \tfrac{|M|}{\sqrt{2}} \psi_2. \tag{6.58}$$

We see in Eq. (6.57d) that the outer solution is proportional to the inner radial co-ordinate η in the vicinity of the boundary layer. Hence, the inner solution must also be proportional to η when $\eta \to \infty$ which leads to $C_{\mathrm{I}} = C_{\mathrm{II}} = 0$. Furthermore, we see that $c_{\mathrm{IV}} = -\frac{45}{32}$ and that $c_{\mathrm{III}} = -c_{\mathrm{IV}}$. Thus, the final result is

$$\langle \psi_2(r,\mu) \rangle = \frac{45}{32}\left(1 - \frac{1}{r^2}\right)\mu\left(1-\mu^2\right), \tag{6.59a}$$

$$\langle \Psi_2(\eta,\mu) \rangle = \frac{9}{2}\left[\frac{1}{16}\,\mathrm{e}^{-2\eta} + \frac{5}{4}\,\mathrm{e}^{-\eta}\cos\eta + \frac{3}{4}\,\mathrm{e}^{-\eta}\sin\eta + \frac{1}{2}\eta\,\mathrm{e}^{-\eta}\sin\eta - \frac{21}{16} + \frac{5}{8}\eta\right]\mu(1-\mu^2). \tag{6.59b}$$

In the next section we calculate the outer streaming from Eq. (6.59a).

6.13 Streaming outside the boundary layer

In this final section of the chapter, we calculate the streaming and visualise it. The outer second-order streaming function is given in Eq. (6.59a) and its relation to the second-order velocity field is inferred from Eq. (6.17),

$$\langle \boldsymbol{v}_2 \rangle = -\boldsymbol{e}_r \frac{1}{r^2}\,\partial_\mu \psi_2 - \boldsymbol{e}_\theta \frac{\left(1-\mu^2\right)^{-\frac{1}{2}}}{r}\,\partial_r \psi_2. \tag{6.60}$$

Insertion of Eq. (6.59a) into Eq. (6.60) yields

$$\langle \boldsymbol{v}_2 \rangle = \boldsymbol{e}_r \frac{45}{32}\left(\frac{1}{r^4} - \frac{1}{r^2}\right)\left(1-3\mu^2\right) - \boldsymbol{e}_\theta \frac{45}{16}\frac{1}{r^4}\,\mu\left(1-\mu^2\right)^{\frac{1}{2}}. \tag{6.61}$$

The spherical co-ordinates can be transformed back to the regular ones by insertion of $\mu = \cos\theta$. Furthermore, we recall that the variable r is measured in units of the sphere

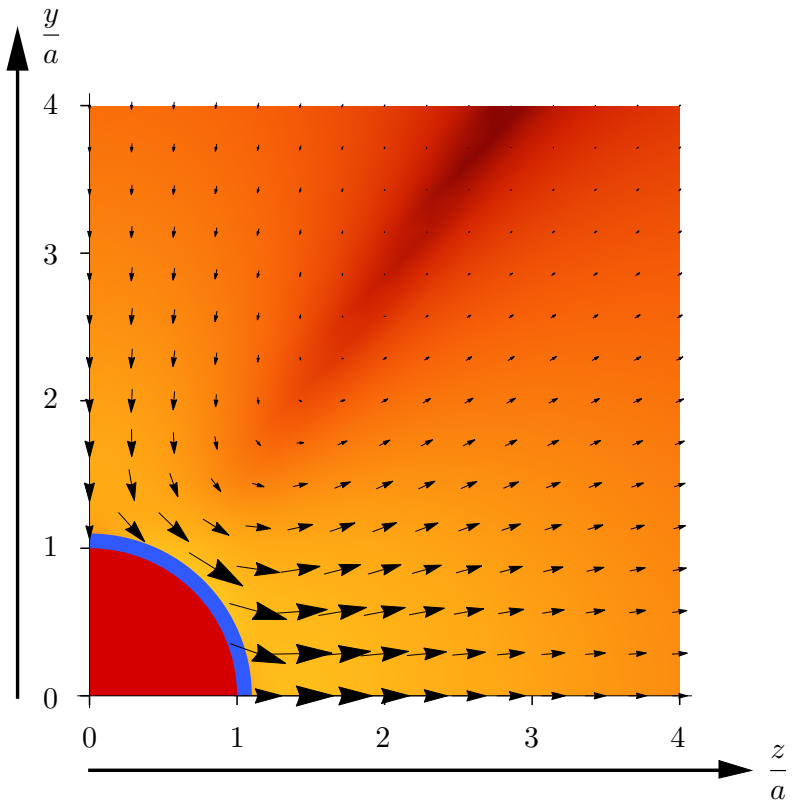

Figure 6.2 Colour plot of the sphere streaming magnitude going from minimum of 0.002 (dark red) to maximum of 0.97 (yellow) on a logarithmic scale, in units of $\varepsilon v_\mathrm{a} = v_\mathrm{a}^2(\omega a)^{-1} \approx 0.6$ mm/s. The value is for water, $v_\mathrm{a} \approx 0.3$ m/s, $\alpha = 12$ µm , and $f \approx 2$ MHz corresponding to $\lambda \approx 750$ µm . The red quadrant is sphere and the blue area its boundary layer region where the outer streaming expression is invalid. The distances are normalised with the radius a.

radius a, and the streaming amplitude in units of $\varepsilon v_\mathrm{a} = v_\mathrm{a}^2(\omega a)^{-1}$. After the transformation to the variable θ and the substitution of the dimensionalised quantities, we obtain

$$\langle \boldsymbol{v}_2 \rangle = \frac{v_\mathrm{a}^2}{\omega a}\frac{45}{32}\left[\boldsymbol{e}_r\left(\frac{a^4}{r^4}-\frac{a^2}{r^2}\right)\left(1-3\cos^2\theta\right)-\boldsymbol{e}_\theta\, 2\,\frac{a^4}{r^4}\cos\theta\sin\theta\right]. \tag{6.62}$$

Eq. (6.62) is the final result of our analytical calculations. It is an expression for the streaming velocity outside the boundary layer region, for a rigid sphere in the incompressible flow approximation and in the limits where $\delta \ll a \ll \lambda$, $\varepsilon \ll 1 \ll |M|$ and $v_\mathrm{a} \ll c_0$.

We have plotted the streaming in Figure 6.2, and we see in Figure 6.1 that the axis of oscillation is the z axis. Thus, the direction of the streaming is outwards along the axis of oscillation, which is also the axis of azimuthal symmetry. Along the axis perpendicular to the axis of oscillation (in this case the y axis), the streaming is inwards. The streaming is strongest at the sphere surface at the angle $\theta \approx \frac{\pi}{4} = 45^\circ$, and lowest in the direction

given by the angle $\theta \approx \frac{5\pi}{16} \approx 56^\circ$. The first angle is found numerically for r fixed at the edge of the boundary layer, which we have chosen as $r = 1.1a$, and the second angle is where the angular part $1 - 3\cos^2\theta$ in $\langle v_2 \rangle_r$ is close to zero. We recall that for water at MHz frequencies, the boundary layer thickness is $\delta \approx 0.5$ µm, and from the discussion of the radiation force, we recall that our choice of the boundary layer region edge is several times δ from the surface, but otherwise arbitrary. The choice $r = 1.1a$ corresponds to 3δ for $a = 15$ µm.

The purpose of the analytical calculations in this chapter was to determine the streaming expression in Figure 6.2 in order to compare this with the streaming generated by channel walls, and see if it drags sub-micron particles towards the pressure node. This comparison is the subject of Chapter 7.

Chapter 7

Influence of a seed particle on the streaming pattern

In this chapter we compare the sphere streaming determined in Chapter 6 with the channel streaming. The channel streaming is generated by channel walls, and we intent to compare it to the sphere streaming, which we calculated for an unbounded fluid (no surrounding walls). We thus combine results that are invalid in each other's domain. Nevertheless, we shall make the combination, while we understand that the results are rough estimates. Afterwards, we supplement this comparison with numerical calculations carried out in COMSOL.

We begin with the comparison based on analytical expressions. The system is shown in Figure 7.1. The simultaneous bounded- and unboundedness is illustrated by the dashed channel walls and the dashed boundary layers generated at them. The illustration of the sphere streaming (red) is based on Figure 6.2 and indicates that there may be areas along the two axes, where the streaming patterns cancel each other out.

For the channel streaming we use the analytical expression derived in Ref. [24]

$$\langle \boldsymbol{v}_2 \rangle_{\mathrm{ch}} \approx v_{\mathrm{str}} \left[\sin(\pi \tilde{z}) \left(\frac{3}{2}\tilde{y}^2 - \frac{1}{2} \right) \boldsymbol{e}_z + \cos(\pi \tilde{z}) \, \frac{\pi \alpha}{2} \left(\tilde{y} - \tilde{y}^3 \right) \boldsymbol{e}_y \right], \tag{7.1}$$

where a tilde denotes a normalisation with respect to the relevant channel dimension,

$$\tilde{z} = \frac{2z}{w} \quad \text{with} \quad -1 < \tilde{z} < 1, \qquad \tilde{y} = \frac{2y}{h} \quad \text{with} \quad -1 < \tilde{y} < 1, \tag{7.2}$$

and where v_{str} and α are the amplitude and channel aspect ratio,

$$v_{\mathrm{str}} \approx \frac{1}{2} \frac{v_{\mathrm{a}}^2}{c_0}, \qquad \alpha \equiv \frac{h}{w} \ll 1. \tag{7.3}$$

The expression is a good approximation for shallow channels which have low aspect ratios α. We make a compromise between the approximation in Eq. (7.1) valid for shallow channels, and the expression in Eq. (6.62) valid in unbounded fluids. For a seed particle radius a_{s} of the order 10 µm , channel width $w = 380$ µm and channel height $h = 180$ µm,

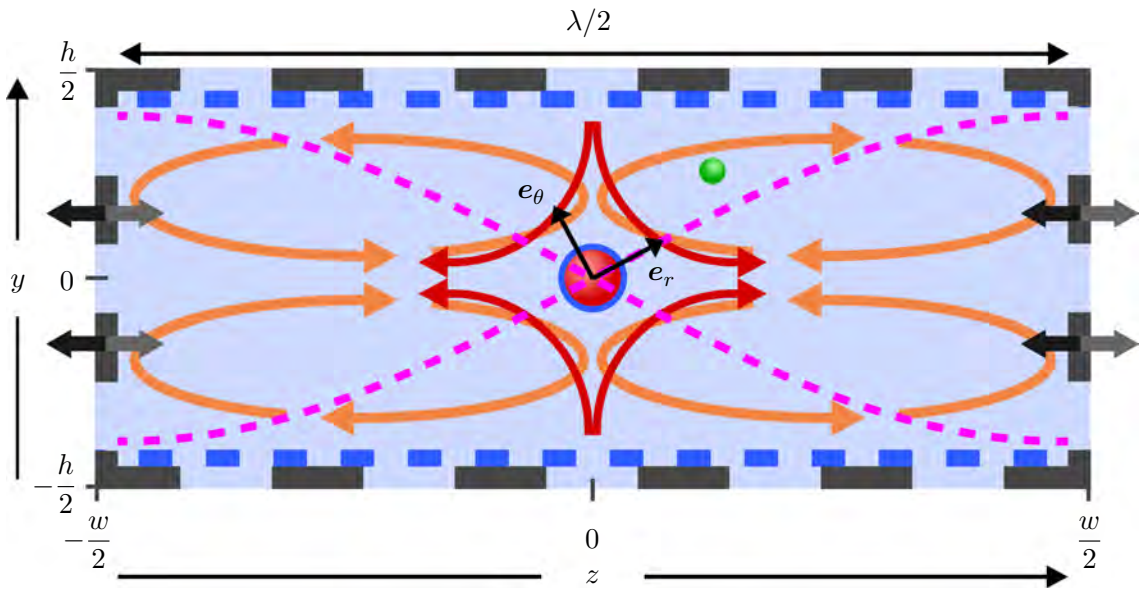

Figure 7.1 System for comparison of the streaming (red arrows) generated by a spherical seed particle (red) at a pressure node, and streaming (orange) generated by boundary walls. For the former we use an expression valid in a an unbounded fluid (no surrounding walls), and latter exists only in the presence of surrounding walls. Hence, the dashed channel walls (grey) and wall boundary layers (blue). The fluid (light blue) supports a half-wavelength standing pressure wave (magenta), and a small probe particle (green) experiences a drag force due to the sum of the streaming patterns.

the aspect ratio is $\alpha = 0.47 < 1$, and the walls are far from the sphere compared to its size ($a_\mathrm{s} \ll h, w$). The channel is thus semi-shallow, while the walls are many radii from the sphere. The streaming velocity fields in Eqs. (6.62) and (7.1) are added using that $\boldsymbol{e}_r = \sin\theta\,\boldsymbol{e}_y + \cos\theta\,\boldsymbol{e}_z$ and $\boldsymbol{e}_\theta = \cos\theta\,\boldsymbol{e}_y - \sin\theta\,\boldsymbol{e}_z$ in the yz-plane. The drag force on a probe particle of radius a_p that is initially at rest, is given by Eq. (4.16) for $\boldsymbol{v}^\mathrm{p} = \boldsymbol{0}$ and $\boldsymbol{v}$ equal to the sum of the streaming velocity fields. If $\langle \boldsymbol{v}_2 \rangle_\mathrm{s}$ denotes the streaming velocity field due to the seed particle, the drag force expression becomes

$$\boldsymbol{F}^\mathrm{drag} = 6\pi\eta a_\mathrm{p} \left(\langle \boldsymbol{v}_2 \rangle_\mathrm{s} + \langle \boldsymbol{v}_2 \rangle_\mathrm{ch} \right). \tag{7.4}$$

In Figure 7.2 the drag force magnitude F^drag on a probe particle is illustrated for the upper right part of the channel in Figure 7.1. As the drag force is proportional to the streaming velocity, the plot (without the caption) could just as well illustrate the streaming and we shall therefore mention the force and the streaming interchangeably.

The plot in Figure 7.1(a) is for $a_\mathrm{s} = 0$ and it is thus a reference plot, showing only the drag force due to the channel streaming. The figure shows the upper right of the four circulating streams that we also plotted in Figure 4.3. It is strongest at the top walls, where the velocity has to decay to zero, and weakest in its centre at $(z, y) = (90, 40)$ µm and four corners at $(z, y) = (0, 0)$, $(180, 0)$, $(180, 80)$ and $(0, 80)$ µm. We recall that this

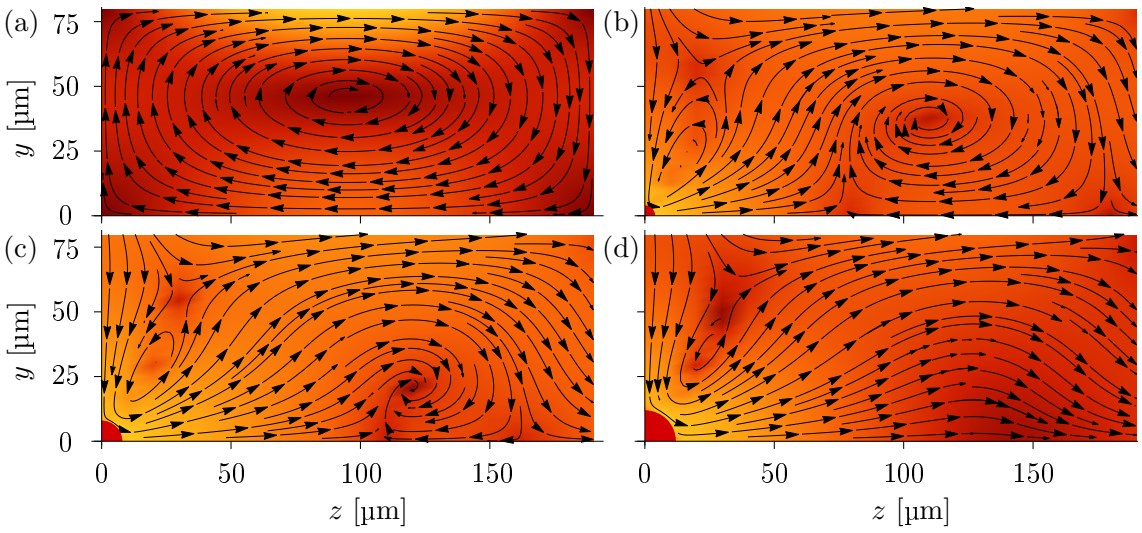

Figure 7.2 Colour plots of the drag force magnitude F^{drag} due to the sum of the sphere streaming and channel streaming, and vector plots of the force direction (no scaling) for different seed particle radii a_{s}. The colour varies from dark red (lowest magnitude $\boldsymbol{F}^{\text{drag}}_{\text{min}}$) to yellow (highest magnitude $\boldsymbol{F}^{\text{drag}}_{\text{max}}$) on a (a) linear scale and (b)-(d) logarithmic scale. The red quadrant at the origin is the seed particle, and the plots show only the upper right quarter of the channel in Figure 7.1 for $h = 180$ µm and $w = 380$ µm. We use parameters for water and $v_{\text{a}} = 1$ m/s. The seed particle radius a_{s}, minimum force magnitude $\boldsymbol{F}^{\text{drag}}_{\text{min}}$, and maximum force magnitude $\boldsymbol{F}^{\text{drag}}_{\text{max}}$ are (a) 0 µm, 0 N and 5 pN, (b) 4 µm, 5 fN and 0.2 nN, (c) 8 µm, 8 fN and 0.2 nN, and (d) 12 µm, 0.2 pN and 0.5 nN.

channel streaming is the motivation for this thesis, since it complicates focusing of sub-micron particles at the channel centre $(z, y) = (0, 0)$ µm. As evident from the figure, the channel streaming drags sub-micron particles near $y = 0$ towards the channel centre (and the pressure node). However, when the particles reach the area close the centre ($z = 0$), they are dragged upwards to the top wall and then towards the upper right corner. The sub-micron particles, for which the streaming-induced drag force dominates the motion, will thus not focus.

Figure 7.2(b) shows the drag force in the presence of a seed particle of radius $a_{\text{s}} = 4$ µm. According to the figure, even such a small seed particle will turn the direction of the drag force along the y axis from upwards to downwards. It also creates what looks like a force corresponding to a small circulating flow close to the particle, at an angle of roughly $\theta \approx 60^{\circ}$. The direction of the force also changes along the first part of the z axis, from inwards to outwards. Finally, the centre of the original circulating flow has moved a little down and to the right. The plot in Figure 7.2(b) is for $a_{\text{s}} = 4$ µm and the boundary layer at the sphere surface has the thickness $\delta \approx 0.5$ µm. The sphere radius is thus barely in the limit $\delta \ll a_{\text{s}}$ where the expression for the sphere streaming is valid. This adds to the roughness of the estimation.

The plot shown in Figure 7.2(c) is for $a_{\text{s}} = 8$ µm which too is barely in the limit

$\delta \ll a_\mathrm{s}$. The drag force due to the seed particle streaming dominates in the left part of the plot, close to the seed particle. This left part closely resembles the sphere streaming shown in Figure 6.2. In the right part of the plot, for $z > 100$ µm , the channel drag force pattern from Figure 7.2(a) is still recognisable, but the original centre of the channel pattern has moved further down and to the right.

Finally, Figure 7.2(d) shows a plot for a seed particle radius of $a_\mathrm{s} = 12$ µm , which is in the limit $\delta \ll a_\mathrm{s}$. The plot is qualitatively different from the two previously discussed. The small circulation in the force close to the seed particle is still visible, but what corresponded to the centre of the channel streaming is not. The direction of the force is outwards along the z axis all the way to the wall. This indicates that the streaming due to the seed particle might not make it easier to trap sub-micron particles at the pressure node. As seen in Figure 7.2(a), the streaming in the absence of a seed particle assists the trapping along the z axis and counteracts it along the y axis,. In Figure 7.2(d), we see the opposite its presence. The streaming counteracts the trapping along the z axis and assists it along the y axis. However, in Figure 7.2(d) we still see an indication of what could be a small circulating flow close to the seed particle. Sub-micron particles would perhaps stay in the flow but it is difficult say from looking at the figure.

It is obvious to consider varying other quantities than the seed particle radius and examine how the total drag force changes. However, the channel streaming and seed particle streaming are same phenomenon and therefore, they have the same dependence on the amplitude v_a of the applied oscillating first-order velocity field. We see that in Eqs. (6.62) and (7.1). Increasing the channel width w is an option, however, since the dependence of the two streaming patterns on the width differ from each other. If we substitute $\omega = c_0\lambda^{-1}$ into Eq. (6.62), we see that the seed particle streaming is proportional to the wavelength λ, which is twice the channel width. In Eq. (7.1), which gives the channel streaming, the dependence on the channel width is implicit in the variables $\tilde{y}$ and $\tilde{z}$ which are normalised with respect to the width and height. We shall not consider this width dependence further, as the purpose of the section was to make a rough estimation of the total streaming pattern in the presence of the seed particle.

We conclude from the investigation in this section that the presence of a seed particle alters the total streaming pattern in the channel. However, the altered streaming pattern does not seem to allow focusing of sub-micron particles, due to the direction of the drag force being outwards along the axis of oscillation. The only indication of the opposite is what looks like a small circulating flow close to the seed particle.

Once again, we stress that the investigation is based on two analytical results that are incompatible with each other's domain. We used the expression for the streaming from a sphere in a fluid that is not surrounded by any wall boundaries, and added it to the channel streaming which is a consequence of such boundaries. Furthermore, the channel we considered was not very shall but nevertheless, we used an expression for streaming in a very shallow channel. The point is that the results of this section are merely indicative and of high uncertainty. In the next section we supplement the results with numerical calculations.

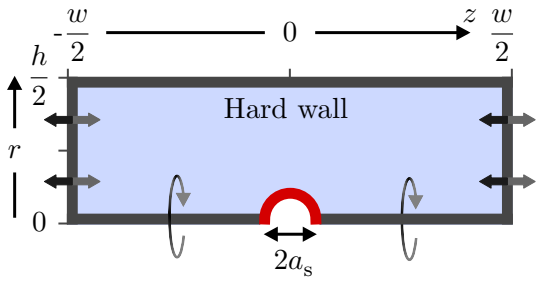

Figure 7.3 Axially symmetric geometry consisting of a cylinder of height w and radius $\frac{h}{2}$ with a central seed particle of radius a_s (red surface) used in the COMSOL simulations. As usual, we use water as the suspending medium. The cylinder is shown with its axis horizontally oriented, and due to the axial symmetry indicated by the circulating arrows, only half of its cross section is shown. The cylinder top and bottom oscillates as indicated by the thick horizontal arrows.

7.1 Simulations of acoustic streaming

In this section we present results from numerical calculations of streaming in the presence of a seed particle. A full 3D simulation of a rectangular channel and a spherical seed particle is too demanding for the computers available in the work with this thesis. We can partly overcome this limitation by instead simulating the axially symmetric problem consisting of a cylinder with oscillating top and bottom, which contains a spherical seed particle at its centre. Due to the axisymmetry, we can solve this 3D problem as if it was a 2D one. The system is sketched in Figure 7.3 with the cylinder rotated so its axis of symmetry is horizontal.

7.1.1 Setting up COMSOL

We are not restricted by the limit $\alpha \ll 1$ as in the previous section, so we consider the cylinder dimensions $h = 240$ µm and $w = 380$ µm. The reason for choosing a cylinder radius $\frac{h}{2}$ larger than 160 µm, which is the width of all the previously considered rectangular channels, is that we also want to see how the streaming is far from the seed particle in the r direction. We choose a polystyrene seed particle of radius $a_\mathrm{s} = 12$, similar to those in the experiments reported in Ref. [1].

COMSOL takes care of the axis of symmetry such that the pressure and velocity fields and there first-order derivatives a continuous on it. On the hard wall and on the surface of the rigid seed particle, we impose no-slip conditions on both the first-and second order the velocity field: $\boldsymbol{v}_1 = \boldsymbol{v}_2 = \boldsymbol{0}$. The oscillating top and bottom of the cylinder is implemented by demanding the first order velocity field to be $\boldsymbol{v}_1 = \mathrm{v}_{bc}\,\mathrm{e}^{-\mathrm{i}\omega t}$ on those walls. Here, the amplitude is $\mathrm{v}_{bc} = d\omega$, where $d = 0.22$ nm is the displacement and $\omega = 2\pi\times$ 1.97 MHz the angular frequency corresponding to a half-wavelength resonance in the cylinder. The value or d is of an order typical for experiments [30].

The second-order condition on the top and bottom is that there must be no mass flux

through them: $\boldsymbol{n} \cdot [\rho_0 \langle \boldsymbol{v}_2 \rangle + \langle \rho_1 \boldsymbol{v}_1 \rangle] = 0$ on the top and bottom boundaries. For the pressure we keep on all boundaries the weak form condition $\boldsymbol{n} \cdot \boldsymbol{J} = 0$, which COMSOL has as the default, for the currents $\boldsymbol{J}$ given by the first-order and second-order time-averaged continuity equation. We shall not go into details about the generalised currents $\boldsymbol{J}$ and driving forces $\boldsymbol{F}$, since they can be found by rewriting the first-order and time-averaged second-order governing equations, Eqs. (2.16) and (2.22), on the form of the generic Cartesian continuity equation in Eq. (3.2). In doing so, one has to remember that the volume measure in Eq. (3.4) is $\mathrm{d}\boldsymbol{r} = r\,\mathrm{d}r\,\mathrm{d}z\,\mathrm{d}\phi$ in cylindrical co-ordinates but we shall not go into further details here, as we merely use COMSOL as a tool.

A final aspect to touch upon when setting up COMSOL is the size of the mesh elements discussed in Chapter 3. The size has to be decreased until the solutions converge. We refer to Ref. [31] in which the authors present simulations of acoustic streaming in a rectangular channel of dimensions similar to the cylinder that we consider. For a given solution g to one of the physical fields, the authors define a convergence parameter $C(g)$ with respect to a reference solution,

$$C(g) = \sqrt{\frac{\int (g - g_{\mathrm{ref}})\,\mathrm{d}a}{\int (g_{\mathrm{ref}})^2\,\mathrm{d}a}}. \tag{7.5}$$

The reference solution is for a maximum boundary mesh length $d_{\mathrm{mesh}} = 0.3\delta$, a third of the boundary layer thickness. In the light of an analysis of the mesh convergence, the authors conclude that $d_{\mathrm{mesh}} = 0.5\delta$ gives a relative convergence of $C \leq 0.002$, sufficient for their streaming analysis. As an analysis of mesh convergence is outside the scope of this thesis, we use their maximum boundary mesh size of $d_{\mathrm{mesh}} = 0.5\delta \approx 0.2$ µm. In the bulk, we allow the side length of the mesh elements to increase up to $50\delta \approx 19$ µm.

7.1.2 The simulated acoustic fields

The result of the simulation is a first-order velocity field amplitude $v_{\mathrm{a}} = 0.28$ m/s, a first-order pressure field amplitude $p_{\mathrm{a}} = 0.27$ MPa and a second-order time-averaged maximum pressure field of $\langle p_2 \rangle_{\mathrm{max}} = 8.5$ Pa. Notice that we used a wall displacement of the same order of magnitude as seen in the experiments referred to above, and that we get amplitudes v_{a} and p_{a} of the same order of magnitude as those used throughout the thesis for a number of estimations.

As our primary interest is the streaming (the second-order time-averaged velocity field), we turn out attention to that. The other fields are shown in Figure E.1 in Appendix E. Figure 7.4 shows two plots of the streaming: one without the seed particle (for reference), and one with a central seed particle of radius $a_{\mathrm{s}} = 12$ µm. The axis of symmetry corresponding to that in the schematic Figure 7.3 is given by $r = 0$. In Figure 7.4(a) we see that in the absence of the seed particle, the streaming is zero at the cylinder centre. Its direction is outwards along $z = 0$ and inwards along the symmetry axis ($r = 0$). Two circulating flows are generated close to the cylinder wall. We see that particles following these would move towards $z = 0$, and then away from the centre of the cylinder towards its side wall. Next, they would move along the side wall back towards the top or bottom.

In Figure 7.4(b) we see on the colour plot that the streaming generated close the seed

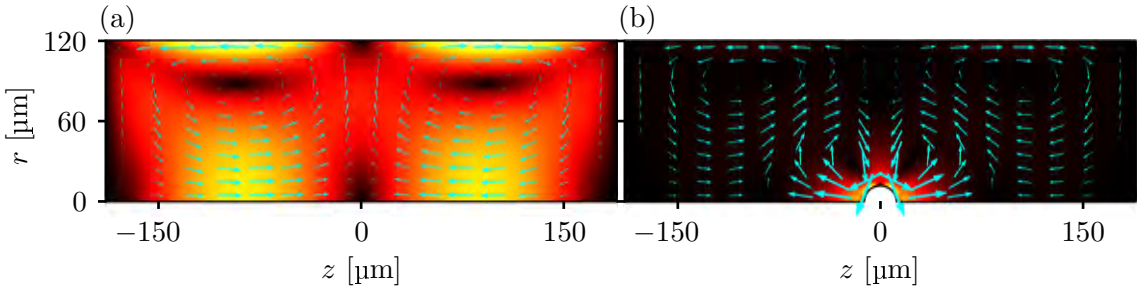

Figure 7.4 Colour plots varying linearly from zero (black) to the maximum (white) magnitude of the second-order velocity field, i.e. the streaming flow, induced by a horizontal half-wavelength resonance by the oscillations of the vertical walls (cylinder top and bottom). The axis of rotational symmetry is given by $r = 0$. The vector plot shows both the direction and magnitude of the streaming flow. (a) Reference plots without the seed particle. The maximum streaming velocity is 7.4 µm /s and the vector size varies linearly from zero streaming magnitude (no arrow) to the maximum magnitude (largest arrow). (b) The channel contains a spherical seed particle of radius $a_s = 12$ µm in its centre. The maximum streaming velocity is 169 µm /s which is at the surface of the seed particle. The vector size varies on a logarithmic scale from zero streaming magnitude (no arrow) to the maximum magnitude (largest arrow).

particle is much stronger than the big circulating flows, which we recognise as the wall-generated streaming from Figure 7.4(a). The streaming close to the sphere consists of two circulating flows which, starting at $(r, z) = (0, \pm a_s)$, have direction outwards along the z axis until $z \approx \pm 60$ µm, after which the streaming changes direction towards the side wall at $(r, z) \approx (40, \pm 60)$ µm. Then its direction changes to be towards $z = 0$, from where it ends the circulation by having direction towards the surface of the seed particle. These circulating flows close to the seed particle qualitatively resemble those indicated in Figure 7.2 which is based on analytical treatment. This resemblance suggests that the seed particle does indeed generate small circulating flows. However, we can not see from either of the figures, to what degree sub-micron particles will be trapped in these. In order to get a better idea of the particle movement in these flows, we employ the COMSOL module "*Particle Tracing for Fluid Flows*".

7.1.3 Particle tracing

The particle tracing module of COMSOL computes the trajectories of particles by solving Newton's second law numerically for one or more forces acting on those particles. We specify the general expressions for the drag force and the acoustic radiation force, given in Eqs. (4.10) and (4.16). We also give as inputs the particle radius, the initial positions and material properties affecting the two forces. As usual, we treat the case of polystyrene particles in water, for which parameter values are listed in Table A.1. We study the motion of 144 particles which are initially distributed evenly, and the results are shown in Figure 7.5. Figures 7.5(a)-(e) and Figures 7.5(f)-(j) are results for the reference system

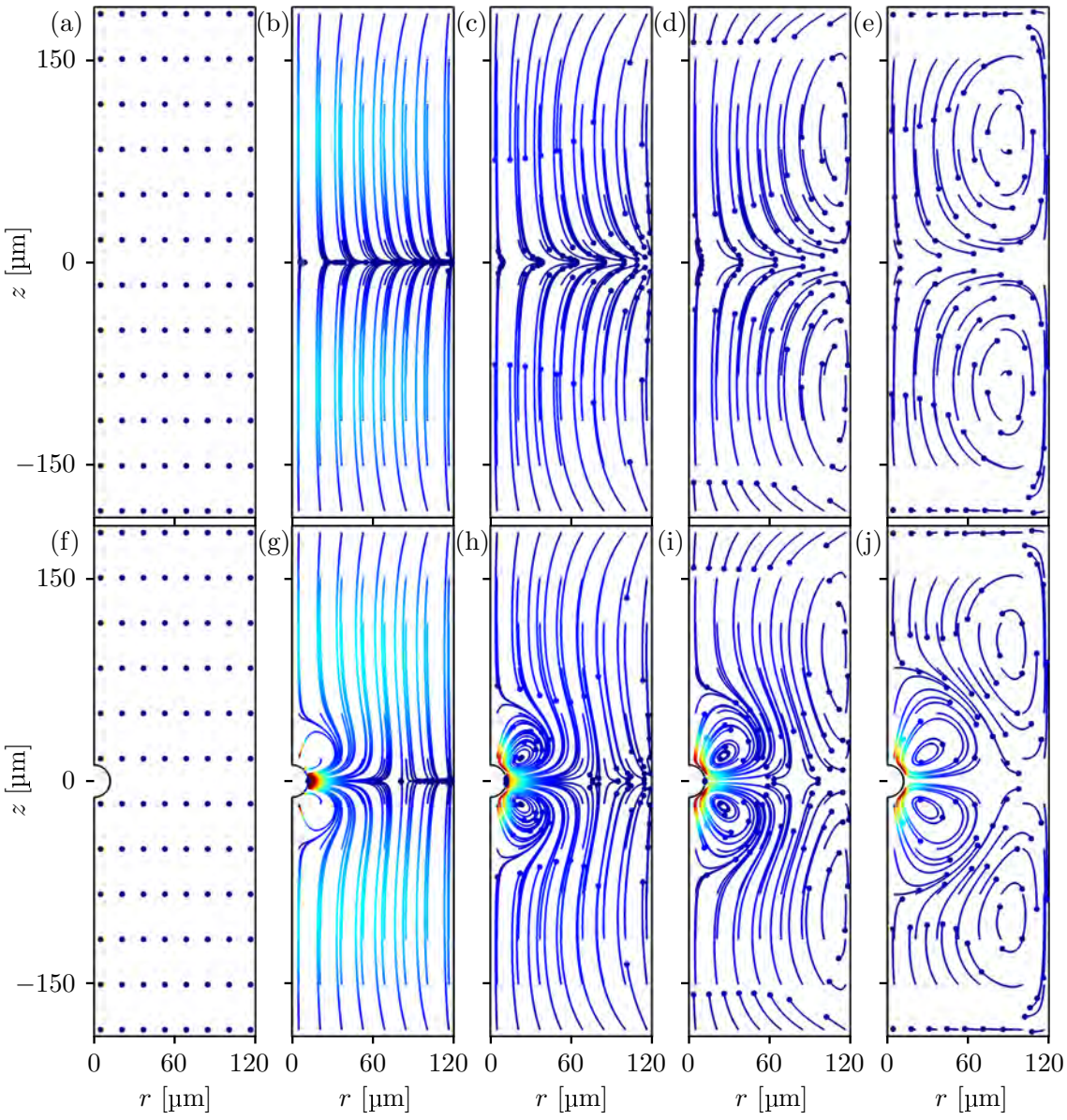

Figure 7.5 Simulations of polystyrene particle trajectories in a cylinder containing water. The fluid supports a half-wavelength standing pressure wave with a node at $z = 0$ (not pictured) excited by the oscillating top and bottom of the cylinder as sketched in Figure 7.3. The 144 particles (blue dots) are initially distributed evenly in (a) the reference system and (f) the seed particle system. The four subfigures following each of the above-mentioned show the particle trajectories (coloured lines) and positions (dots) after 15 seconds of motion for four different particle radii: 2.5 µm in (b) and (g), 1.5 µm in (c) and (h), 1.0 µm in (d) and (i), and 100 nm in (e) and (j). The particle speed varies from $v^{\mathrm{p}} = 0$ (darkest blue) to $v^{\mathrm{p}} = 169$ µm , but the maximum of the colour scale is 100 µm /s (darkest red).

(no seed particle) and the seed particle system, respectively. The initial distribution of particles is shown in Figures 7.5(a) and 7.5(f), while the remaining subfigures show the particle trajectories after 15 seconds of acoustophoretic motion. The particle size is the same for all particles within each subfigure but decreases within each row of subfigures. The micron-sized plots are included to illustrate the transition from the motion dominated by the radiation force to the motion dominated by the streaming-induced drag force.

As expected, we see in Figures 7.5(b) and 7.5(g) that the motion of the 2.5 µm-sized particles is dominated by the radiation force. By comparison with Figure 4.2 we recognise the almost straight motion, with high velocities halfway between the cylinder top or bottom and the pressure node $z = 0$, as the work of the radiation force. It is evident that all the particles are trapped at the pressure node ($z = 0$), though the seed particle streaming bends the trajectories of some of the particles, such that they also move to the surface of the seed particle. This shows that that supra-micron-sized particles are easily focused or trapped at the pressure node.

Figures 7.5(c) and 7.5(d) show a transition regime at particle radii in the approximate interval 1.0-1.5 µm. For these particle sizes, the drag force due to the channel streaming becomes of almost the same order of magnitude as the radiation force. Consequently, the particle motion is a mixture between the straight lines seen in Figures 7.5(b) and 7.5(g), and the streaming pattern in Figure 7.4(a). All the 1.5 µm-sized particles in Figure 7.5(c) has curved trajectories but stay at the pressure node when they reach, whereas some of the 1.0 µm-sized particles in Figure 7.5(d) starts circulating.

For the corresponding figures of the seed particle system, Figures 7.5(h) and 7.5(i), we see that the particles close to the cylinder wall ($r \gtrapprox 70$ µm) has approximately the same trajectories as those described above for the reference system. However, the particles that move close to the seed particle gets trapped in the small circulating generated by the seed particle. These particles do not follow the channel streaming towards the side wall and then towards the top or bottom, but stay close to the seed particle and thereby also the pressure node.

Finally, we see in Figures 7.5(e) and 7.5(j) that the drag force dominates the trajectories for particles with radii of 100 nm. The streaming patterns in Figure 7.4 are clearly visualised by the trajectories. For the particles in the reference system, this means that after reaching the pressure node, they flow to the wall ($r = 120$ µm) and then move back towards the top or bottom of the cylinder. However, the particles in the seed particle system do not all do that. Those close to the seed particle stay in its circulating flows rather than circulate in the channel-generated ones. Thus, the seed particle traps some of the particles in an area close to the pressure node. They are not completely focused, though, since most move at least 30 µm away from the node during their circulation.

It seems that the seed particle has the best effect for particles of radii approximately equal to the critical radius $a_c \approx 0.5$ µm calculated in Eq. (4.18). This is the approximate particle size where the drag force begins to dominate while the radiation force still has an impact on the particle motion. The latter thus brings the particles close to pressure node where some of them are trapped by the sphere's circulating flow, as indicated in Figure 7.5(i).

We conclude that for 1-µm-particles and sub-micron-particles, the presence of a seed

particle seem to generate small circulating flows that confine those particles to an area around the seed particle. They are, however, not completely focused at the pressure node.

Chapter 8

Conclusion and outlook

In this thesis we have studied how the presence of a seed particle affects the acoustophoretic motion of sub-micron particles suspended in microfluidic channels with transverse standing wave fields. The motivation is that in the absence of the seed particle, it is difficult to trap sub-micron particles at the pressure node in the channel centre. However, the experiments reported in Ref.[1] suggest that the presence of a seed particle inhomogeneity enables trapping of sub-micron particles. Out aim with this thesis was to explain these observations. Explanations are needed since a more profound theoretical understanding of sub-micron particles undergoing acoustophoretic motion open the way for biomedical applications involving particle detection, separation and enrichment of sub-cellular organelles, viral particles etc.

8.1 Conclusion

Our study began with Gorkov's [17] expression for the acoustic radiation force, which is valid for any incident acoustic fields. We used this to calculate how the acoustic radiation force on a small probe particle changes, when an inhomogeneity in the form of a seed particle is introduced to the pressure node at the channel centre. The goal was to see if the latter could be of at least the same order of magnitude as the streaming-induced drag force on particles of radius ~ 100 nm.

The analytical treatment showed that for sub-micron particles with a density and compressibility similar to water's, the seed particle force is a least one order of magnitude lower than the drag force. This was the most relevant result, since biological particles contain much water and consequently have a density and compressibility close to those of water. Another result was that an ideal seed particle of infinite density would make the seed particle force almost, but not quite, of the same order of magnitude as the drag force.

After concluding that the seed particle force does not seem to enable trapping of sub-micron particles, we moved on to study the streaming generated the seed particle. In order to determine an analytical expression for this streaming, we wrote the Navier-Stokes equation for incompressible flows on the form of a fourth-order scalar partial differential equation. Due to its singularity arising from the disparate length scales of the bound-

ary layer, the seed particle and the acoustic wavelength, the method of matched asymptotic expansions was employed to obtain an approximate expression for the time-averaged second-order velocity field.

Next, we used this expression to make a graphical estimation of the effect of the seed particle streaming on the total streaming pattern, which determines the drag force. The examination indicated that the seed particle would generate a small circulating flow close to its surface, that might enable trapping of sub-micron particles.

Finally, the indication from the analytical treatment was reinforced by numerical simulations of the streaming pattern and particle trajectories in a cylinder with oscillating top and bottom walls. The simulations showed small circulating flows generated in the vicinity of the sphere. Furthermore, the simulations indicated that particles just below the size, where the radiation force and the drag force are of the same order of magnitude, can be brought into these flows by the former force and then stay there due to the action of the latter.

8.2 Outlook

The work of this thesis did not fully account for the seed particle-enabled acoustic trapping of sub-micron particles that has been observed experimentally. Below some suggestions are listed for future work that might improve the work of this thesis and perhaps explain why the seed particle does enable the trapping.

8.2.1 Analytical treatment of the radiation force

We considered only the contribution to the radiation force due to fields scattered on a seed single particle. The analytical treatment could be extended by considering a cluster or some special configuration of seed particles.

8.2.2 Analytical treatment of the streaming

An obvious improvement to the analytical treatment of the streaming would be to somehow include channel boundaries in the problem when deriving the sphere streaming. Another improvement would be to use the exact expression given in Ref. [24] for the channel streaming, instead of the shallow-channel expression, when comparing it with the seed particle the sphere streaming.

8.2.3 Numerical simulations of the seed particle streaming

The effect of the seed particle on the overall streaming pattern was simulated in a closed cylindrical structure because a full 3D simulation of a sphere in a channel of rectangular cross section requires substantial computer power. It would, however be ideal to simulate the streaming in a channel as opposed to close cylinder.

Furthermore, one could also implement the contribution to the radiation force from the seed particle into the COMSOL simulations in order to compare the numerical result with the analytical predictions for water-like and ideal particles.

Appendix A

Physical constants

Table A.1 Material parameter values at ambient pressure 0.1 MPa and at temperature 300 K for water [9, 32–34], air [35], and polystyrene [36–39].

Parameter	Symbol	Water	Polystyrene	Unit
Mass density	ρ	9.966×10^{2}	1.05×10^{3}	kg m^{-3}
Isentropic speed of sound	c_0	1.502×10^{3}	2.40×10^{3}	m s^{-1}
Compressibility	κ	4.451×10^{-10}	2.38×10^{-10}	Pa^{-1}
Dynamic shear viscosity	η	8.538×10^{-4}		Pa s
Bulk viscosity	ζ	2.4×10^{-3}		Pa s
Kinematic viscosity	ν	8.567×10^{-7}		m^2 s^{-1}
Viscosity ratio	β	3.0×10^{0}		

Appendix B

Appendix to Chapter 2

B.1 Fluid description

A fluid is either a liquid or a gas that deforms continuously and with little resistance under the influence of external forces. It is composed of fluid elements, typically molecules, with an interelement distance of the order 0.3 nm for liquids and 3 nm for gases [25, chap. 1]. The continuum hypothesis states that the macroscopic properties of a fluid consisting of molecules are the same if this quantised structure is replaced by a completely continuous structure. It is valid when the length scales of the investigated particles, structures etc. are much bigger than the intermolecular distances. In this thesis we consider only fluids in lab-on-a-chip systems, where the smallest length scales are of the order 100 nm . We can thus assume the validity of the continuum hypothesis.

There are two ways to describe the continuum fields: the Eulerian field description and the Lagrangian field description. In this thesis we use the Eulerian field description which focuses on the motion of the fluid through fixed spatial locations. The continuum fields are described at a fixed spatial position $\boldsymbol{r}$ at all times t and hence these two variables are independent. We define the value of any field $F(\boldsymbol{r}, t)$ at the spatial point $\boldsymbol{r}$ at time t as an average value in some fluid particle of volume $\Delta V(\boldsymbol{r})$ around $\boldsymbol{r}$,

$$F(\boldsymbol{r}, t) = \left\langle F_{\text{mol}}(\boldsymbol{r'}, t) \right\rangle_{\boldsymbol{r'} \in \Delta V(\boldsymbol{r})} . \tag{B.1}$$

The volume $\Delta V(\boldsymbol{r})$ is sufficiently large that it contains an enormous number of molecules, which ensures that molecular fluctuations will not affect the observed average value. On the other hand, $\Delta V(\boldsymbol{r})$ has to be sufficiently small that the value is indeed a local average. If it is too big, external forces vary over the spatial distribution of the fluid particle and the average becomes macroscopic.

Let m_i and $\boldsymbol{v}_i$ denote the mass and velocity of the i'th molecule and let $i \in \Delta V$ denote all molecules contained in $\Delta V(\boldsymbol{r})$ at time t. Then, we define the mass density $\rho(\boldsymbol{r}, t)$ and

the velocity field $\boldsymbol{v}(\boldsymbol{r},t)$ as

$$\rho(\boldsymbol{r},t) \equiv \frac{1}{\Delta V}\sum_{i\in\Delta V} m_i, \tag{B.2a}$$

$$\boldsymbol{v}(\boldsymbol{r},t) \equiv \frac{1}{\rho(\boldsymbol{r},t)\Delta V}\sum_{i\in\Delta V} m_i\boldsymbol{v}_i. \tag{B.2b}$$

Notice how the velocity field is defined by the momentum density and not simply as the sum of the molecular velocities in the fluid particle.

B.2 Mathematial notation

In order to simplify the mathematical treatment of the acoustofluidic subjects in the following chapters we shall adopt the notation used by Bruus [40]. Although we shall also use cylindrical and spherical co-ordinates, a Cartesian co-ordinate system is used here for clarity. In a Cartesian co-ordinate system a vector $\boldsymbol{v}$ is written as

$$\boldsymbol{v} = (v_x, v_y, v_z) = v_x\boldsymbol{e}_x + v_y\boldsymbol{e}_y + v_z\boldsymbol{e}_z = \sum_{i=x,y,z} v_i\boldsymbol{e}_i \equiv v_i\boldsymbol{e}_i. \tag{B.3}$$

Here (v_x, v_y, v_z) are the x, y and z co-ordinates of $\boldsymbol{v}$, and $\boldsymbol{e}_x$, $\boldsymbol{e}_y$ and $\boldsymbol{e}_z$ are the corresponding orthonormal basis vectors. In the last expression we have used Einstein's summation convention that repeated indices are implicitly summed over. In this simplifying notation an index can appear at most twice in any term and non-repeated indices must be the same in all terms. In Cartesian co-ordinates it is understood that the summation is over $i = x$, y, z as in Eq. (B.3).

As a compact notation for partial derivatives we write

$$\partial_x v \equiv \frac{\partial v}{\partial x}. \tag{B.4}$$

With this notation we can write the vector differential operator $\boldsymbol{\nabla}$ in Cartesian co-ordinates as

$$\boldsymbol{\nabla} \equiv \boldsymbol{e}_x\partial_x + \boldsymbol{e}_y\partial_y + \boldsymbol{e}_y\partial_y = \boldsymbol{e}_i\partial_i. \tag{B.5}$$

Two other important quantities, the divergence $\boldsymbol{\nabla}\cdot\boldsymbol{v}$ and the Laplacian $\nabla^2\boldsymbol{v}$ of a vector $\boldsymbol{v}$, can in Cartesian co-ordinates be written as

$$\boldsymbol{\nabla}\cdot\boldsymbol{v} \equiv \partial_x v_x + \partial_y v_y + \partial_z v_z \qquad = \partial_i v_i, \tag{B.6a}$$

$$\boldsymbol{\nabla}\cdot\boldsymbol{\nabla}\boldsymbol{v} \equiv \nabla^2\boldsymbol{v} \equiv \boldsymbol{e}_x\partial_x^2 v_x + \boldsymbol{e}_y\partial_y^2 v_y + \boldsymbol{e}_z\partial_z^2 v_z = \partial_i\partial_i v_j. \tag{B.6b}$$

Another symbol we shall use with the index notation is the Kronecker delta δ_{ij},

$$\delta_{ij} \equiv \begin{cases} 1, & \text{for } i = j, \\ 0, & \text{for } i \neq j. \end{cases} \tag{B.7}$$

When treating integrals we shall often apply the divergence theorem which states that the volume integral of the divergence of any vector field $\boldsymbol{v}$ over a region Ω is equal to the integral over the region's surface $\partial\Omega$ of the flux $\boldsymbol{v} \cdot \boldsymbol{n}$ through it,

$$\int_\Omega \boldsymbol{\nabla} \cdot \boldsymbol{v} \, \mathrm{d}\boldsymbol{r} = \oint_{\partial\Omega} \boldsymbol{n} \cdot \boldsymbol{v} \, \mathrm{d}a \qquad \text{or} \qquad \int_\Omega \partial_j v_j \, \mathrm{d}\boldsymbol{r} = \oint_{\partial\Omega} n_j v_j \, \mathrm{d}a \tag{B.8}$$

Here, $\boldsymbol{n}$ is a vector of unit length that is perpendicular to the surface $\partial\Omega$ and points outwards. The 2D and 3D integral measures are denoted $\mathrm{d}a$ and $\mathrm{d}\boldsymbol{r}$, respectively.

Appendix C

Appendix to Chapter 4

C.1 Detailed calculation of the scattered velocity potential

This is a more detailed calculation of the velocity potential scattered by the seed particle, given in Eq. (5.10). The starting point is

$$\phi_{\mathrm{sc}}(r,t) = -f_{1,\mathrm{s}}\frac{a_{\mathrm{s}}^3}{2}\frac{p_{\mathrm{a}}}{\rho_0 c_0}\boldsymbol{\nabla}\cdot\left(\frac{\cos\theta\boldsymbol{e}_r - \sin\theta\boldsymbol{e}_\theta}{r}\right)\cos(\omega t). \tag{C.1}$$

In spherical co-ordinates, the divergence $\boldsymbol{\nabla}\cdot\boldsymbol{v}$ of an azimuthally symmetric vector field $\boldsymbol{v}$ is

$$\boldsymbol{\nabla}\cdot\boldsymbol{v} = \frac{1}{r^2}\,\partial_r\left(r^2 v_r\right) + \frac{1}{r\sin\theta}\,\partial_\theta\left(\sin\theta\, v_\theta\right). \tag{C.2}$$

Setting $\boldsymbol{v} = \dfrac{\cos\theta\boldsymbol{e}_r - \sin\theta\boldsymbol{e}_\theta}{r}$ yields

$$\boldsymbol{\nabla}\cdot\boldsymbol{v} = \frac{1}{r^2}\,\partial_r\left(r^2\,\frac{\cos\theta}{r}\right) + \frac{1}{r\sin\theta}\,\partial_\theta\left(\frac{-\sin^2\theta}{r}\right) \tag{C.3a}$$

$$= \frac{1}{r^2}\,\cos\theta + \frac{1}{r\sin\theta}\,\left(\frac{-\sin\theta\cos\theta}{r}\right) \tag{C.3b}$$

$$= \frac{\cos\theta}{r^2} - \frac{2\cos\theta}{r^2} = -\frac{\cos\theta}{r^2}. \tag{C.3c}$$

Insertion of Eq. (C.3c) into Eq. (C.1) yields the result in Eq. (5.10),

$$\phi_{\mathrm{sc}}(r,t) = f_{1,\mathrm{s}}\frac{a_{\mathrm{s}}^3}{2}\frac{p_{\mathrm{a}}}{\rho_0 c_0}\,\frac{\cos\theta}{r^2}\,\cos(\omega t). \tag{C.4}$$

Appendix D

Appendix to Chapter 5

D.1 Derivation of the scalar equation of motion

The starting point is the rewritten and non-dimensionalised Navier-Stokes equation in Eq. (6.12),

$$\partial_t \boldsymbol{\zeta}' - \boldsymbol{\nabla} \times (\boldsymbol{v}' \times \boldsymbol{\zeta}') = \frac{\varepsilon}{R} \nabla'^2 \boldsymbol{\zeta}', \qquad \varepsilon = \frac{V_0}{\omega a}, \qquad R = \frac{a V_0}{\nu}. \tag{D.1}$$

To proceed further we exploit the symmetry around the z axis which dictates that the physical fields can neither have an azimuthal dependence nor an azimuthal component, thus reducing the problem to a 2D problem. Since the velocity field is divergenceless, we can write the two components in terms of the curl of a scalar function $\psi(r, \theta)$, which we shall refer to as the streaming function,

$$\boldsymbol{v} = \boldsymbol{\nabla} \times \boldsymbol{\xi} = \boldsymbol{\nabla} \times \left[\frac{\psi(r, \theta)}{r \sin \theta} \, \boldsymbol{e}_\phi \right]. \tag{D.2}$$

Taking the curl of a vector that has only an azimuthal component ensures that the velocity field has only a radial and a polar component. The division by $r \sin \theta$ turns out to be convenient. We now wish to calculate the vorticity $\boldsymbol{\zeta}$, its Laplacian $\nabla^2 \boldsymbol{\zeta}$ and the term $\boldsymbol{\nabla} \times (\boldsymbol{v} \times \boldsymbol{\zeta})$ contained in Eq. (D.1) in terms of the streaming function. In order to calculate the vorticity $\boldsymbol{\zeta} = \boldsymbol{\nabla} \times \boldsymbol{v} = \boldsymbol{\nabla} \times \boldsymbol{\nabla} \times \boldsymbol{\xi}$ we use the identity $\boldsymbol{\nabla} \times \boldsymbol{\nabla} \times \boldsymbol{\xi} = \boldsymbol{\nabla}(\boldsymbol{\nabla} \cdot \boldsymbol{\xi}) - \nabla^2 \boldsymbol{\xi}$ to obtain

$$\boldsymbol{\zeta} = \boldsymbol{\nabla}(\boldsymbol{\nabla} \cdot \boldsymbol{\xi}) - \nabla^2 \boldsymbol{\xi}. \tag{D.3}$$

In spherical co-ordinates the divergence is

$$\boldsymbol{\nabla} \cdot \boldsymbol{\xi} = \frac{1}{r^2} \, \partial_r \left(r^2 \xi_r \right) + \frac{1}{r \sin \theta} \, \partial_\theta \left(\sin \theta \, \xi_\theta \right) + \frac{1}{r \sin \theta} \, \partial_\phi \, \xi_\phi = 0, \tag{D.4}$$

where the two first terms are zero since $\boldsymbol{\xi}$ has only an azimuthal component, and the last term is zero due to the azimuthal symmetry. The vorticity $\boldsymbol{\zeta}$ is then given by the Laplacian of $\boldsymbol{\xi}$

$$\boldsymbol{\zeta} = -\nabla^2 \boldsymbol{\xi} = -\nabla^2 \left(\frac{\psi}{r \sin \theta} \, \boldsymbol{e}_\phi \right) \tag{D.5}$$

The three components of the Laplacian are

$$[\nabla^2\boldsymbol{\xi}]_r = \left(\nabla^2 - \frac{2}{r^2}\right)\xi_r - 2\left(\frac{\cot\theta + \partial_\theta}{r^2}\right)\xi_\theta - \frac{2}{r^2\sin\theta}\,\partial_\phi\xi_\phi, \tag{D.6a}$$

$$[\nabla^2\boldsymbol{\xi}]_\theta = \frac{2}{r^2}\,\partial_\theta\xi_r + \left(\nabla^2 - \frac{1}{r^2\sin^2\theta}\right)\xi_\theta - \frac{2\cos\theta}{r^2\sin^2\theta}\,\partial_\phi\xi_\phi, \tag{D.6b}$$

$$[\nabla^2\boldsymbol{\xi}]_\phi = \frac{2}{r^2\sin\theta}\,\partial_\phi\,\xi_r + \frac{2\cos\theta}{r^2\sin^2\theta}\,\partial_\phi\,\xi_\theta + \left(\nabla^2 - \frac{1}{r^2\sin^2\theta}\right)\xi_\phi, \tag{D.6c}$$

where all terms but the last are zero either due to the components being zero or the azimuthal symmetry.

$$[\nabla^2\boldsymbol{\xi}]_\phi = \left(\nabla^2 - \frac{1}{r^2\sin^2\theta}\right)\xi_\phi \tag{D.7a}$$

$$= \frac{1}{r^2}\,\partial_r\left(r^2\,\partial_r\,\xi_\phi\right) + \frac{1}{r^2\sin\theta}\,\partial_\theta\left(\sin\theta\,\partial_\theta\xi_\phi\right) + \frac{1}{r^2\sin^2\theta}\,\overbrace{\partial_\phi^2\,\xi_\phi}^{=0} - \frac{1}{r^2\sin^2\theta}\,\xi_\phi \tag{D.7b}$$

$$= \frac{1}{r^2\sin\theta}\,\partial_r\left(r^2\partial_r\left[\frac{\psi}{r}\right]\right) + \frac{1}{r^3\sin\theta}\partial_\theta\left(\sin\theta\,\partial_\theta\left[\frac{\psi}{\sin\theta}\right]\right) - \frac{\psi}{r^3\sin^3\theta} \tag{D.7c}$$

$$= \frac{1}{r^2\sin\theta}\,\partial_r\left(r\partial_r\psi - \psi\right) + \frac{1}{r^3\sin\theta}\partial_\theta\left(\partial_\theta\psi - \frac{\cos\theta}{\sin\theta}\,\psi\right) - \frac{\psi}{r^3\sin^3\theta} \tag{D.7d}$$

$$= \frac{1}{r\sin\theta}\,\partial_r^2\psi + \frac{1}{r^3\sin\theta}\left(\partial_\theta^2\psi - \frac{\cos\theta}{\sin\theta}\,\partial_\theta\psi + \frac{1}{\sin^2\theta}\,\psi\right) - \frac{\psi}{r^3\sin^3\theta} \tag{D.7e}$$

$$= \frac{1}{r\sin\theta}\left[\partial_r^2\psi + \frac{1}{r^2}\left(\partial_\theta^2\psi - \frac{\cos\theta}{\sin\theta}\partial_\theta\psi\right)\right] \tag{D.7f}$$

Finally, we insert Eq. (D.7f) in Eq. (D.3) and make the transformation $\mu = \cos\theta$ to obtain

$$\boldsymbol{\zeta} = -\frac{\boldsymbol{e}_\phi}{r\sin\theta}\left[\partial_r^2\psi + \frac{1}{r^2}\left((1-\mu^2)^{1/2}\,\partial_\mu\left[(1-\mu^2)^{1/2}\partial_\mu\psi\right] + \mu\partial_\mu\psi\right)\right] \tag{D.8a}$$

$$= -\frac{\boldsymbol{e}_\phi}{r\sin\theta}\left[\partial_r^2\psi + \frac{1}{r^2}\left((1-\mu^2)\,\partial_\mu^2\psi - \mu\partial_\mu\psi + \mu\partial_\mu\psi\right)\right] \tag{D.8b}$$

$$= -\frac{\boldsymbol{e}_\phi}{r\sin\theta}\,D^2\psi, \tag{D.8c}$$

where we in the last expression have introduced the operator D^2,

$$D^2 = \partial_r^2\psi + \frac{1-\mu^2}{r^2}\,\partial_\mu^2. \tag{D.9}$$

In order to calculate the term $\boldsymbol{\nabla}\times(\boldsymbol{v}\times\boldsymbol{\zeta})$ we have to determine the velocity field in terms of the streaming function. Using the definition of the curl in spherical co-ordinates we get

$$\boldsymbol{v} = \boldsymbol{\nabla} \times \boldsymbol{\xi} = \boldsymbol{\nabla} \times \left[\frac{\psi}{r\sin\theta}\,\boldsymbol{e}_\phi\right] = \frac{1}{r^2\sin\theta}\begin{vmatrix} \boldsymbol{e}_r & r\boldsymbol{e}_\theta & r\sin\theta\boldsymbol{e}_\phi \\ \partial_r & \partial_\theta & \partial_\phi \\ \xi_r & r\xi_\theta & r\sin\theta\xi_\phi \end{vmatrix} \tag{D.10a}$$

$$= \frac{1}{r^2\sin\theta}\Bigg[\boldsymbol{e}_r\Big(\partial_\theta[\sin\theta\xi_\phi] - \partial_\phi\xi_\theta\Big) + r\boldsymbol{e}_\theta\Big(\partial_r[r\sin\theta\xi_\phi] - \partial_\phi\xi_r\Big) \tag{D.10b}$$

$$+ r\sin\theta\boldsymbol{e}_\phi\Big(\partial_r[r\xi_\theta] - \partial_\theta\xi_r\Big)\Bigg] \tag{D.10c}$$

$$= \boldsymbol{e}_r\frac{\partial_\theta[\sin\theta\xi_\phi]}{r\sin\theta} - \boldsymbol{e}_\theta\frac{\partial_r[r\xi_\phi]}{r} = \boldsymbol{e}_r\frac{1}{r^2\sin\theta}\partial_\theta\psi - \boldsymbol{e}_\theta\frac{1}{r\sin\theta}\partial_r\psi \tag{D.10d}$$

$$= -\boldsymbol{e}_r\frac{\partial_\mu\psi}{r^2} - \boldsymbol{e}_\theta\frac{\partial_r\psi}{r(1-\mu^2)}. \tag{D.10e}$$

The next step is the calculation of the cross product $\boldsymbol{v}\times\boldsymbol{\zeta}$ which we determine from Eqs. (D.8c) and (D.10e) and the definition of a cross product in spherical co-ordinates,

$$\boldsymbol{v}\times\boldsymbol{\zeta} = \begin{vmatrix} \boldsymbol{e}_r & \boldsymbol{e}_\theta & \boldsymbol{e}_\phi \\ v_r & v_\theta & v_\phi \\ \zeta_r & \zeta_\theta & \zeta_\phi \end{vmatrix} = \boldsymbol{e}_r(v_\theta\zeta_\phi - v_\phi\zeta_\theta) + \boldsymbol{e}_\theta(v_r\zeta_\phi - v_\phi\zeta_r) + \boldsymbol{e}_\phi(v_r\zeta_\theta - v_\theta\zeta_r) \tag{D.11a}$$

$$= \boldsymbol{e}_r v_\theta\zeta_\phi - \boldsymbol{e}_\theta v_r\zeta_\phi = \boldsymbol{e}_r\frac{(\partial_r\psi)(D^2\psi)}{r^2\sin^2\theta} + \boldsymbol{e}_\theta\frac{(\partial_\theta\psi)(D^2\psi)}{r^3\sin^2\theta}. \tag{D.11b}$$

Evidently, we drop the terms containing v_ϕ, ζ_r and ζ_θ as these are zero. Finally, we can calculate the entire term. Once again using the definition of the curl in spherical co-ordinates, we get

$$\boldsymbol{\nabla}\times(\boldsymbol{v}\times\boldsymbol{\zeta}) = \frac{1}{r^2\sin\theta}\begin{vmatrix} \boldsymbol{e}_r & r\boldsymbol{e}_\theta & r\sin\theta\boldsymbol{e}_\phi \\ \partial_r & \partial_\theta & \partial_\phi \\ [\boldsymbol{v}\times\boldsymbol{\zeta}]_r & r[\boldsymbol{v}\times\boldsymbol{\zeta}]_\theta & r\sin\theta[\boldsymbol{v}\times\boldsymbol{\zeta}]_\phi \end{vmatrix} \tag{D.12a}$$

$$= \frac{1}{r^2\sin\theta}\Bigg\{ \boldsymbol{e}_r\Big[\partial_\theta\Big(r\sin\theta[\boldsymbol{v}\times\boldsymbol{\zeta}]_\phi\Big) - \partial_\phi\Big(r[\boldsymbol{v}\times\boldsymbol{\zeta}]_\theta\Big)\Big] + \tag{D.12b}$$

$$r\boldsymbol{e}_\theta\Big[\partial_r\Big(r\sin\theta[\boldsymbol{v}\times\boldsymbol{\zeta}]_\phi\Big) - \partial_\phi\Big([\boldsymbol{v}\times\boldsymbol{\zeta}]_r\Big)\Big] + \tag{D.12c}$$

$$r\sin\theta\boldsymbol{e}_\phi\Big[\partial_r\Big(r[\boldsymbol{v}\times\boldsymbol{\zeta}]_\theta\Big) - \partial_\theta\Big([\boldsymbol{v}\times\boldsymbol{\zeta}]_r\Big)\Big]\Bigg\}. \tag{D.12d}$$

Only the radial and polar components of $\boldsymbol{v} \times \boldsymbol{\zeta}$ are non-zero and they do not depend on the azimuthal angle ϕ which leaves

$$\boldsymbol{\nabla} \times (\boldsymbol{v} \times \zeta) = \frac{1}{r}\boldsymbol{e}_\phi \left[\partial_r(r[\boldsymbol{v} \times \boldsymbol{\zeta}]_\theta) - \partial_\theta[\boldsymbol{v} \times \zeta]\right] \tag{D.13a}$$

$$= \frac{1}{r}\boldsymbol{e}_\phi \left[\partial_r\left(\frac{(\partial_\theta\psi)(D^2\psi)}{r^2\sin^2\theta}\right) - \partial_\theta\left(\frac{(\partial_r\psi)(D^2\psi)}{r^2\sin^2\theta}\right)\right] \tag{D.13b}$$

$$= \frac{1}{r}\boldsymbol{e}_\phi \Bigg[- \frac{2(\partial_\theta\psi)(D^2\psi)}{r^3\sin^2\theta} + \frac{\partial_r\big[(\partial_\theta\psi)(D^2\psi)\big]}{r^2\sin^2\theta} \tag{D.13c}$$

$$+ \frac{2\cos\theta\,(\partial_r\psi)(D^2\psi)}{r^2\sin^3\theta} - \frac{\partial_\theta\big[(\partial_r\psi)(D^2\psi)\big]}{r^2\sin^2\theta}\Bigg] \tag{D.13d}$$

$$= \frac{\boldsymbol{e}_\phi}{r^3\sin\theta}\Bigg[\frac{2}{r}(\partial_\mu\psi)(D^2\psi) - \partial_r\big[(\partial_\mu\psi)(D^2\psi)\big] \tag{D.13e}$$

$$+ \frac{2\mu}{1-\mu^2}(\partial_r\psi)(D^2\psi) + \partial_\mu\big[(\partial_r\psi)(D^2\psi)\big]\Bigg] \tag{D.13f}$$

$$= \frac{\boldsymbol{e}_\phi}{r^3\sin\theta}\Bigg[\frac{2}{r}(\partial_\mu\psi)(D^2\psi) - (\partial_\mu\psi)\,\partial_r(D^2\psi) \tag{D.13g}$$

$$+ \frac{2\mu}{1-\mu^2}(\partial_r\psi)(D^2\psi) + (\partial_r\psi)\,\partial_\mu(D^2\psi)\Bigg] \tag{D.13h}$$

In Eq. (D.13b) we insert the components from Eq. (D.11b) and in Eqs. (D.13e) and (D.13f) we transform the angular co-ordinate $\mu = \cos\theta$. Finally, we write the result more compactly as

$$\boldsymbol{\nabla} \times (\boldsymbol{v} \times \boldsymbol{\zeta}) = \frac{\boldsymbol{e}_\phi}{r\sin\theta}\left[\frac{1}{r^2}\frac{\partial\big(\psi, D^2\psi\big)}{\partial(r,\mu)} + \frac{2}{r^2}(D^2\psi)(L\psi)\right], \tag{D.14}$$

where we have introduced the operators

$$\frac{\partial\big(P,Q\big)}{\partial(x,y)} = (\partial_x P)(\partial_y Q) - (\partial_y P)(\partial_x Q), \qquad L = \frac{\mu}{1-\mu^2}\,\partial_r + \frac{1}{r}\,\partial_\mu. \tag{D.15}$$

We saw in Eqs. (D.5) and (D.8) that the vorticity could be expressed as minus the Laplacian of the function $\boldsymbol{\xi}$,

$$\boldsymbol{\zeta} = -\nabla^2\boldsymbol{\xi} = -\nabla^2\left(\frac{\psi}{r\sin\theta}\,\boldsymbol{e}_\phi\right) = -\frac{D^2\psi}{r\sin\theta}\,\boldsymbol{e}_\phi, \tag{D.16}$$

where the last expression was the result. When calculating the term $\nabla^2\boldsymbol{\zeta}$ in Eq. (D.1) we notice the similarity between $\boldsymbol{\xi}$ and $\boldsymbol{\zeta}$ in Eq. (D.16) and immediately see that the result must be

$$\nabla^2\boldsymbol{\zeta} = -\nabla^2\left(\frac{D^2\psi}{r\sin\theta}\,\boldsymbol{e}_\phi\right) = -\frac{D^2(D^2\psi)}{r\sin\theta}\,\boldsymbol{e}_\phi. \tag{D.17}$$

When the terms in Eqs. (D.14), (D.16) and (D.17) are inserted into the non-dimensionalised Navier-Stokes equation, we obtain, after multiplication by $-(r\sin\theta)$, a scalar equation for the streaming function,

$$\partial_t(D^2\psi) + \varepsilon\left[\frac{1}{r^2}\frac{\partial(\psi, D^2\psi)}{\partial(r,\mu)} + \frac{2}{r^2}(D^2\psi)(L\psi)\right] = \frac{1}{|M|^2}D^4\psi, \tag{D.18}$$

where the operators are

$$D^2 = \partial_r^2 + \frac{1-\mu^2}{r^2}\,\partial_\mu^2, \qquad D^4 = D^2D^2, \qquad L = \frac{\mu}{1-\mu^2}\,\partial_r + \frac{1}{r}\,\partial_\mu, \tag{D.19}$$

and

$$\frac{\partial(P,Q)}{\partial(x,y)} = (\partial_x P)(\partial_y Q) - (\partial_y P)(\partial_x Q). \tag{D.20}$$

Eq. (D.43) is equation of motion formulated in terms of the streaming function in a scalar equation. The price paid for reducing the vector equation to the scalar equation is the latter's higher order.

D.2 Exact first-order solution of streaming equation

To first order the streaming equation in non-dimensionalised co-ordinates is

$$\partial_t(D^2\psi_1) = \frac{1}{|M|^2}D^4\psi_1, \tag{D.21}$$

and has the boundary conditions

$$\psi_1 = 0 \qquad \text{at} \quad r = 1, \tag{D.22a}$$

$$\partial_r\psi_1 = 0 \qquad \text{at} \quad r = 1, \tag{D.22b}$$

$$\psi_1 \to \tfrac{1}{2}v_{\mathrm{a}}r^2\big(1-\mu^2\big) \qquad \text{as} \quad r \to \infty, \tag{D.22c}$$

We recall that we assume a harmonic time dependence of the fields which means that in dimensionalised co-ordinates, the time derivative yields a factor $\mathrm{i}\omega$, corresponding to a factor i in the non-dimensionalised ones. As we from the definition of the boundary number, Eq. (6.2a), have that $\mathrm{i}|M|^2 = M^2$, we can rewrite Eq. (D.21) as

$$M^2D^2\psi_1 = D^4\psi_1. \tag{D.23}$$

The far-field condition Eq. (D.22c) calls for a separation of variables,

$$\psi_1(r,\mu) = R_1(r)\big(1-\mu^2\big). \tag{D.24}$$

We then get

$$D^2\psi_1 = \partial_r^2\psi_1 + \frac{1-\mu^2}{r^2}\,\partial_\mu^2\psi_1 = \big(1-\mu^2\big)\left[\partial_r^2R_1 - \frac{2}{r^2}R_1\right]. \tag{D.25}$$

Next, we use this result for the higher-order derivative

$$D^4\psi_1 = D^2\big(D^2\psi_1\big) = \left[\partial_r^2 + \frac{1-\mu^2}{r^2}\,\partial_\mu^2\right]\left[\big(1-\mu^2\big)\partial_r^2 R_1 - \frac{2}{r^2}\big(1-\mu^2\big)R_1\right] \tag{D.26a}$$

$$= \big(1-\mu^2\big)\left[\partial_r^4 R_1 - \frac{4}{r^2}\,\partial_r^2 R + \frac{8}{r^3}\,\partial_r R - \frac{8}{r^4}\,R\right]. \tag{D.26b}$$

Insertion of Eqs. (D.25) and (D.26b) into Eq. (D.23) yields an ordinary differential equation,

$$\partial_r^4 R_1 - \left(M^2 + \frac{4}{r^2}\right)\partial_r^2 R + \frac{8}{r^3}\,\partial_r R + \left(\frac{2M^2}{r^2} - \frac{8}{r^4}\right)R. \tag{D.27}$$

By direct insertion, it can be verified that Eq. (D.27) has the solution

$$R(r) = \frac{k_\mathrm{I}}{r} + k_\mathrm{II}\,\frac{r^3-1}{3r} + \frac{k_\mathrm{III}}{M^3}\left[\frac{\cosh(Mr)}{Mr} - \sinh(Mr)\right] + \frac{\mathrm{i}k_\mathrm{IV}}{M^3}\left[\cosh(Mr) - \frac{\sinh(Mr)}{Mr}\right]. \tag{D.28}$$

As the terms in the square brackets explode for $r \to \infty$, the far-field condition in Eq. (D.22c) leads to $k_\mathrm{III} = -\,\mathrm{i}k_\mathrm{IV}$ and $k_\mathrm{II} = \frac{3}{2}$. Insertion of this into Eq. (D.28) and use of the identity $\cosh(Mr) - \sinh(Mr) = \exp(-Mr)$ yields

$$R(r) = \frac{1}{2}r^2 - \left[\frac{1}{2} - k_\mathrm{I}\right]\frac{1}{r} + \frac{\mathrm{i}k_\mathrm{IV}}{M^3}\left[1 + \frac{1}{Mr}\right]\mathrm{e}^{-Mr}. \tag{D.29}$$

In order to apply the condition in Eq. (D.22b) we calculate the derivative of $R(r)$,

$$\partial_r R = r + \left[\frac{1}{2} - k_\mathrm{I}\right]\frac{1}{r^2} + \frac{\mathrm{i}k_\mathrm{IV}}{M^3}\left[-M - \frac{1}{r} - \frac{1}{Mr^2}\right]\mathrm{e}^{-Mr}. \tag{D.30}$$

The two remaining boundary conditions in Eqs. (D.22a) and (D.22b) are

$$k_\mathrm{I} + \frac{\mathrm{i}k_\mathrm{IV}}{M^3}\left[1 + \frac{1}{M}\right]\mathrm{e}^{-M} = 0, \tag{D.31a}$$

$$\frac{3}{2} - k_\mathrm{I} + \frac{\mathrm{i}k_\mathrm{IV}}{M^3}\left[-M - 1 - \frac{1}{M}\right]\mathrm{e}^{-M} = 0. \tag{D.31b}$$

$$\tag{D.31c}$$

The conditions in Eq. (D.31) can be formulated as a matrix equation,

$$\begin{bmatrix} 1 & \frac{\mathrm{i}}{M^3}\left[1 + \frac{1}{M}\right]\mathrm{e}^{-M} \\ -1 & \frac{\mathrm{i}}{M^3}\left[-1 - M - \frac{1}{M}\right]\mathrm{e}^{-M} \end{bmatrix}\begin{bmatrix} k_\mathrm{I} \\ k_\mathrm{IV} \end{bmatrix} = \begin{bmatrix} 0 \\ -\frac{3}{2} \end{bmatrix}. \tag{D.32}$$

The determinant D of the coefficient matrix is

$$D = \begin{vmatrix} 1 & \frac{\mathrm{i}}{M^3}\left[1 + \frac{1}{M}\right]\mathrm{e}^{-M} \\ -1 & \frac{\mathrm{i}}{M^3}\left[-1 - M - \frac{1}{M}\right]\mathrm{e}^{-M} \end{vmatrix} \tag{D.33a}$$

$$= \frac{\mathrm{i}}{M^3}\left[-1 - M - \frac{1}{M} + 1 + \frac{1}{M}\right]\mathrm{e}^{-M} = -\frac{\mathrm{i}}{M^3}\,\mathrm{e}^{-M}. \tag{D.33b}$$

Then the coefficients are

$$k_{\mathrm{I}} = \frac{1}{D}\begin{vmatrix} 0 & \frac{\mathrm{i}}{M^3}\left[1+\frac{1}{M}\right]\mathrm{e}^{-M} \\ -\frac{3}{2} & \frac{\mathrm{i}}{M^3}\left[-1-M-\frac{1}{M}\right]\mathrm{e}^{-M} \end{vmatrix} \tag{D.34a}$$

$$= \mathrm{i}M^2\,\mathrm{e}^{M}\begin{vmatrix} 0 & \frac{\mathrm{i}}{M^3}\left[1+\frac{1}{M}\right]\mathrm{e}^{-M} \\ -\frac{3}{2} & \frac{\mathrm{i}}{M^3}\left[-1-M-\frac{1}{M}\right]\mathrm{e}^{-M} \end{vmatrix} = -\frac{3M+3}{2M^2}, \tag{D.34b}$$

and

$$k_{\mathrm{IV}} = \frac{1}{D}\begin{vmatrix} 1 & 0 \\ -1 & -\frac{3}{2} \end{vmatrix} = \mathrm{i}M^2\,\mathrm{e}^{M}\begin{vmatrix} 1 & 0 \\ -1 & -\frac{3}{2} \end{vmatrix} = -\frac{3\,\mathrm{i}M^2}{2}\,\mathrm{e}^{M}. \tag{D.35}$$

Insertion of Eqs. (D.34) and (D.35) into Eq. (D.29) and a subsequent insertion into Eq. (D.24) yields the exact first-order solution to the streaming equation,

$$\psi_1(r,\mu) = \left[\frac{1}{2}r^2 - \left(\frac{M^2+3M+3}{2M^2}\right)\frac{1}{r} + \frac{3}{2M}\left(1+\frac{1}{Mr}\right)\mathrm{e}^{M(1-r)}\right]\left(1-\mu^2\right). \tag{D.36}$$

We recall that $|M| \gg 1$ and that r is measured in units of the sphere radius. Thus, the real part of argument of the exponential function becomes a very high negative number at the edge of the boundary layer region where $r \approx 1+5\frac{\delta}{a}$ (which is $a+5\delta$ in dimensionalised co-ordinates). This means that the term containing the exponential function decays with a characteristic length of δ which is why we call this length the boundary layer thickness. For $r \gg \delta$ the term is virtually zero and if we also approximate the second term with $|M| \gg 1$, we arrive at the outer first-order solution given in Eq. (6.46b),

$$\psi_1(r,\mu) \approx \frac{1}{2}\left(r^2 - \frac{1}{r}\right)\left(1-\mu^2\right), \qquad \text{for} \qquad |M| \gg 1 \qquad \text{and} \qquad r \gtrapprox 1+5\frac{\delta}{a}. \tag{D.37}$$

The inner radial co-ordinate $\eta = \frac{|M|}{\sqrt{2}}(r-1)$ can be rewritten as $r = 1+\frac{\sqrt{2}\eta}{|M|}$ which if inserted into Eq. (D.36) yields

$$\psi_1(r,\mu) = \left[\frac{1}{2}\left(1+\frac{\sqrt{2}\eta}{|M|}\right)^2 - \left(\frac{M^2+3M+3}{2M^2}\right)\left(1+\frac{\sqrt{2}\eta}{|M|}\right)^{-1}\right. \tag{D.38a}$$

$$\left. + \frac{3}{2M}\left(1+\frac{1}{M}\left[1+\frac{\sqrt{2}\eta}{|M|}\right]^{-1}\right)\mathrm{e}^{-\sqrt{2}\frac{M}{|M|}\eta}\right]\left(1-\mu^2\right). \tag{D.38b}$$

As $\frac{\sqrt{2}\eta}{|M|} = r-1 \ll 1$ close to the sphere surface and the boundary layer, we can make Taylor expansions to first order,

$$\psi_1(r,\mu) \approx \left[\frac{1}{2}\left(1+2\frac{\sqrt{2}\eta}{|M|}\right) - \left(\frac{M^2+3M+3}{2M^2}\right)\left(1-\frac{\sqrt{2}\eta}{|M|}\right)\right. \tag{D.39a}$$

$$\left. + \frac{3}{2M}\left(1+\frac{1}{M}\left[1-\frac{\sqrt{2}\eta}{|M|}\right]\right)\mathrm{e}^{-\sqrt{2}\frac{M}{|M|}\eta}\right]\left(1-\mu^2\right). \tag{D.39b}$$

Neglecting terms of order $|M|^{-2}$ or higher yields

$$\psi_1(r,\mu) \approx \left[\frac{1}{2} + \frac{\sqrt{2}\eta}{|M|} - \frac{1}{2} - \frac{3}{2M} + \frac{\sqrt{2}\eta}{2|M|} + \frac{3}{2M}\,\mathrm{e}^{-\sqrt{2}\frac{M}{|M|}\eta}\right]\left(1-\mu^2\right) \tag{D.40a}$$

$$= \left[\frac{3\sqrt{2}\eta}{2|M|} - \frac{3}{2M} + \frac{3}{2M}\,\mathrm{e}^{-\sqrt{2}\frac{M}{|M|}\eta}\right]\left(1-\mu^2\right) \tag{D.40b}$$

$$= \frac{\sqrt{2}}{|M|}\frac{3}{2}\left[\eta - \frac{|M|}{\sqrt{2}M} + \frac{|M|}{\sqrt{2}M}\,\mathrm{e}^{-\sqrt{2}\frac{M}{|M|}\eta}\right]\left(1-\mu^2\right). \tag{D.40c}$$

From the definition of the boundary layer number, we have that $\mathrm{i}|M|^2 = M^2$ or equivalently $M = \frac{1+\mathrm{i}}{\sqrt{2}}|M|$ which we can rewrite as $\frac{|M|}{\sqrt{2}M} = \frac{1}{2}(1-\mathrm{i})$. Insertion of the last expression into Eq. (D.40c) yields

$$\psi_1(r,\mu) = \frac{\sqrt{2}}{|M|}\frac{3}{2}\left[\eta - \frac{1}{2}(1-\mathrm{i})\left(1-\mathrm{e}^{-(1+\mathrm{i})\eta}\right)\right]\left(1-\mu^2\right). \tag{D.41a}$$

Finally, multiplying by $\frac{|M|}{\sqrt{2}}$ to get

$$\frac{|M|}{\sqrt{2}}\psi_1(r,\mu) = \frac{3}{2}\left[\eta - \frac{1}{2}(1-\mathrm{i})\left(1-\mathrm{e}^{-(1+\mathrm{i})\eta}\right)\right]\left(1-\mu^2\right) \tag{D.42a}$$

we recognise the inner first-order solution given in Eq. (6.46a).

D.3 Transformation of the streaming equation to inner co-ordinates

In this section we transform the equation

$$\partial_t(D^2\psi) \;+\varepsilon\left[-\frac{1}{r^2}\frac{\partial(\psi,D^2\psi)}{\partial(r,\mu)} + \frac{2}{r^2}(D^2\psi)(L\psi)\right] \;=\; \frac{1}{|M|^2}D^4\psi, \tag{D.43}$$

to be formulated in terms of the inner radial co-ordinate η and the inner streaming function Ψ,

$$\eta = \frac{|M|}{\sqrt{2}}\,(r-1), \qquad \Psi = \frac{|M|}{\sqrt{2}}\psi. \tag{D.44}$$

As $\frac{|M|}{\sqrt{2}}$ is a constant, we see in Eq. (D.44) that

$$\partial_r\psi = \frac{\partial\psi}{\partial r} = \frac{\partial\eta}{\partial r}\frac{\partial\psi}{\partial\eta} = \frac{|M|}{\sqrt{2}}\frac{\partial\psi}{\partial\eta} = \frac{\partial\Psi}{\partial\eta} = \partial_\eta\Psi, \tag{D.45a}$$

$$\partial_r^2\psi = \frac{\partial(\partial_\eta\Psi)}{\partial r} = \frac{\partial\eta}{\partial r}\frac{\partial(\partial_\eta\Psi)}{\partial\eta} = \frac{|M|}{\sqrt{2}}\,\partial_\eta^2\Psi. \tag{D.45b}$$

With the results in Eq. (D.45) we can write

$$D^2\psi = \partial_r^2\psi + \frac{1-\mu^2}{r^2}\,\partial_\mu^2\psi = \frac{|M|}{\sqrt{2}}\partial_\eta^2\Psi + \frac{1-\mu^2}{r^2}\,\frac{\sqrt{2}}{|M|}\partial_\mu^2\Psi. \tag{D.46}$$

If we express r in terms of η we get

$$D^2\psi = \frac{|M|}{\sqrt{2}}\partial_\eta^2\Psi + \left(1-\mu^2\right)\left(1+\frac{\sqrt{2}\eta}{|M|}\right)^{-2}\frac{\sqrt{2}}{|M|}\partial_\mu^2\Psi \tag{D.47a}$$

$$\approx \frac{|M|}{\sqrt{2}}\partial_\eta^2\Psi + \left(1-\mu^2\right)\left(1-2\frac{\sqrt{2}\eta}{|M|}\right)\frac{\sqrt{2}}{|M|}\partial_\mu^2\Psi. \tag{D.47b}$$

To obtain the last expression we have made a Taylor expansion of $\left(1+\frac{\sqrt{2}\eta}{|M|}\right)^{-2}$ to first order in $\frac{\sqrt{2}\eta}{|M|} \ll 1$. To see if the expansion is justified we express η in terms of r using Eq. (D.44). The inequality then becomes

$$\frac{\sqrt{2}\eta}{|M|} = \frac{\sqrt{2}}{|M|}\frac{|M|}{\sqrt{2}}(r-1) = r-1 \ll 1, \tag{D.48}$$

We know see that the Taylor expansion is justified for $r \ll 2$ where we recall that r is measured in units of the sphere radius a. Thus, close to the sphere and thereby also the boundary layer, the Taylor expansion is justified. Returning to Eq. (D.47b), we recall that the transformation of the radial derivative can be considered a normalisation. By that we mean that the derivatives are now of the same order of magnitude close to the boundary layer, $\partial_\eta\Psi \sim \partial_\mu\Psi$. Thus, to leading order in $|M|$ we obtain

$$D^2\psi \approx \frac{|M|}{\sqrt{2}}\partial_\eta^2\Psi. \tag{D.49}$$

The next derivative in Eq. (D.43) can be transformed using Eqs. (D.44), (D.45a) and (D.49),

$$\frac{\partial(\psi, D^2\psi)}{\partial(r,\mu)} = \big(\partial_r\psi\big)\partial_\mu\big(D^2\psi\big) - \big(\partial_\mu\psi\big)\partial_r\big(D^2\psi\big) \tag{D.50a}$$

$$= \big(\partial_\eta\Psi\big)\partial_\mu\left(\frac{|M|}{\sqrt{2}}\partial_\eta^2\Psi\right) - \left(\partial_\mu\frac{\sqrt{2}}{|M|}\Psi\right)\frac{|M|}{\sqrt{2}}\partial_\eta\left(\frac{|M|}{\sqrt{2}}\partial_\eta^2\Psi\right) \tag{D.50b}$$

$$= \frac{|M|}{\sqrt{2}}\frac{\partial(\Psi, \partial_\eta^2\Psi)}{\partial(\eta,\mu)}. \tag{D.50c}$$

We move on to the transformation of the derivative $L\psi$ where we Taylor expand as in Eq. (D.47b) and subsequently keep only terms of leading order in $|M|$,

$$L\psi = \frac{\mu}{1-\mu^2}\,\partial_r\psi + \frac{1}{r}\,\partial_\mu\psi = \frac{\mu}{1-\mu^2}\,\partial_\eta\Psi + \left(1+\frac{\sqrt{2}\eta}{|M|}\right)^{-1}\partial_\mu\left(\frac{\sqrt{2}}{|M|}\Psi\right) \tag{D.51a}$$

$$\approx \frac{\mu}{1-\mu^2}\,\partial_\eta\Psi + \left(1-\frac{\sqrt{2}\eta}{|M|}\right)\partial_\mu\left(\frac{\sqrt{2}}{|M|}\Psi\right) \approx \frac{\mu}{1-\mu^2}\,\partial_\eta\Psi. \tag{D.51b}$$

The transformed product term $(D^2\psi)(L\psi)$ is given by Eqs. (D.49) and (D.51),

$$\big(D^2\psi\big)\big(L\psi\big) = \frac{|M|}{\sqrt{2}}\frac{\mu}{1-\mu^2}\big(\partial_\eta^2\Psi\big)\big(\partial_\eta\Psi\big). \tag{D.52}$$

Finally, we can determine the derivative on the right hand side of Eq. (D.43). The easiest way to do that is by inspection of Eq. (D.49) which states that $D^2\psi = \frac{|M|}{\sqrt{2}}\,\partial_\eta^2\Psi$. Going back to the outer streaming function we then have $D^2\psi = \frac{|M|^2}{2}\,\partial_\eta^2\psi$ which states that $D^2 = \frac{|M|^2}{2}\,\partial_\eta^2$. For the fourth-order differential operator we thus obtain

$$D^4\psi = D^2\big(D^2\psi\big) = D^2\left(\frac{|M|}{\sqrt{2}}\partial_\eta^2\Psi\right) = \frac{|M|^2}{2}\,\partial_\eta^2\left(\frac{|M|}{\sqrt{2}}\partial_\eta^2\Psi\right) = \frac{|M|^3}{2\sqrt{2}}\partial_\eta^4\Psi. \tag{D.53}$$

When inserting Eqs. (D.49), (D.50), (D.52) and (D.53) into Eq. (D.43), the factors $\frac{|M|}{\sqrt{2}}$ in each term can be multiplied away to obtain

$$\partial_t\big(\partial_\eta^2\psi\big) + \frac{\varepsilon}{r^2}\left[\frac{\partial\big(\Psi,\partial_\eta^2\Psi\big)}{\partial(\eta,\mu)} + \frac{2\mu}{1-\mu^2}\big(\partial_\eta\Psi\big)\big(\partial_\eta^2\Psi\big)\right] = \frac{1}{2}\partial_\eta^4\Psi. \tag{D.54}$$

As we have seen earlier, the factor r^{-2} can be Taylor expanded close to the boundary,

$$\frac{1}{r^2} = \left(1+\frac{\sqrt{2}\eta}{|M|}\right)^{-2} \approx 1 - 2\frac{\sqrt{2}\eta}{|M|}. \tag{D.55}$$

After insertion of Eq. (D.55) into Eq. (D.54), we have to leading order in $|M|$ the inner, non-dimensionalised equation of motion,

$$\partial_t\big(\partial_\eta^2\psi\big) + \varepsilon\left[\frac{\partial\big(\Psi,\partial_\eta^2\Psi\big)}{\partial(\eta,\mu)} + \frac{2\mu}{1-\mu^2}\big(\partial_\eta\Psi\big)\big(\partial_\eta^2\Psi\big)\right] = \frac{1}{2}\partial_\eta^4\Psi. \tag{D.56}$$

This is the equation that we present in Eq. (6.26).

D.4 Details in the first-order asymptotic matching

In this section we fill in the details in first-order asymptotic matching leading to the determination of the coefficients c_{II} and C_{II}. Our starting point is the equations

$$(1+\mathrm{i})C_{\mathrm{II}} = 1 - c_{\mathrm{II}}, \tag{D.57a}$$

$$C_{\mathrm{II}} = -\frac{|M|}{\sqrt{2}}\big(c_{\mathrm{II}} + \tfrac{1}{2}\big), \tag{D.57b}$$

which we can write as the matrix equation

$$\begin{bmatrix} 1 & 1+\mathrm{i} \\ \frac{|M|}{\sqrt{2}} & 1 \end{bmatrix}\begin{bmatrix} c_{\mathrm{II}} \\ C_{\mathrm{II}} \end{bmatrix} = \begin{bmatrix} 1 \\ -\frac{|M|}{2\sqrt{2}} \end{bmatrix}. \tag{D.58}$$

The determinant D of the coefficient matrix is

$$D = \begin{vmatrix} 1 & 1+\mathrm{i} \\ \frac{|M|}{\sqrt{2}} & 1 \end{vmatrix} = 1 - \frac{|M|}{\sqrt{2}}(1+\mathrm{i}). \tag{D.59a}$$

Then the coefficients are

$$c_{\mathrm{II}} = \frac{1}{D} \begin{vmatrix} 1 & 1+\mathrm{i} \\ -\frac{|M|}{2\sqrt{2}} & 1 \end{vmatrix} = \frac{1}{1-\frac{|M|}{\sqrt{2}}(1+\mathrm{i})} \begin{vmatrix} 1 & 1+\mathrm{i} \\ -\frac{|M|}{2\sqrt{2}} & 1 \end{vmatrix} = \frac{1+\frac{|M|}{2\sqrt{2}}(1+\mathrm{i})}{1-\frac{|M|}{\sqrt{2}}(1+\mathrm{i})} \tag{D.60a}$$

$$= \frac{-\frac{|M|}{2\sqrt{2}}(1+\mathrm{i})-1}{\frac{|M|}{\sqrt{2}}(1+\mathrm{i})-1} = -\frac{1}{2}\frac{|M|(1+\mathrm{i})+2\sqrt{2}}{|M|(1+\mathrm{i})-\sqrt{2}} \approx -\frac{1}{2} \qquad \text{for} \qquad |M| \gg 1, \tag{D.60b}$$

and

$$C_{\mathrm{II}} = \frac{1}{D} \begin{vmatrix} 1 & 1 \\ \frac{|M|}{\sqrt{2}} & -\frac{|M|}{2\sqrt{2}} \end{vmatrix} = \frac{1}{1-\frac{|M|}{\sqrt{2}}(1+\mathrm{i})} \begin{vmatrix} 1 & 1 \\ \frac{|M|}{\sqrt{2}} & -\frac{|M|}{2\sqrt{2}} \end{vmatrix} = \frac{-\frac{3|M|}{2\sqrt{2}}}{1-\frac{|M|}{\sqrt{2}}(1+\mathrm{i})} \tag{D.61a}$$

$$= \frac{\frac{3|M|}{2\sqrt{2}}}{\frac{|M|}{\sqrt{2}}(1+\mathrm{i})-1} = \frac{3}{2}\frac{|M|\sqrt{2}}{|M|\sqrt{2}(1+\mathrm{i})-2} \tag{D.61b}$$

$$\approx \frac{3}{2}\frac{1}{1+\mathrm{i}} = \frac{3}{4}(1-\mathrm{i}) \qquad \text{for} \qquad |M| \gg 1. \tag{D.61c}$$

These are the coefficients given in Eq. (6.45).

D.5 Calculation of the product terms in the inner second-order streaming equation

In this section we provide a detailed calculation of the product terms on the left hand side of the inner, time-averaged second-order streaming equation, Eq. (6.48), which reduces it to Eq. (6.49). Our starting point is Eq. (6.48),

$$\left\langle \frac{\partial(\Psi_1, \partial_\eta^2 \Psi_1)}{\partial(\eta,\mu)} \right\rangle + \frac{2\mu}{1-\mu^2} \left\langle (\partial_\eta^2 \Psi_1)(\partial_\eta \Psi_1) \right\rangle = \frac{1}{2}\partial_\eta^4 \langle \Psi_2 \rangle , \tag{D.62}$$

and from Eq. (6.46a) we have the inner first-order solution,

$$\Psi_1(\eta,\mu) = \frac{3}{2}\left[\eta - \frac{1}{2}(1-\mathrm{i})\left(1-\mathrm{e}^{-(1+\mathrm{i})\eta}\right)\right](1-\mu^2), \tag{D.63}$$

which we remember has a time dependence given by $\mathrm{e}^{\mathrm{i}t}$ in the non-dimensionalised coordinates. Furthermore, the real part is understood. First, we calculate the three first

radial derivatives of Ψ_1,

$$\partial_\eta \Psi_1 = \frac{3}{2}\left[1 - \mathrm{e}^{-(1+\mathrm{i})\eta}\right]\left(1-\mu^2\right), \tag{D.64a}$$

$$\partial_\eta^2 \Psi_1 = \frac{3}{2}(1+\mathrm{i})\,\mathrm{e}^{-(1+\mathrm{i})\eta}\left(1-\mu^2\right), \tag{D.64b}$$

$$\partial_\eta^3 \Psi_1 = -3\,\mathrm{i}\,\mathrm{e}^{-(1+\mathrm{i})\eta}\left(1-\mu^2\right). \tag{D.64c}$$

Then, we calculate the remaining derivatives of Ψ_1,

$$\partial_\mu \Psi_1 = -3\left[\eta - \frac{1}{2}(1-\mathrm{i})\left(1-\mathrm{e}^{-(1+\mathrm{i})\eta}\right)\right]\mu, \tag{D.65a}$$

$$\partial_\mu \partial_\eta^2 \Psi_1 = -3(1+\mathrm{i})\,\mathrm{e}^{-(1+\mathrm{i})\eta}\,\mu. \tag{D.65b}$$

We are now ready to calculate the time averages of the product terms in Eq. (D.62). They can all be written on the form

$$\left\langle \mathrm{Re}\left[A(\eta,\mu)\,\mathrm{e}^{\,\mathrm{i}t}\right]\mathrm{Re}\left[B(\eta,\mu)\,\mathrm{e}^{\,\mathrm{i}t}\right]\right\rangle, \tag{D.66}$$

where the functions f and g are one of the derivatives in Eqs. (D.64) and (D.65). It can be shown [25, p. 186] that

$$\left\langle \mathrm{Re}\left[A(\eta,\mu)\,\mathrm{e}^{\,\mathrm{i}t}\right]\mathrm{Re}\left[B(\eta,\mu)\,\mathrm{e}^{\,\mathrm{i}t}\right]\right\rangle, = \frac{1}{2}\mathrm{Re}\left[A(\eta,\mu)\,B^*(\eta,\mu)\right]. \tag{D.67}$$

Using this result, the first term in Eq. (D.62) is

$$\left\langle \frac{\partial(\Psi_1, \partial_\eta^2 \Psi_1)}{\partial(\eta,\mu)} \right\rangle = \left\langle \mathrm{Re}\left[\partial_\eta \Psi_1\,\mathrm{e}^{\,\mathrm{i}t}\right]\mathrm{Re}\left[\partial_\mu \partial_\eta^2 \Psi_1\,\mathrm{e}^{\,\mathrm{i}t}\right]\right\rangle - \left\langle \mathrm{Re}\left[\partial_\mu \Psi_1\,\mathrm{e}^{\,\mathrm{i}t}\right]\mathrm{Re}\left[\partial_\eta^3 \Psi_1\,\mathrm{e}^{\,\mathrm{i}t}\right]\right\rangle$$

$$= \frac{1}{2}\mathrm{Re}\left[\left(\partial_\eta \Psi_1\right)\left(\partial_\mu \partial_\eta^2 \Psi_1\right)^*\right] - \frac{1}{2}\mathrm{Re}\left[\left(\partial_\mu \Psi_1\right)\left(\partial_\eta^3 \Psi_1\right)^*\right] \tag{D.68a}$$

$$= \frac{1}{2}\mathrm{Re}\left[\left(\frac{3}{2}\left[1-\mathrm{e}^{-(1+\mathrm{i})\eta}\right]\left(1-\mu^2\right)\right)\left(-3(1+\mathrm{i})\,\mathrm{e}^{-(1+\mathrm{i})\eta}\,\mu\right)^*\right] \tag{D.68b}$$

$$- \frac{1}{2}\mathrm{Re}\left[\left(-3\left[\eta - \frac{1}{2}(1-\mathrm{i})\left(1-\mathrm{e}^{-(1+\mathrm{i})\eta}\right)\right]\mu\right)\left(-3\,\mathrm{i}\,\mathrm{e}^{-(1+\mathrm{i})\eta}\left(1-\mu^2\right)\right)^*\right]. \tag{D.68c}$$

We collect common factors, perform the complex conjugation and take the real part,

$$\left\langle \frac{\partial\big(\Psi_1, \partial_\eta^2 \Psi_1\big)}{\partial(\eta,\mu)} \right\rangle = \left\langle \mathrm{Re}\left[\partial_\eta \Psi_1 \, \mathrm{e}^{\,\mathrm{i}t}\right] \mathrm{Re}\left[\partial_\mu \partial_\eta^2 \Psi_1 \, \mathrm{e}^{\,\mathrm{i}t}\right] \right\rangle - \left\langle \mathrm{Re}\left[\partial_\mu \Psi_1 \, \mathrm{e}^{\,\mathrm{i}t}\right] \mathrm{Re}\left[\partial_\eta^3 \Psi_1 \, \mathrm{e}^{\,\mathrm{i}t}\right] \right\rangle$$

$$= -\frac{9}{2}\,\mu\big(1-\mu^2\big) \left\{ \frac{1}{2}\,\mathrm{Re}\left[\left(1 - \mathrm{e}^{-(1+\mathrm{i})\eta}\right) \left((1+\mathrm{i})\,\mathrm{e}^{-(1+\mathrm{i})\eta}\right)^* \right] \right. \tag{D.69a}$$

$$\left. - \mathrm{Re}\left[\left(\eta - \frac{1}{2}(1-\mathrm{i}) \left(1 - \mathrm{e}^{-(1+\mathrm{i})\eta}\right) \right) \left(\mathrm{i}\,\mathrm{e}^{-(1+\mathrm{i})\eta}\right)^* \right] \right\} \tag{D.69b}$$

$$= -\frac{9}{2}\,\mu\big(1-\mu^2\big) \left\{ \frac{1}{2}\,\mathrm{Re}\left[\left(1 - \mathrm{e}^{-(1+\mathrm{i})\eta}\right) \left((1-\mathrm{i})\,\mathrm{e}^{-(1-\mathrm{i})\eta}\right) \right] \right. \tag{D.69c}$$

$$\left. - \mathrm{Re}\left[\left(\eta - \frac{1}{2}(1-\mathrm{i}) \left(1 - \mathrm{e}^{-(1+\mathrm{i})\eta}\right) \right) \left(-\mathrm{i}\,\mathrm{e}^{-(1-\mathrm{i})\eta}\right) \right] \right\} \tag{D.69d}$$

$$= -\frac{9}{2}\,\mu\big(1-\mu^2\big)\,\mathrm{Re}\left\{ \frac{1}{2} \left(1 - \mathrm{e}^{-(1+\mathrm{i})\eta}\right) \left((1-\mathrm{i})\,\mathrm{e}^{-(1-\mathrm{i})\eta}\right) \right. \tag{D.69e}$$

$$\left. - \left(\eta - \frac{1}{2}(1-\mathrm{i}) \left(1 - \mathrm{e}^{-(1+\mathrm{i})\eta}\right) \right) \left(-\mathrm{i}\,\mathrm{e}^{-(1-\mathrm{i})\eta}\right) \right\} \tag{D.69f}$$

$$= -\frac{9}{2}\,\mu\big(1-\mu^2\big)\,\mathrm{Re}\left\{ \frac{1}{2} \left(\mathrm{e}^{-(1-\mathrm{i})\eta} - \mathrm{i}\,\mathrm{e}^{-(1-\mathrm{i})\eta} - \mathrm{e}^{-2\eta} + \mathrm{i}\,\mathrm{e}^{-2\eta} \right) \right. \tag{D.69g}$$

$$\left. - \left(\mathrm{i}\eta\,\mathrm{e}^{-(1-\mathrm{i})\eta} - \frac{1}{2}\,\mathrm{i}(1-\mathrm{i})\,\mathrm{e}^{-(1-\mathrm{i})\eta} + \frac{1}{2}\,\mathrm{i}(1-\mathrm{i})\,\mathrm{e}^{-2\eta} \right) \right\} \tag{D.69h}$$

Using that $\mathrm{e}^{-(1-\mathrm{i})\eta} = \mathrm{e}^{-\eta}\,(\cos\eta + \mathrm{i}\sin\eta)$, we get

$$\left\langle \frac{\partial\big(\Psi_1, \partial_\eta^2 \Psi_1\big)}{\partial(\eta,\mu)} \right\rangle \tag{D.70a}$$

$$= -\frac{9}{2}\,\mu\big(1-\mu^2\big) \left\{ \frac{1}{2} \left(\mathrm{e}^{-\eta}\cos\eta + \mathrm{e}^{-\eta}\sin\eta - \mathrm{e}^{-2\eta} \right) \right. \tag{D.70b}$$

$$\left. - \left(-\eta\,\mathrm{e}^{-\eta}\sin\eta + \frac{1}{2}\,\mathrm{e}^{-\eta}\sin\eta - \frac{1}{2}\,\mathrm{e}^{-\eta}\cos\eta + \frac{1}{2}\,\mathrm{e}^{-2\eta} \right) \right\} \tag{D.70c}$$

$$= -\frac{9}{2}\,\mu\big(1-\mu^2\big) \left(\mathrm{e}^{-\eta}\cos\eta + \eta\,\mathrm{e}^{-\eta}\sin\eta - \mathrm{e}^{-2\eta} \right). \tag{D.70d}$$

We proceed to use the result in Eq. (D.67) on the second product term in Eq. (D.62),

$$\Big\langle(\partial_\eta^2\Psi_1)(\partial_\eta\Psi_1)\Big\rangle = \Big\langle \mathrm{Re}\left[\partial_\eta^2\Psi_1\,\mathrm{e}^{\,\mathrm{i}t}\right]\mathrm{Re}\left[\partial_\eta\Psi_1\,\mathrm{e}^{\,\mathrm{i}t}\right]\Big\rangle = \frac{1}{2}\mathrm{Re}\left[\left(\partial_\eta^2\Psi_1\right)\left(\partial_\eta\Psi_1\right)^*\right] \tag{D.71a}$$

$$= \frac{1}{2}\mathrm{Re}\left[\left(\frac{3}{2}(1+\mathrm{i})\,\mathrm{e}^{-(1+\mathrm{i})\eta}\left(1-\mu^2\right)\right)\left(\frac{3}{2}\left[1-\mathrm{e}^{-(1+\mathrm{i})\eta}\right]\left(1-\mu^2\right)\right)^*\right]$$

$$= \frac{9}{8}\big(1-\mu^2\big)^2\,\mathrm{Re}\left[\left((1+\mathrm{i})\,\mathrm{e}^{-(1+\mathrm{i})\eta}\right)\left(1-\mathrm{e}^{-(1+\mathrm{i})\eta}\right)^*\right] \tag{D.71b}$$

$$= \frac{9}{8}\big(1-\mu^2\big)^2\,\mathrm{Re}\left[\left((1+\mathrm{i})\,\mathrm{e}^{-(1+\mathrm{i})\eta}\right)\left(1-\mathrm{e}^{-(1-\mathrm{i})\eta}\right)\right] \tag{D.71c}$$

$$= \frac{9}{8}\big(1-\mu^2\big)^2\,\mathrm{Re}\left[\mathrm{e}^{-(1+\mathrm{i})\eta}+\mathrm{i}\,\mathrm{e}^{-(1+\mathrm{i})\eta}-\mathrm{e}^{-2\eta}-\mathrm{i}\,\mathrm{e}^{-2\eta}\right] \tag{D.71d}$$

$$= \frac{9}{8}\big(1-\mu^2\big)^2\left(\mathrm{e}^{-\eta}\cos\eta+\mathrm{e}^{-\eta}\sin\eta-\mathrm{e}^{-2\eta}\right). \tag{D.71e}$$

Insertion of the results in Eqs. (D.70) and (D.71) into Eq. (D.62) yields

$$\partial_\eta^4\,\langle\Psi_2\rangle = -2\,\frac{9}{2}\,\mu\big(1-\mu^2\big)\left(\mathrm{e}^{-\eta}\cos\eta+\eta\,\mathrm{e}^{-\eta}\sin\eta-\mathrm{e}^{-2\eta}\right) \tag{D.72a}$$

$$+\,2\,\frac{2\mu}{1-\mu^2}\,\frac{9}{8}\big(1-\mu^2\big)\left(\mathrm{e}^{-\eta}\cos\eta+\mathrm{e}^{-\eta}\sin\eta-\mathrm{e}^{-2\eta}\right) \tag{D.72b}$$

$$= \frac{9}{2}\,\mu\big(1-\mu^2\big)\Big(-2\,\mathrm{e}^{-\eta}\cos\eta-2\eta\,\mathrm{e}^{-\eta}\sin\eta+2\,\mathrm{e}^{-2\eta}+\mathrm{e}^{-\eta}\cos\eta+\mathrm{e}^{-\eta}\sin\eta-\mathrm{e}^{-2\eta}\Big)$$

$$= \frac{9}{2}\left(\mathrm{e}^{-2\eta}-\mathrm{e}^{-\eta}\cos\eta+\mathrm{e}^{-\eta}\sin\eta-2\eta\,\mathrm{e}^{-\eta}\sin\eta\right)\mu\big(1-\mu^2\big). \tag{D.72c}$$

The equality between the first and the last term in Eq. (D.72) is the expression given in Eq. (6.49).

D.6 Outer second-order solution

In this section we provide the details used in solving the outer time-averaged, second-order streaming equation given in Eq. (6.53),

$$D^4\langle\psi_2\rangle = D^2\big(D^2\langle\psi_2\rangle\big) = 0. \tag{D.73}$$

The outer second-order solution is given in Eq. (6.51),

$$\langle\Psi_2(\eta,\mu)\rangle = \frac{9}{2}\left[\frac{1}{16}\,\mathrm{e}^{-2\eta}+\frac{5}{4}\,\mathrm{e}^{-\eta}\cos\eta+\frac{3}{4}\,\mathrm{e}^{-\eta}\sin\eta+\frac{1}{2}\eta\,\mathrm{e}^{-\eta}\sin\eta+C_{\mathrm{I}}\eta^3+C_{\mathrm{II}}\eta^2+\frac{5}{8}\eta-\frac{21}{16}\right]\mu(1-\mu^2). \tag{D.74}$$

We know that the inner and outer solutions must match for $r\to 1$ and $\eta\to\infty$, from which we infer that the solutions must all have the angular factor $\mu\big(1-\mu^2\big)$. We thus expect four solutions which we write as follows,

$$\langle\psi_2(r,\mu)\rangle = \langle\psi_{21}(r,\mu)\rangle + \langle\psi_{22}(r,\mu)\rangle, \qquad D^2\langle\psi_{21}\rangle = 0, \qquad D^2\langle\psi_{22}\rangle = \langle\psi_{21}\rangle. \tag{D.75}$$

Assuming that $\psi_{21}(r,\mu) = R_{21}(r)\mu\big(1-\mu^2\big)$, we get

$$D^2\big\langle\psi_{21}\big\rangle = \partial_r^2\big\langle\psi_{21}\big\rangle + \frac{1-\mu^2}{r^2}\,\partial_\mu^2\big\langle\psi_{21}\big\rangle = \left(\partial_r^2\big\langle R_{21}\big\rangle - \frac{6}{r^2}\,\big\langle R_{21}\big\rangle\right)\mu\big(1-\mu^2\big) = 0, \quad \text{(D.76)}$$

which has the solution

$$\big\langle R_{21}(r)\big\rangle = c_{\mathrm{I}} r^3 + c_{\mathrm{II}} r^{-2}. \quad \text{(D.77)}$$

We use Eq. (D.76) to proceed to the second equation in Eq. (D.75), assuming that $\psi_{22}(r,\mu) = R_{22}(r)\mu\big(1-\mu^2\big)$,

$$D^2\big\langle\psi_{22}\big\rangle = \left(\partial_r^2\big\langle R_{22}\big\rangle - \frac{6}{r^2}\,\big\langle R_{22}\big\rangle\right)\mu\big(1-\mu^2\big) = \Big(c_{\mathrm{I}} r^3 + c_{\mathrm{II}} r^{-2}\Big)\,\mu\big(1-\mu^2\big). \quad \text{(D.78)}$$

By direct insertion, it can be shown that this equation has the solution

$$\big\langle R_{22}(r)\big\rangle = -c_{\mathrm{I}}\,\frac{7}{42} + c_{\mathrm{II}}\,\frac{3}{42}\,r^5 + c_{\mathrm{II}} r^3 + c_{\mathrm{IV}} r^{-2}. \quad \text{(D.79)}$$

We combine the solutions in Eqs. (D.77) and (D.79) and redefine the constants to obtain the outer second-order solution

$$\big\langle\psi_2(r,\mu)\big\rangle = \big[c_{\mathrm{I}} r^5 + c_{\mathrm{II}} r^3 + c_{\mathrm{III}} + c_{\mathrm{IV}} r^{-2}\big]\mu\big(1-\mu^2\big). \quad \text{(D.80)}$$

This is the solution given in Eq. (6.54).

Appendix E

Appendix to Chapter 7

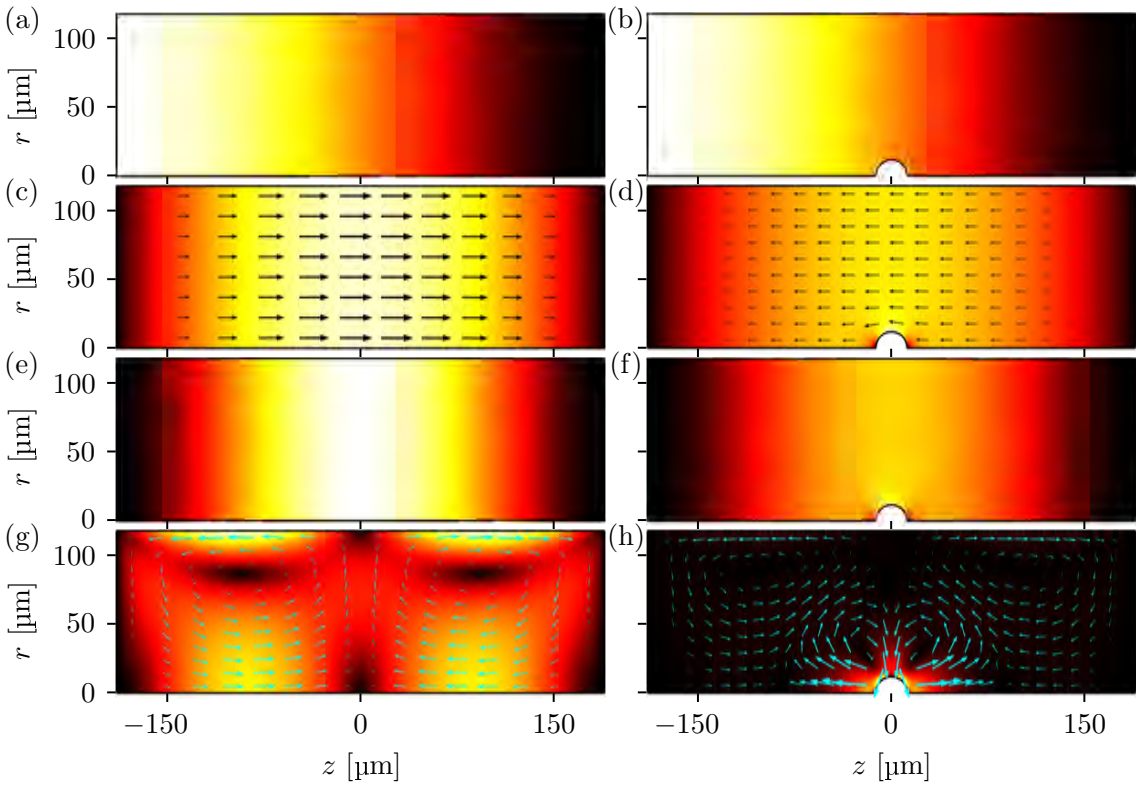

Figure E.1 First-order and time-averaged second-order pressure and velocity fields. The subfigures in the left column show the fields of the reference system, whereas those in the right column show the fields of the seed particle system. All the colour plots have a linear scale from black (lowest field magnitude) to white (highest field magnitude) and all the vector plots except (h) have a linear scale from no arrow (zero magnitude) to the largest arrow (maximum magnitude). The first-order pressure is shown in (a) and (b). The maximum and minimum pressure is (a) $\pm p_\mathrm{a} = \pm 0.25$ Pa and (b) $\pm p_\mathrm{a} \pm 0.27$ Pa, and orange corresponds to zero pressure. The colour plot thus shows a half-wavelength standing pres-

sure wave with a node at $z = 0$ as expected. The first-order velocity field is shown in (c) and (d). The maximum magnitude is (c) $v_\mathrm{a} = 0.18$ m/s and (d) $v_\mathrm{a} = 0.28$ m/s, while the minimum is zero for both. The colour and vector plots thus show a half-wavelength standing wave with an antinode at $z = 0$. The time-averaged second-order pressure is shown in (e) and (f). The maximum and minimum are (e) $\pm\left\langle p_2\right\rangle_\mathrm{max} = \pm 7.5$ Pa and (f) $\pm\left\langle p_2\right\rangle_\mathrm{max} = \pm 8.5$. The colour plots thus show a full-wavelength standing pressure wave. The time-averaged seconder order velocity field (the streaming) is shown in (g) and (h). The maximum streaming is (g) $\left\langle v_2\right\rangle_\mathrm{max} = 7.4$ µm /s and (h) $\left\langle v_2\right\rangle_\mathrm{max} = 169$. The minimum streaming is zero and in (h) the vector scale is logarithmic.

Bibliography

[1] B. Hammarström, T. Laurell, and J. Nilsson, *Seed particle enabled acoustic trapping of bacteria and nanoparticles in continuous flow systems.* Lab Chip **12**, 4296–4304 (2012).

[2] P. Augustsson, C. Magnusson, M. Nordin, H. Lilja, and T. Laurell, *Microfluidic, label-free enrichment of prostate cancer cells in blood based on acoustophoresis.* Anal. Chem. **84**(18), 7954–7962 (2012).

[3] J. V. Norris, M. Evander, K. M. Horsman-Hall, J. Nilsson, T. Laurell, and J. P. Landers, *Acoustic differential extraction for forensic analysis of sexual assault evidence.* Anal. Chem. **81**(15), 6089–6095 (2009).

[4] C. Grenvall, P. Augustsson, J. R. Folkenberg, and T. Laurell, *Harmonic microchip acoustophoresis: A route to online raw milk sample precondition in protein and lipid content quality control.* Anal. Chem. **81**(15), 6195–6200 (2009).

[5] M. A. M. Gijs, *Magnetic bead handling on-chip: new opportunities for analytical applications.* Microfluidics Nanofluidics **1**(1), 22–40 (2004).

[6] T. S. Simonova, V. N. Shilov, and O. A. Shramko, *Low-frequency dielectrophoresis and the polarization interaction of uncharged spherical particles with an induced debye atmosphere of arbitrary thickness.* Colloid Journal **63**(1), 108–155 (2001).

[7] A. Lenshof, C. Magnusson, and T. Laurell, *Acoustofluidics 8: Applications in acoustophoresis in continuous flow microsystems.* Lab Chip **12**, 1210–1223 (2012).

[8] A. Lenshof and T. Laurell, *Emerging clinical applications of microchip-based acoustophoresis.* JALA **16**, 443–449 (2011).

[9] P. B. Muller and H. Bruus, *Numerical study of thermoviscous effects in ultrasound-induced acoustic streaming in microchannels.* Phys. Rev. E **90**(4), 043016 (2014).

[10] F. Petersson, A. Nilsson, C. Holm, H. Jönsson, and T. Laurell, *Separation of lipids from blood utilizing ultrasonic standing waves in microfluidic channels.* Analyst **129**(10), 938–43 (2004).

[11] R. Barnkob, P. Augustsson, T. Laurell, and H. Bruus, *An automated full-chip micro-PIV setup for measuring microchannel acoustophoresis: Simultaneous determination*

of forces from acoustic radiation and acoustic streaming. In S. Verporte, H. Andersson, J. Emneus, and N. Pamme (eds.), *Proc. 14th MicroTAS, 3 - 7 October 2010, Groningen, The Netherlands*, 1247–49 (CBMS) (2010).

[12] Private e-mail correspondence with Professor Henrik Bruus (DTU Physics, Department of Physics, bruus@dtu.fysik.dk).

[13] C. P. Nielsen, *Introduction to weak form modeling in comsol* (2013), a guide developed in the Theoretical Microfluidics Group headed by Professor Henrik Bruus (bruus@fysik.dtu.dk) at the Department of Physics at the Technical University of Denmark.

[14] H. Bruus, *Implementation of first- and second-order acoustic perturbation theory in comsol* (2016), DTU Physics, Department of Physics (bruus@fysik.dtu.dk).

[15] L. V. King, *On the acoustic radiation pressure on spheres*. Proc. R. Soc. London, Ser. A **147**(861), 212–240 (1934).

[16] K. Yosioka and Y. Kawasima, *Acoustic radiation pressure on a compressible sphere*. Acustica **5**, 167–173 (1955).

[17] L. P. Gorkov, *On the forces acting on a small particle in an acoustical field in an ideal fluid*. Sov. Phys.–Dokl. **6**(9), 773–775 (1962), [Doklady Akademii Nauk SSSR **140**, 88 (1961)].

[18] M. Settnes and H. Bruus, *Forces acting on a small particle in an acoustical field in a viscous fluid*. Phys. Rev. E **85**, 016327 (2012).

[19] J. T. Karlsen and H. Bruus, *Forces acting on a small particle in an acoustical field in a thermoviscous fluid*. Phys. Rev. E **92**, 043010 (2015).

[20] H. Bruus, *Acoustofluidics 7: The acoustic radiation force on small particles*. Lab Chip **12**, 1014–1021 (2012).

[21] S. Sadhal, *Acoustofluidics 13: Analysis of acoustic streaming by singular perturbation*. Lab Chip **in press**, (Tutorial Part 13) (2012).

[22] M. Wiklund, R. Green, and M. Ohlin, *Acoustofluidics 14: Applications of acoustic streaming in microfluidic devices*. Lab Chip **12**, 2438–2451 (2012).

[23] P. M. Tribler, *Acoustic streaming in microchannels - The trinity of analytics, numerics and experiments*. Ph.D. thesis, DTU Physics, Department of Physics, www.fysik.dtu.dk/microfluidics.

[24] P. B. Muller, M. Rossi, A. G. Marin, R. Barnkob, P. Augustsson, T. Laurell, C. J. Kähler, and H. Bruus, *Ultrasound-induced acoustophoretic motion of microparticles in three dimensions*. Phys. Rev. E **88**(2), 023006 (2013).

[25] H. Bruus, *Theoretical Microfluidics* (Oxford University Press, Oxford) (2008).

[26] N. Riley, *On a sphere oscillating in a viscous fluid*. Quarterly Journal of Mechanics & Applied Mathematics **19**(4), 461–472 (1966).

[27] S. Sadhal, *Acoustofluidics 15: Streaming with sound waves interacting with solid particles*. Lab Chip **12**, 2600–2611 (2012).

[28] L. Prandtl, *Über Flüssigkeitsbewegung bei sehr kleiner Reibung*. Verhandl. III. Intern. Math. Kongr. Heidelberg 484 (1904).

[29] M. D. Van Dyke, *Perturbation Methods in Fluid Mechanics* (Parabolic Press, Stanford CA), 2nd edn. (1975).

[30] J. Dual and T. Schwarz, *Acoustofluidics 3: Continuum mechanics for ultrasonic particle manipulation*. Lab Chip **12**, 244–252 (2012).

[31] P. B. Muller, R. Barnkob, M. J. H. Jensen, and H. Bruus, *A numerical study of microparticle acoustophoresis driven by acoustic radiation forces and streaming-induced drag forces*. Lab Chip **12**, 4617–4627 (2012).

[32] W. Wagner and A. Pruss, *The iapws formulation 1995 for the thermodynamic properties of ordinary water substance for general and scientific use*. J. Phys. Chem. Ref. Data **31**(2), 387–535 (2002).

[33] M. L. Huber, R. A. Perkins, A. Laesecke, D. G. Friend, J. V. Sengers, M. J. Assael, I. N. Metaxa, E. Vogel, R. Mares, and K. Miyagawa, *New international formulation for the viscosity of h2o*. J. Phys. Chem. Ref. Data **38**(2), 101–125 (2009).

[34] M. L. Huber, R. A. Perkins, D. G. Friend, J. V. Sengers, M. J. Assael, I. N. Metaxa, K. Miyagawa, R. Hellmann, and E. Vogel, *New international formulation for the thermal conductivity of h2o*. J. Phys. Chem. Ref. Data **41**(3), 033102 (2012).

[35] *CRC Handbook of Chemistry and Physics* (CRC Press, Boca Raton, FL), 95th edn. (2014).

[36] *CRC Polymers: A Properties Database* (CRC Press, Boca Raton, FL) (2014).

[37] Onda Corporation, *Tables of Acoustic Properties of Materials: Plastics* (www.ondacorp.com/tecref_acoustictable.shtml) (2015).

[38] E. S. Domalski and E. D. Hearing, *Heat Capacities and Entropies of Organic Compounds in the Condensed Phase. Volume III*. J. Phys. Chem. Ref. Data **25**(1), 1 (1996).

[39] S. S. Chang and A. B. Bestul, *Heat capacities for atactic polystyrene of narrow molecular weight distribution to 360°K.* J. Polym. Sci. A-2 Polym. Phys. **6**(5), 849–860 (1968).

[40] H. Bruus, *Lecture notes: Acoustic streaming* (2015), DTU Physics, Department of Physics (bruus@dtu.fysik.dk).